Revised version submitted to *Geochimica et Cosmochimica Acta*

A temporal shift of chondrule generation from the inner to outer Solar System inferred from oxygen isotopes and Al-Mg chronology of chondrules from primitive CM and CO chondrites

Kohei Fukuda [a,*], Travis J. Tenner [a,b], Makoto Kimura [c], Naotaka Tomioka [d], Guillaume Siron [a], Takayuki Ushikubo [d], Noël Chaumard [a,e], Andreas T. Hertwig [a,f], Noriko T. Kita [a]

[a] WiscSIMS, Department of Geoscience, University of Wisconsin-Madison, 1215 W. Dayton St., Madison, WI 53706, USA

[b] Chemistry Division, Nuclear and Radiochemistry, Los Alamos National Laboratory, MSJ514, Los Alamos, NM 87545, USA

[c] National Institute of Polar Research, Tokyo 190-8518, Japan

[d] Kochi Institute for Core Sample Research, JAMSTEC, Kochi 783-8502, Japan

[e] Fi Group, Direction scientifique, 14 terrasse Bellini, 92800 Puteaux, France

[f] Institute of Earth Sciences, Heidelberg University, Im Neuenheimer Feld 236, 69120 Heidelberg, Germany

[*]To whom correspondence should be addressed. E-mail: kfukuda2@wisc.edu

ABSTRACT

Deciphering the spatial and temporal evolution of chondrules allows for a better understanding of how asteroidal seeds formed, migrated, and eventually accreted into parent asteroids. Here we report high precision Al-Mg ages and oxygen three-isotope ratios of fifteen FeO-poor chondrules from the least metamorphosed Mighei-like (CM) and Ornans-like (CO) carbonaceous chondrites, Asuka 12236 (CM2.9), Dominion Range 08006 (CO3.01), and Yamato-81020 (CO3.05). This is the first report of Al-Mg ages of chondrules from the CM chondrite group. All but one of the fifteen chondrules exhibit a restricted range of inferred initial $^{26}Al/^{27}Al$ ratios, and all ratios are $\leq 6.0 \times 10^{-6}$, which is systematically lower than those of the majority of ordinary chondrite (OC) chondrules. These observations indicate that the majority of chondrules in the outer Solar System were produced ≥ 2.2 Ma after the formation of Ca-Al-rich inclusions (CAIs), which postdates OC chondrule formation in the inner Solar System (≤ 2.2 Ma after CAI formation). We propose that the discrete chondrule-forming events in different disk regions reflect a time difference in growth and orbital evolution of planetesimals within the first 4 Ma of the Solar System.

One chondrule from Asuka 12236 has an age of 1.9 Ma after CAI formation and is therefore significantly older than the other fourteen chondrules, meaning this chondrule formed contemporaneously with the majority of OC chondrules. This old chondrule also exhibits ^{16}O-depleted oxygen isotope characteristics compared to the other chondrules, suggesting a distinct formation region, probably inside the disk region relative to where the majority of CM and CO chondrules formed. Our results indicate that this old chondrule has migrated from the inner to the outer part of the protoplanetary disk within ~1 Ma and then accreted into the CM parent asteroid >3 Ma after CAI formation, although its formation exterior to the accretion region of the CM parent asteroid and subsequent inward migration cannot be ruled out completely.

1. INTRODUCTION

Astronomical observations of young stellar objects show that submicrometer to centimeter-sized dust grains are heterogeneously distributed in a given protoplanetary disk (van der Marel et al., 2013). Clarifying the spatio-temporal distribution of dust grains is crucial to decipher when and where planetesimals form in a protoplanetary disk (Harsono et al., 2018). Regarding our Solar System, chondrites are among the most primitive, undifferentiated meteorites that contain abundant submillimeter-sized objects known as chondrules, which are melted objects produced by transient heating events in the protoplanetary disk (Scott and Krot, 2014). The nature of transient heating events and timing of chondrule formation in our Solar System is a long-standing question (e.g., Connolly and Jones, 2016). Previous studies have proposed that chondrule formation events require the formation of a proto-Jupiter, planetary embryos, and/or large planetesimals; this suggests that chondrules might have formed as a consequence of planetary growth (e.g., Ciesla et al., 2004; Boss and Durisen, 2005; Asphaug et al., 2011; Desch et al., 2012 and references therein; Morris et al., 2012; Sanders and Scott, 2012; Johnson et al., 2015; Lichtenberg et al., 2018; Nagasawa et al., 2019; Gong et al., 2019). Thus, determining the time and location of chondrule formation events can provide key constraints on the spatio-temporal evolution of planetary bodies in our Solar System.

Chondrules from different chondrite groups have distinct chemical, isotopic, and physical properties, suggesting that they formed in local disk regions and subsequently accreted to their respective parent asteroid (e.g., Alexander, 2005; Alexander et al., 2008; Jones, 2012; Alexander and Ebel, 2012; Palme et al., 2015). Oxygen isotope ratios of individual chondrules from carbonaceous chondrites (CCs) show a large range of mass-independent fractionation (e.g., Tenner et al., 2018a and references therein). In contrast, chondrules from non-carbonaceous chondrites (NCs) such as ordinary and enstatite chondrites show a narrow range of oxygen isotope ratios, which is close to those of Earth and Mars (e.g., Kita et al., 2010; Weisberg et al., 2011, 2021). The large mass-independent fractionation in CC chondrules is likely related to the abundance of ^{16}O-poor water ice in CC chondrule-forming regions, while the narrow range observed in NC chondrules indicate the complete evaporation of water ice and homogenization of oxygen isotopes in the NC chondrule-forming regions (e.g., Yurimoto and Kuramoto, 2004; Connolly and Huss, 2010; Tenner et al., 2015, 2018a). NC and CC chondrules also exhibit distinct nucleosynthetic Cr and Ti isotope anomalies (Gerber et al., 2017; Schneider et al., 2020). These observations are broadly consistent with a fundamental isotopic dichotomy between carbonaceous and non-carbonaceous meteorite groups, including achondrites and irons, which is thought to arise from differences in their formation locations, most likely the inner and outer Solar System, respectively (Warren, 2011). The W and Mo isotopic compositions of iron meteorites indicate that the carbonaceous and non-carbonaceous reservoirs co-existed and maintained their isotopic differences during the earliest stage of the Solar System evolution (Kruijer et al., 2017). Currently, the most popular explanation for these two reservoirs is that they were separated by proto-Jupiter or a pressure maximum in the disk (Budde et al., 2016a; Kruijer et al., 2017, 2020; Brasser and Mojzsis, 2020; Kleine et al., 2020 and references therein). NCs have isotopic compositions that are similar to those of Earth and Mars, indicating that they formed inside the orbit of proto-Jupiter (we refer this region as "inner Solar System"). The CCs formed at the other side, i.e., outside the orbit of proto-Jupiter (we refer this region as "outer Solar System"), which is consistent with differences in their volatile contents and abundances of refractory inclusions (e.g., Desch et al., 2018). If correct, the distinct O, Cr, and Ti isotopic properties in chondrules also indicate that chondrule formation occurred in different disk regions, including the inner and outer Solar System (Schneider et al., 2020). In this paper we first consider the hypothesis of the "Jupiter-divide" and discuss the time and location of chondrule formation based on oxygen isotopes and Al-Mg chronology. Then we further discuss whether the current understanding of chondrule formation agrees/disagrees with this hypothesis.

Chondrule ages with uncertainties smaller than 0.5 million years (Ma) have been obtained by absolute Pb-Pb dating and relative age dating using the decay of the short-lived nuclide ^{26}Al to ^{26}Mg (half-life of 0.705 Ma; Nishiizumi, 2004). The latter chronometer determines the age relative to the formation of calcium-aluminum-rich inclusions (CAIs), the oldest solids in the Solar System (Amelin et al., 2010; Bouvier and Wadhwa, 2010; Connelly et al., 2012). The Pb-Pb dating of NC chondrules indicates protracted chondrule formation in the inner Solar System spanning from 0 to 4 Ma after CAIs (Connelly et al., 2012; Bollard et al., 2017), while the majority of the Al-Mg ages of NC chondrules indicate a shorter duration, ranging from 1.5–3.0 Ma after CAIs (e.g., Kita et al., 2000; Villeneuve et al., 2009; Pape et al., 2019; Siron et al., 2021a; see also Nagashima et al., 2018 and references therein). The Pb-Pb dating of CC chondrules also indicates protracted chondrule formation in the outer Solar System (0 to 4 Ma after CAIs; Connelly et al., 2012; Bollard et al., 2017), while the Al-Mg ages of CC chondrules indicate a shorter duration, ranging from 1.5–4.0 Ma after CAIs (Nagashima et al., 2018 and references therein). Despite this inconsistency between Pb-Pb and Al-Mg ages, NC and CC chondrules generally do not show distinguishable ages, suggesting that chondrule formation occurred contemporaneously in the inner and outer Solar System (Kurahashi et al., 2008; Bollard et al., 2017).

In contrast to observed chondrule formation ages, parent asteroids of chondritic meteorites from the inner and outer disk might not accrete contemporaneously; i.e., the majority of CC parent bodies accreted ~2.5–4.0 Ma after CAIs, which postdates accretion of NC parent bodies (~2 Ma after CAIs) (e.g., Fujiya et al., 2012, 2013; Sugiura and Fujiya, 2014; Doyle et al., 2015; Jogo et al., 2017; Blackburn et al., 2017; Edwards and Blackburn, 2020). Thus, the later accretion of asteroids in the outer Solar System indicates a time interval of up to ~4 Ma between the earliest chondrule formation dated by Pb-Pb dating and their subsequent accretion into the CC parent asteroids. However, mixing time scales of chondrules in the protoplanetary disk could have been much shorter than 1 Ma (Alexander, 2005; Cuzzi et al., 2010), otherwise the distinct chondrule properties among each chondrite group would not be retained (e.g., Alexander et al., 2008; Hezel and Palme, 2010; Alexander and Ebel, 2012; Palme et al., 2015; Hezel et al., 2018 and references therein). Furthermore, the estimated accretion time of NC parent bodies (i.e., ~2 Ma after CAIs) is older than the youngest Al-Mg and Pb-Pb ages of NC chondrules (~3–4 Ma after CAIs; Vileuenve et al., 2009; Bollard et al., 2017; Pape et al., 2019). The discrepancy would be likely caused by disturbance of Al-Mg and U-Pb systematics of some NC chondrules during parent body alteration (Alexander and Ebel, 2012; Lewis and Jones, 2019; Siron et al., 2021a), or younger chondrules represent remelting of primary chondrules in the protoplanetary disk (Pape et al., 2021). As such, the relationship between the timing and duration of chondrule formation and their accretion into parent asteroids remains unclear. Recent high precision Al-Mg analyses of chondrules from the least metamorphosed chondrites point to restricted formation ages of NC chondrules (~1.8–2.2 Ma after CAIs; Siron et al., 2021a, 2021b) and a possible late formation of CC chondrules compared to those from NCs (Ushikubo et al., 2013; Nagashima et al., 2014, 2017; Schrader et al., 2017; Hertwig et al., 2019a; Tenner et al., 2019). If correct, then the timing of chondrule formation relative to the accretion of their respective parent asteroids would be consistent (e.g., Alexander et al., 2008; Budde et al., 2016b).

To further explore a possible difference in formation times between chondrules from the inner and outer Solar System, we obtained high precision Al-Mg ages and oxygen three-isotope ratios of anorthite-bearing chondrules from the least metamorphosed Mighei-like

(CM) and Ornans-like (CO) chondrites that are major groups among CCs (Scott and Krot, 2014). Anorthite has a relatively high closure temperature for the Al-Mg chronometer (≥500˚C; LaTourrette and Wasserburg, 1998; Van Orman et al., 2014) and is likely to remain undisturbed in the least metamorphosed chondrites (Ushikubo et al., 2013; Tenner et al., 2019; Siron et al., 2021a). We also investigated the mineral chemistry of anorthite in detail (e.g., abundance of excess silica [ ]Si_4O_8 endmember component; Beaty and Albee, 1980; Tenner et al., 2019) and conducted characterization by transmission electron microscopy (TEM), in order to evaluate the reliability of anorthite with respect to closure of the Al-Mg system in the chondrules studied here.

2. MATERIALS AND METHODS

2.1. Samples

For this study, we selected three carbonaceous chondrites, Asuka (A) 12236 (CM2.9; Kimura et al., 2020), Dominion Range (DOM) 08006 (classified as CO3.00 from Davidson et al., 2019a, while we adopt CO3.01 from FeNi-metal analyses of Tenner et al., 2018b), and Yamato (Y)-81020 (CO3.05; Kimura et al., 2008). A 12236 is one of the least altered CM chondrites recently identified by Kimura et al. (2020). This meteorite has a higher presolar grain abundance and amino acid concentration compared to other CM chondrites, consistent with A 12236 being a highly primitive and unheated CM chondrite (Nittler et al., 2021; Glavin et al., 2020). We investigated chondrules from two thin sections, A 12236 (thin section 51-1) and DOM 08006 (thin section 50), loaned to us by the National Institute of Polar Research (NIPR) and US Antarctic meteorite program (ANSMET), respectively. A 12236 (51-1) is one of the sections examined previously by Kimura et al. (2020). For the two thin sections, we selected 11 chondrules (5 from A 12236 and 6 from DOM 08006) that contain plagioclase grains larger than 10 µm, in order to obtain high precision Al-Mg isotope data. Oxygen isotope ratios of constituent minerals (olivine, pyroxene, plagioclase) in the 11 chondrules were also determined. We also selected four chondrules (Y20, Y24, Y71, Y175) from the Y-81020 thin section (56-1; NIPR) for reinvestigation of their Al-Mg ages, which have been previously analyzed by Kurahashi et al. (2008). Their petrology, mineral chemistry, and oxygen isotope ratios of olivine and pyroxene are reported in Kurahashi et al. (2008) and Tenner et al. (2013). The four chondrules from Y-81020 are all FeO-poor chondrules with Mg# > 98.7, where Mg# is defined as [Mg]/[Mg + Fe] in molar %. They are classified as porphyritic olivine pyroxene (Y20 and Y24), porphyritic pyroxene (Y71), and Al-rich (Y175). To complement the oxygen isotope analyses of olivine and pyroxene already analyzed, we measured the oxygen three-isotope ratios of plagioclase in these four chondrules.

2.2. Electron microscopy and electron microprobe analysis

Backscattered electron (BSE) and secondary electron (SE) images of individual chondrules were acquired using a Hitachi S-3400 scanning electron microscope (SEM) at the University of Wisconsin-Madison (UW-Madison). The major- and minor-element oxide compositions of chondrule minerals were obtained with a Cameca SX-51 or Cameca SXFive FE electron-probe microanalyzer (EPMA) at UW-Madison. The analytical conditions of each session and the detection limits are described in Supplementary Material 1. Probe for EPMA™ (PFE) was used for the data reduction and the estimation of the detection limits.

For mafic minerals, endmembers (molar %) are expressed as Fo (= [Mg]/[Mg + Fe]) for olivine, and En (= [Mg]/[Mg + Fe + Ca]), Fs (= [Fe]/[Mg + Fe + Ca]), and Wo (= [Ca]/[Mg + Fe + Ca]) for pyroxene. In this paper, low-Ca and high-Ca pyroxenes represent pyroxene with Wo < 10 and Wo ≥ 10, respectively. The Mg#s of olivine and pyroxene are expressed as Mg# = [Mg]/[Mg + Fe] in molar %. For plagioclase, the An content is expressed as An = [Ca]/[Ca + Na + K] in molar %. We also estimate an "excess silica" component that is the [ ]Si_4O_8 endmember component (Beaty and Albee, 1980). The calculation procedure of the excess silica component follows the description in Siron et al. (2021a).

2.3. Transmission electron microscopy (TEM)

For TEM observations, plagioclase grains in chondrule D89 from DOM 08006 were processed into an ultrathin foil ~150 nm thick using a Ga-ion beam after the deposition of a carbon protection layer in a focused ion beam (FIB) apparatus (Hitachi SMI-4050) at the Kochi Institute for Core Sample Research (KOCHI), JAMSTEC. The ultrathin foil was mounted on a Cu grid using a micromanipulator equipped with the FIB and investigated using a TEM (JEOL JEM-ARM200F at KOCHI) operated at an accelerating voltage of 200 kV. The sample was characterized with bright-field transmission electron imaging (BF-TEM) and by high-angle annular dark field scanning transmission electron imaging (HAADF-STEM). Crystal structures were identified using selected-area electron diffraction (SAED), and the chemical compositions of the samples were obtained using energy-dispersive X-ray spectrometry (EDS) with a 100-mm^2 silicon drift detector.

2.4. Secondary ion mass spectrometry (SIMS)

Oxygen three-isotope and Al-Mg isotope analyses were performed with the WiscSIMS Cameca IMS 1280 secondary ion mass spectrometer (SIMS) equipped with a radio-frequency (RF) plasma ion source. Five separate SIMS sessions (three for oxygen isotopes and two for Al-Mg isotopes) were conducted, for which analytical conditions were optimized for each session as described below. After each analytical session, the SIMS pits were examined with the Hitachi S-3400 SEM, the images of which are shown in Supplementary Materials 2 and 3.

2.4.1. SIMS oxygen isotope analyses

Olivine and pyroxene in chondrules from A 12236 and DOM 08006 were analyzed in separate sessions (S1 for A 12236, S2 for DOM 08006). The analytical conditions for both sessions are similar to those described in Kita et al. (2010) and Siron et al. (2021a). For both sessions, a $^{133}Cs^{+}$ primary ion beam was focused to a ~12 µm diameter spot at 2 nA. Secondary oxygen ions ($^{16}O^{-}$, $^{17}O^{-}$, and $^{18}O^{-}$) were detected simultaneously using multi-collector Faraday cups (MCFC). The FCs for $^{16}O^{-}$ and $^{18}O^{-}$ employed 10^{10} ohm and 10^{11} ohm resistors, respectively. To improve the precision of $\delta^{17}O$, the FC for $^{17}O^{-}$ employed a high gain feedback resistor (10^{12} ohm) with reduced thermal noise (Fukuda et al., 2021a; Bouden et al., 2021). Additionally, the count rate of $^{16}O^{1}H^{-}$ was measured at the end of each measurement in order to estimate the tailing effect on the $^{17}O^{-}$ signal (Heck et al., 2010). The contribution of the $^{16}O^{1}H^{-}$ was negligible (< 0.2‰) for most analyses (~99%), otherwise data were rejected. The baselines of the three FCs were monitored during each presputtering and averaged over eight analyses, which were taken as the values to correct secondary ion intensities. As in previous studies, 14–16 unknown analyses were bracketed by 8 analyses (4 before and 4 after the unknowns) of a San Carlos olivine reference material (hereafter SC-Ol; $\delta^{18}O$ = 5.32‰, Kita et al., 2010). The typical secondary $^{16}O^{-}$ ion intensity when measuring SC-Ol was 2.3×10^{9} counts per second (cps). The measured $^{18}O/^{16}O$ and $^{17}O/^{16}O$ ratios were normalized to the VSMOW scale (Vienna Standard Mean Ocean Water; Baertschi, 1976), expressed in delta notation as (‰): $\delta^{17,18}O = [(^{17,18}O/^{16}O)_{sample}/(^{17,18}O/^{16}O)_{VSMOW} - 1] \times 1000$. The mass-independent fractionation $\Delta^{17}O$ was calculated as $\Delta^{17}O = \delta^{17}O - 0.52 \times \delta^{18}O$.

In addition to SC-Ol, several olivine and pyroxene reference materials listed in Supplementary Table S4-2, whose chemical compositions are similar to the measured chondrule olivine and pyroxene grains, were analyzed to estimate the instrumental biases on $\delta^{18}O$. For the A 12236 session (S1), the averaged external reproducibility of the bracketing standard SC-Ol was typically 0.17‰, 0.24‰, and 0.25‰ (2SD) for $\delta^{18}O$, $\delta^{17}O$, and $\Delta^{17}O$, respectively; for the DOM 08006 session (S2) the values were 0.19‰, 0.22‰, and 0.23‰ (2SD), respectively. The external reproducibilities (2SD) for each bracket are assigned as the uncertainties of the bracketed unknown analyses.

The plagioclase grains in all the 15 chondrules were analyzed in a third session (S3). The analytical conditions are similar to those described in Ushikubo et al. (2012). The $^{133}Cs^{+}$ primary ion beam was focused to a ~3 μm diameter spot at 20 pA. Secondary oxygen ions were detected simultaneously using one FC for $^{16}O^{-}$ and two electron multipliers (EMs) for $^{17}O^{-}$, and $^{18}O^{-}$, respectively. The FC for $^{16}O^{-}$ employed a 10^{11} ohm resistor. We analyzed two plagioclase grains in each of the chondrules from A 12236 and DOM 08006, and one plagioclase grain in each chondrule from Y-81020. Six to ten unknown analyses were bracketed by 8 analyses of an anorthite reference material PL3 from the Hachijo-jima volcano Allivalite (An = 95, $\delta^{18}O$ = 5.79‰; Matsuhisa, 1979), which was used for the instrumental bias correction. The averaged external reproducibilities of the bracketing standard PL3 were 0.4‰, 0.9‰, and 1.0‰ (2SD) for $\delta^{18}O$, $\delta^{17}O$, and $\Delta^{17}O$, respectively, which were assigned as the uncertainties of bracketed unknown analyses.

The mean oxygen isotope ratios of individual chondrules are calculated based on multiple olivine and pyroxene analyses, following the data reduction scheme from Hertwig et al. (2018) (see Supplementary Material 1 for more details).

2.4.2. SIMS Al-Mg isotope analysis

The Mg three-isotopes and $^{27}Al/^{24}Mg$ ratios of plagioclase grains in the 15 chondrules were collected in a fourth session (S4) using the MCFC mode. Analytical conditions are the same as described in Fukuda et al. (2021b) for melilite analyses in CAIs. A 2 nA $^{16}O_2^{-}$ primary ion beam was focused to a ~10 µm diameter spot, which was generated by the RF source with the power of 860W. Secondary ions ($^{24}Mg^+$, $^{25}Mg^+$, $^{26}Mg^+$, $^{27}Al^+$) were detected simultaneously with four FCs (L′2, C, H1, H′2). The typical $^{24}Mg^+$ and $^{27}Al^+$ count rates during measurement of the anorthite glass standard (MgO 1 wt.%) were 7.4×10^6 and 2.3×10^8 cps, respectively. Due to the relatively low secondary Mg^+ ion intensities, the MCFCs for $^{24,25,26}Mg^+$ signals each employed 10^{12} ohm resistors (Fukuda et al., 2021a) and the FC for $^{27}Al^+$ employed a 10^{11} ohm resistor. A single analysis took ~8 min, including 100 s of presputtering, ~80 s for automated centering of the secondary ion deflectors (DTFA-X and -Y), and 300 s of integration (10 s × 30 cycles) of the secondary ion signals. An instrumental bias on $\delta^{25}Mg$ was estimated by measuring the Mg isotopes of two synthetic anorthite glasses with 0.6 and 1 wt.% MgO, both of which have a $\delta^{25}Mg_{DSM\text{-}3}$ (per-mil deviation from Mg reference material DSM-3; Galy et al., 2003) of −1.77‰ (Kita et al., 2012). A relative sensitivity factor RSF = $[(^{27}Al^+/^{24}Mg^+)_{measured}/(^{27}Al/^{24}Mg)_{true}]$ was also evaluated by measuring $^{27}Al^+/^{24}Mg^+$ ratios on the two synthetic anorthite glasses.

The instrumental biases and RSFs of the two anorthite glasses were identical within uncertainties (Supplementary Table S5-1). Thus, only the anorthite glass with 1 wt.% MgO was used as a bracketing standard for instrumental bias and RSF corrections. Four to eight unknown analyses were bracketed by 6–8 analyses of the anorthite glass standard. Four to eight unknown analyses were bracketed by 6–8 analyses of the bracketing standard. The averaged external reproducibilities (2SD) of the raw measured $\delta^{25}Mg$, $\delta^{26}Mg$, and $\Delta^{26}Mg$ for the bracketing anorthite glass (1 wt.% MgO) were 0.36‰, 0.29‰ and 0.46‰, respectively.

The Mg three-isotopes and $^{27}Al/^{24}Mg$ ratios of olivine and pyroxene phenocrysts in the 15 chondrules were collected in a fifth session (S5) using the MCFC mode. The analytical conditions are similar to those described in Fukuda et al. (2020) and Siron et al. (2021a). A 1 nA $^{16}O_2^-$ primary ion beam was focused to a ~7 µm diameter spot, which was generated by the RF source with the power of 800W. Secondary ions ($^{24}Mg^+$, $^{25}Mg^+$, $^{26}Mg^+$, $^{27}Al^+$) were detected simultaneously with four FCs (L′2, C, H1, H′2) using a 10^{10} ohm resistor for $^{24}Mg^+$ and three 10^{11} ohm resistors for $^{25,26}Mg^+$ and $^{27}Al^+$. Counting times were the same as in the plagioclase analyses. Eight to fourteen unknown analyses were bracketed by 8 analyses of the bracketing standard SC-Ol. The typical secondary $^{24}Mg^+$ ion intensity when measuring SC-Ol was 2.0×10^8 cps. In addition to SC-Ol, 13 olivine and 5 pyroxene reference materials, whose Mg isotope ratios on the DSM-3 scale are reported in Fukuda et al. (2020), were measured to correct for instrumental bias. The averaged external reproducibilities (2SD) of the raw measured $\delta^{25}Mg$, $\delta^{26}Mg$, and $\Delta^{26}Mg$ values for the bracketing standard SC-Ol were 0.14‰, 0.27‰, and 0.07‰, respectively.

Data reduction procedures follow those described in Siron et al. (2021a) and are summarized in Supplementary Material 1.

2.5. Estimation of Al-Mg relative ages

The initial $^{26}Al/^{27}Al$ ratios, $(^{26}Al/^{27}Al)_0$, of the 15 chondrules were obtained from isochron regressions using Isoplot 4.15 (Model 1; Ludwig, 2012). Uncertainties for the reported $(^{26}Al/^{27}Al)_0$ values and relative ages are 95% confidence intervals. The relative ages are calculated as:

$$\Delta t\ (Myr) = \ln\left[\frac{(^{26}Al/^{27}Al)_{0,CAI}}{(^{26}Al/^{27}Al)_{0,chondrule}}\right] \times \frac{0.705}{\ln(2)} \tag{1}$$

using the canonical CV CAI $(^{26}Al/^{27}Al)_0$ of 5.25×10^{-5} (Jacobsen et al., 2008; Larsen et al., 2011) and the half-life of ^{26}Al (0.705 Ma; Nishiizumi, 2004).

3. RESULTS

The research data obtained in this study are documented in Supplementary Materials 2–6 and are summarized in Tables 1–3, including the locations of oxygen isotope analyses (Supplementary Material 2) and Al-Mg isotope analyses (Supplementary Material 3), oxygen isotope ratios of chondrule minerals (Supplementary Material 4), Mg isotope and $^{27}Al/^{24}Mg$ ratios of chondrule minerals (Supplementary Material 5), chemical compositions of chondrule minerals (Supplementary Material 6), mean oxygen isotope ratios and mean chondrule Mg#s (Table 1), average chemical compositions and excess silica components of plagioclase EPMA analyses (Table 2), and the $(^{26}Al/^{27}Al)_0$, $(\delta^{26}Mg)_0$*, and Al-Mg age values (Table 3).

3.1. Petrography and mineral chemistry

The A 12236 and DOM 08006 chondrules studied include porphyritic pyroxene (PP; less than 20% modal olivine), porphyritic olivine (PO; less than 20% modal pyroxene), porphyritic olivine-pyroxene (POP; between 20–80% modal olivine) (Jones, 1994), and Al-rich chondrules (Al_2O_3 > 10 wt.%; Bischoff and Keil, 1984) (Figs. 1 and 2), that all contain FeO-poor mafic minerals with high Mg#s (≥98.5; Table 1). The olivine and pyroxene proportions were roughly estimated from BSE images. The Mg#s of olivine and pyroxene grains within each chondrule are similar to each other (Fig. 3), consistent with the observation for FeO-poor chondrules from DOM 08006 (Davidson et al., 2019a) and other pristine chondrites (Ushikubo et al., 2012; Tenner et al., 2013, 2015; Schrader et al., 2017; Hertwig et al., 2018; Chaumard et al., 2018, 2021; Davidson et al., 2019b). No secondary anhydrous phases (e.g., nepheline) are observed in the chondrules studied.

3.1.1. A 12236 chondrules

Figure 1 shows BSE images of the five A 12236 chondrules studied here. Four of them (A21, A28, A184, A207; Fig. 1a–f) are PP chondrules and the other, A75, is a POP chondrule (Fig. 1g–h). They consist mostly of low-Ca pyroxene ($En_{94–99}Fs_{<2}Wo_{1–4}$), forsteritic olivine ($Fo_{\geq 99}$), anorthitic or near-anorthitic plagioclase ($An_{\geq 86}$), high-Ca pyroxene ($En_{60–66}Fs_{<2}Wo_{33–39}$), and FeNi-metal. In the four PP chondrules, the olivine grains are often enclosed by poikilitic low-Ca pyroxene (e.g., Fig. 1e–f). Chondrules A21 and A28 appear to have altered regions in their mesostases (e.g., Fig. 1d). We carefully avoided these altered regions for chemical, oxygen, and Al-Mg isotope analyses and only measured clean anorthite grains (Fig. 1b and d and Supplementary Materials 2 and 3). The POP chondrule A75 is mineralogically zoned (Fig. 1g), with large olivine crystals (Mg# = 99.5) and interstitial plagioclase in the core, and with minor amounts of high-Ca pyroxene and low-Ca pyroxene (Mg# = 99.4) in the outermost shell of the chondrule with poikilitically enclosed small olivine grains (Mg# = 99.2) (Fig. 1h).

3.1.2. DOM 08006 chondrules

Figure 2 shows BSE images of the six DOM 08006 chondrules studied here. Three of them (D41, D59, D109; Fig. 2a–c) are POP, while chondrules D10, D89, and D198 are PP, PO, and Al-rich chondrules, respectively (Fig. 2d–g). As for A 12236 chondrules, the six DOM chondrules consist of low-Ca pyroxene ($En_{95–99}Fs_{<2}Wo_{1–5}$), forsteritic olivine ($Fo_{\geq98}$), anorthitic or near-anorthitic plagioclase ($An_{\geq87}$), high-Ca pyroxene ($En_{58–64}Fs_{<2}Wo_{35–41}$), and FeNi-metal. The Al-rich chondrule D198 also contains corroded spinel grains (Fig. 2g). The constituent phases of the six chondrules escaped aqueous alteration, as evidenced by the lack of phyllosilicates, consistent with the observations of Davidson et al. (2019a).

3.1.3. Plagioclase compositions

The chemical compositions (e.g., An content and MgO concentration) as well as the abundances of excess silica ($[\ ]Si_4O_8$) within the plagioclase grains were determined in all 15 chondrules from A 12236, DOM 08006, and Y-81020 and can be used as an indicator for the extent of plagioclase secondary alteration (Tenner et al., 2019). Plagioclase from the A 12236 and DOM 08006 chondrules contains up to 9% and up to 6% of the excess silica endmember, respectively (Table 2, Fig. 4a and b). The range of excess silica in DOM 08006 is consistent with that reported in Davidson et al. (2019a). For A 12236 and DOM 08006 chondrule plagioclase, the range of excess silica, as well as An contents (86.5 to 99.4) and MgO concentrations (0.5 to 1.3 wt.%; Fig. 4d and e) are similar to those from Acfer 094 and CR chondrites that experienced minimal parent body alteration (Tenner et al., 2019; Davidson et al., 2019b). For Y-81020 chondrule plagioclase, the abundances of excess silica (up to 5%; Fig. 4c) and MgO concentrations (0.8 to 1.0 wt.%; Fig. 4f) are comparable to those of A 12236 and DOM 08006 chondrules. The An contents of Y-81020 chondrule plagioclase grains are also similar to those of A 12236 and DOM 08006. In detail, chondrule Y175 exhibits slightly lower An contents than those of the rest of chondrules we studied, down to 79.7 (Fig. 4c and f), but within the range of chondrule plagioclase from CR chondrites (79.3–99.9; Tenner et al., 2019).

3.2. TEM observation of plagioclase

Plagioclase grains with clear excess silica in chondrule D89 (up to ~6%; Fig. 2e) were further evaluated by TEM. The ultrathin section manufactured from chondrule D89 is composed of two plagioclase grains and an interstitial low-Ca pyroxene grain (Fig. 5a–c). The plagioclase grains are chemically homogeneous (Fig. 5c and Supplementary Fig. S3) and do not contain mineral inclusions, even down to the nanometer-scale (Fig. 5b–d). These TEM observations are broadly consistent with chondrule plagioclase from the primitive Acfer 094 and CR chondrites (Tenner et al., 2019).

The space groups of the plagioclase grains in chondrule D89, which have molar [Ca]/[Na+Ca] = 0.99, were determined using the systematic absences of diffraction spots due to crystal symmetry in their SAED patterns. The SAED pattern taken from one plagioclase grain only shows reflections with indices of $h + k + l = 2n$, where n is an integer, which is consistent with a body-centered lattice (Fig. 5e) and with the space group $I\bar{1}$. The SAED pattern from the other plagioclase grain also shows extra faint reflections with indices of $h + k + l = 2n + 1$ (Fig. 5f) that suggest that it has a primitive lattice (space group $P\bar{1}$). Therefore, the D89 plagioclase is in a transitional state in the $I\bar{1}$ to $P\bar{1}$ phase transition. According to the phase diagram in the system $NaAlSi_3O_8$-$CaAl_2Si_2O_8$, the $I\bar{1}$ and $P\bar{1}$ phases are stable above and below ~200°C, respectively, for pure anorthite composition (Smith, 1984). Although the symmetry relations of Si-rich anorthite are poorly understood, its transition temperature is probably higher than 200°C due to the elevated albite component in plagioclase (Smith, 1984).

3.3. Oxygen isotope systematics

3.3.1. A 12236 and DOM 08006

Ten out of the eleven chondrules from A 12236 and DOM 08006 (except for chondrule A75 from A 12236) show internally homogeneous oxygen isotope ratios among coexisting olivine and pyroxene (Fig. 6). The mean oxygen isotope ratios of chondrules, which are calculated from their constituent olivine and pyroxene spot analysis data, are shown in Fig. 7a, and are interpreted to represent the average oxygen isotope ratios of the final chondrule melt (e.g., Ushikubo et al., 2012). On an oxygen three-isotope diagram, the mean oxygen isotope ratios of the 10 chondrules plot between the Primitive Chondrule Minerals (PCM; Ushikubo et al., 2012) and the Carbonaceous Chondrite Anhydrous Mineral (CCAM; Clayton et al., 1977) lines (Fig. 7a). Their mean $\Delta^{17}O$ values range from −6.4 ± 0.2‰ to −4.1 ± 0.2‰ (2σ), consistent with values from other CO and CM chondrules with Mg# ≥98 (Fig. 8b; Tenner et al., 2013; Chaumard et al., 2018, 2021) and the bulk oxygen isotopic composition of A 12236 (−4.75‰) (Kimura et al., 2020). Aside from chondrule A75, it is noted that plagioclase in the 10 chondrules are similar in oxygen isotope ratios to their coexisting olivine and pyroxene (Fig. 6).

The oxygen isotope ratios of minerals in chondrule A75 are systematically ^{16}O-depleted compared to the rest of the chondrules we investigated and exhibit systematic variations among coexisting minerals (Fig. 7a). Specifically, large olivine grains in the core (Fig. 1g) exhibit homogenously ^{16}O-depleted compositions ($\Delta^{17}O$ = −0.8 ± 0.5‰; 2SD), while pyroxene grains in the outermost shell are slightly heterogeneous and comparatively

^{16}O-rich (Δ^{17}O = −1.8 ± 0.9‰; 2SD). Further, the interstitial plagioclase exhibits more ^{16}O-rich compositions (Δ^{17}O = −3.5 ± 0.8‰; 2SD).

3.3.2. Y-81020 plagioclase

We also measured the oxygen isotope ratios of plagioclase grains in the four chondrules from Y-81020. The grains have oxygen isotope ratios that are consistently higher to various degrees in both δ^{18}O and Δ^{17}O compared to the coexisting olivine and pyroxene phenocrysts measured by Tenner et al. (2013) (Fig. 8). For instance, a plagioclase analysis of Y24 has slightly heavier oxygen isotope ratios relative to the coexisting olivine and pyroxene grains (Fig. 8b), while that of Y175 is isotopically much heavier than the coexisting pyroxene grains (Fig. 8d).

3.4. Al-Mg systematics

All plagioclase analyses show resolvable δ^{26}Mg* values ranging from 0.7 ± 0.3‰ to 2.5 ± 0.6‰ (2σ), with corresponding ^{27}Al/^{24}Mg ratios ranging from 25 to 67 (Supplementary Table S5-5). Olivine and pyroxene exhibit a limited variation in δ^{26}Mg* values ranging from −0.13 ± 0.12‰ to 0.18 ± 0.08‰ (2σ) with ^{27}Al/^{24}Mg ratios ≤ 0.2 (Supplementary Table S5-5). The Al-Mg isochron diagrams are shown in Fig. 9. Chondrule mineral isochrons have mean squared weighted deviations (MSWD) of 0.2 and 1.5, below the threshold value of 2.5 for rejecting straight-line isochrons, according to Brooks et al. (1972).

Chondrules from DOM 08006 and A 12236, except for chondrule A75, show similar ranges in (^{26}Al/^{27}Al)$_0$ from (3.6 ± 0.9) × 10^{-6} to (5.3 ± 0.6) × 10^{-6} and (3.5 ± 0.9) × 10^{-6} to (4.7 ± 0.5) × 10^{-6} (95% confidence intervals), respectively (Fig. 9a–j). Chondrule A75, the mineralogically zoned chondrule with heterogeneous and relatively ^{16}O-depleted isotopic signatures, has an exceptionally high $(^{26}Al/^{27}Al)_0 = (8.0 \pm 0.7) \times 10^{-6}$ (Fig. 9c). The Al-Mg ages of chondrules from DOM 08006 range from 2.33 $^{-0.10}/_{+0.11}$ Ma to 2.72 $^{-0.22}/_{+0.28}$ Ma after CAIs. The chondrules from A 12236, except for A75, exhibit similar Al-Mg ages ranging from 2.45 $^{-0.11}/_{+0.12}$ Ma to 2.76 $^{-0.23}/_{+0.30}$ Ma after CAIs. Chondrule A75 has the oldest Al-Mg age (1.92 ± 0.09 Ma after CAIs) among the chondrules we studied, and is ~0.5–0.8 Ma older than the other four chondrules from A 12236.

The four Y-81020 chondrules we reanalyzed show a narrow range in $(^{26}Al/^{27}Al)_0$ ranging from $(4.9 \pm 1.0) \times 10^{-6}$ to $(6.0 \pm 0.6) \times 10^{-6}$ (Fig. 9k–n), corresponding to Al-Mg ages ranging from 2.21 $^{-0.10}/_{+0.11}$ Ma to 2.41 $^{-0.19}/_{+0.24}$ Ma after CAIs. Our Al-Mg ages are systematically younger by ~0.1–0.4 Ma than those reported in Kurahashi et al. (2008) (Fig. 10).

4. DISCUSSION

4.1. Parent body alteration effects on Al-Mg systematics of chondrule plagioclase

4.1.1. Pristine nature of chondrule plagioclase in Asuka 12236 and DOM 08006

Parent body alteration, such as thermal metamorphism, could potentially disturb Al-Mg systematics of chondrule plagioclase/glassy mesostasis (e.g., Sano et al., 2014; Nagashima et al., 2017). For example, Nagashima et al. (2017) investigated Al-Mg systematics of two chondrules from Yamato-980145 (CV3.1) that experienced less thermal metamorphism than most other CV chondrites, such as Allende (CV3.6) (Komatsu et al., 2014). Plagioclase grains in the two chondrules show no resolvable excesses in ^{26}Mg despite the relatively low petrologic subtype of Yamato-980145. Since plagioclase in one of the chondrules is replaced by a nepheline-like phase, Nagashima et al. (2017) concluded that the lack of excess ^{26}Mg is most likely due to disturbance of the Al-Mg systematics by thermal metamorphism at relatively high temperatures (≥400°C). Thus, it is important to evaluate any parent body alteration effects on Al-Mg systematics, even for lower petrologic subtypes of ~3.1.

Tenner et al. (2019) pointed out that the mineral chemistry of plagioclase in FeO-poor chondrules appears to correlate with the extent of thermal metamorphism. They found that chondrule plagioclase from the least metamorphosed chondrites (L/LL3.01–3.05, ungrouped C3.00, CR2–3) share a similar mineral chemistry, such as the presence of excess silica, high An contents, and high MgO concentrations, whereas plagioclase from chondrites of higher petrologic subtypes (≥3.1) mostly lack silica excesses and show reduced An contents and MgO concentrations. On the basis of these observations, Tenner et al. (2019) proposed that the mineral chemistry of plagioclase can be used as a tool to evaluate whether Al-Mg systematics in plagioclase were likely disturbed by thermal metamorphism. In this study, we show that chondrule plagioclase grains from A 12236 and DOM 08006 exhibit mineral chemistries that are similar to those of plagioclase from the least metamorphosed chondrites (i.e., presence of excess silica, high An contents and MgO concentrations; Fig. 4a and b, d and e), which are consistent with A 12236 and DOM 08006 to be classified as CM2.9 and CO 3.00–3.01, respectively (Tenner et al., 2018b; Davidson et al., 2019a; Kimura et al., 2020). An experimental study has shown that excess silica is incorporated at high temperatures (~1100 to 1500 °C; Longhi and Hays, 1979). Therefore, the presence of excess silica in chondrule plagioclase indicates that the high-temperature history of chondrules was preserved and that plagioclase did not undergo further alteration after crystallizing from the melt. This is consistent with the presence of high symmetry plagioclase (grain1) in chondrule D89 from DOM 08006 (body-centered anorthite with space group $I\bar{1}$; Fig. 5e), suggesting high-temperature crystallization and rapid cooling. In addition, the plagioclase grain in chondrule D89 shows no evidence of replacement by other mineral phases during alteration, down to nanometer-scale (Fig. 5b–d), consistent with observations in chondrules from the least metamorphosed chondrites (Tenner et al., 2019). These observations indicate that chondrule plagioclase from A 12236 and DOM 08006 have experienced at most minimal thermal metamorphism on their parent bodies. This is consistent with petrographic observations for A 12236 (Kimura et al., 2020).

Oxygen isotope ratios of plagioclase are particularly sensitive to parent body processes (e.g., fluid-rock interaction; Krot et al., 2019). For chondrules from chondrites with minimal hydrothermal alteration, such as Acfer 094 and many CR chondrites, oxygen isotope ratios of plagioclase/glassy mesostasis are similar to those of coexisting olivine and pyroxene phenocrysts (Ushikubo et al., 2012; Tenner et al., 2015; Schrader et al., 2017). In contrast, this is not the case for chondrules from chondrites that have undergone hydrothermal alteration, in which oxygen isotope ratios of plagioclase/glassy mesostasis tend to be enriched in heavier isotopes relative to those of coexisting olivine and pyroxene (Maruyama et al., 1999; Maruyama and Yurimoto, 2003; Akaki et al., 2007; Chaussidon et al., 2008; Kita et al., 2010; Rudraswami et al., 2011; Wakaki et al., 2013; Krot and Nagashima, 2016; Hertwig et al., 2019b; Zhang et al., 2020). It is likely that chondrule plagioclase in these meteorites was subjected to oxygen isotope exchange with metasomatic fluids in their parent bodies (e.g., Krot and Nagashima, 2016). In this study, we find that oxygen isotope ratios of plagioclase grains in chondrules from A 12236 and DOM 08006, except for chondrule A75, are similar to those of coexisting olivine and pyroxene phenocrysts (Fig. 6a–k), suggesting only minimal hydrothermal alteration of studied chondrules on CM and CO parent bodies. We note, however, that the presence of Fe oxy-hydride in matrix (Davidson et al., 2019a) indicates that DOM 08006 has undergone minor amounts of parent body alteration.

Furthermore, the some glassy mesostases in DOM 08006 chondrules show evidence of parent body alteration; for example, Shimizu et al. (2021) suggest that the high δD values in DOM 08006 mesostases could have been inherited from surrounding matrix materials during parent body alteration. As such, we targeted anorthitic plagioclase grains that are more resistant to parent body alteration and we do not find any evidence of alteration in terms of oxygen isotopes and mineral chemistry. Future oxygen isotope analyses of glassy mesostases in DOM 08006 chondrules may reveal the extent of parent body alteration in more detail.

Although the plagioclase in chondrule A75 exhibits oxygen isotope disequilibrium with coexisting olivine and pyroxene (Fig. 6c), the observed oxygen isotopic and petrographic characteristics do not support alteration of A75 by parent body processes. First, the oxygen isotope ratios of the plagioclase grains are distributed along a slope ~1 line and are enriched in ^{16}O relative to coexisting olivine and pyroxene, both of which are inconsistent with trends observed in chondrules that have undergone aqueous/hydrothermal alteration. Instead, we suggest that the oxygen isotope ratios and petrographic characteristics of chondrule A75 minerals reflect incomplete melting of isotopically distinct precursors. For example, the poikilitic textures of small olivine grains within the low-Ca pyroxene rim (Fig. 1h) suggest that this chondrule experienced gas-melt exchange and dissolution of olivine during chondrule formation (e.g., Tissandier et al., 2002; Libourel et al., 2006; Marrocchi et al., 2018a; Barosch et al., 2019). We therefore interpret the olivine in the core (Fig. 1g) as relict grains that retained the oxygen isotope ratios of the precursor dust (Tenner et al., 2018a and references therein; Marrocchi et al., 2018a), whereas low-Ca pyroxene and interstitial plagioclase crystallized from a chondrule melt that interacted with an isotopically distinct environment. Therefore, we conclude that the observed oxygen isotope disequilibrium in chondrule A75 is not related to parent body alteration, but instead reflects primary oxygen isotope heterogeneity among its constituent minerals.

Altogether, we find no evidence of parent body alteration of chondrule plagioclase from A 12236 and DOM 08006, suggesting their Al-Mg systematics are undisturbed. This is consistent with well-defined isochron regressions of all the chondrules with acceptable MSWD values (Table 3). Therefore, the obtained $(^{26}Al/^{27}Al)_0$ values represent the initial $^{26}Al/^{27}Al$ ratios at the formation of individual chondrules, meaning their Al-Mg ages confidently represent their formation time in the solar protoplanetary disk.

4.1.2. Y-81020 plagioclase; not as pristine as A 12236 and DOM 08006 plagioclase

Regarding mineral chemistry, plagioclase in the four chondrules from Y-81020 is similar to plagioclase from the least metamorphosed chondrites, i.e., excess silica is present in most analyses (up to ~5%) and An contents as well as MgO concentrations are high (Fig. 4c and f), suggesting that primary Al-Mg systematics are preserved. However, in contrast to the results from A 12236 and DOM 08006, the oxygen isotope ratios of plagioclase in Y-81020 chondrules are systematically higher in both $\delta^{18}O$ and $\Delta^{17}O$ compared to coexisting olivine and pyroxene (Fig. 8a–d), indicating oxygen isotope exchange between plagioclase and an ^{16}O-poor component in the parent body. The oxygen isotope ratios of plagioclase in Y24, Y71, and Y175 plot on a linear regression line with a slope of ~0.7 that was obtained for bulk CM chondrites and mineral separates of Murchison (CM2) (dotted line in Fig. 8a–d). This line is considered to represent a mixing line between anhydrous silicate components (i.e., chondrules) and secondary minerals formed by a low temperature fluid (i.e., phyllosilicates) (Clayton and Mayeda, 1984, 1999; see also Chaumard et al., 2018). This suggests that chondrule plagioclase in Y-81020 experienced various degrees of oxygen isotope exchange with ^{16}O-poor fluids on the parent body.

However, in addition to plagioclase chemistry, there are several observations that point to a limited effect of this alteration on the Al-Mg systematics. First, all plagioclase analyses (N = 21) of the four Y-81020 chondrules show clear excess of ^{26}Mg. Second, the Al-Mg isochrons do not show any evidence of disturbance (i.e., MSWDs close to 1). Third, the Al-Mg systematics of chondrule plagioclase from hydrothermally altered Kaba (CV3.1) were found to be undisturbed (Nagashima et al., 2017), although the oxygen isotope ratios of plagioclase in Kaba chondrules are systematically enriched in heavier isotopes relative to those of coexisting olivine and pyroxene (Krot and Nagashima, 2016; Hertwig et al., 2019b). Importantly, the degree of heavy-isotope enrichment in chondrule plagioclase from Kaba ($\delta^{18}O$ up to ~15‰) is higher than in Y-81020 ($\delta^{18}O$ up to ~5‰), suggesting that alteration of Kaba chondrules was more extensive at higher water/rock ratios and/or lower temperature. Thus, undisturbed Al-Mg systematics of Kaba chondrules support the interpretation that hydrothermal alteration did not affect Al-Mg systematics of Y-81020 chondrule plagioclase. We note, however, that chondrule plagioclase from Y-81020, compiled in Tenner et al. (2019), has on average a slightly lower abundance of excess silica and a lower An content compared to Acfer 094 and CR chondrites. In summary, chondrule plagioclase from Y-81020 (CO3.05) is not as pristine as plagioclase in A 12236 and DOM 08006, but the Al-Mg systematics of plagioclase in Y-81020 chondrules are, nonetheless, likely undisturbed.

4.2. Distinct chondrule-forming environments: Constraints from mineral chemistry and oxygen isotopes

Mg#s are a useful measure of redox states during chondrule formation since these are controlled by metal-silicate equilibria (Ebel and Grossman, 2000). The high Mg#s of chondrules studied here (≥98.5) correspond to formation at reduced conditions, 3–4 log units below the iron-wüstite (IW) buffer (Tenner et al., 2015). A plot of mean $\Delta^{17}O$ values of individual chondrules versus their Mg#s reveals a dichotomy between NC and CC chondrules (Fig. 7). NC chondrules are ^{16}O-depleted relative to CC chondrules (Fig. 7a; e.g., Kita et al., 2010; Weisberg et al., 2011, 2021; Nagashima et al., 2015; Miller et al., 2017; Siron et al., 2021a) and show a narrow range of $\Delta^{17}O$ values (typically from −0.5‰ to +1.0‰) with variable Mg#s (Fig. 7b). In contrast, $\Delta^{17}O$ values of CC chondrules are more variable (typically −8‰ to +1‰) and show characteristic trends when plotted against Mg#s (Ushikubo et al., 2012; Tenner et al., 2013, 2015, 2017; Schrader et al., 2013, 2014, 2017; Chaumard et al., 2018, 2021; Hertwig et al., 2018, 2019b; Marrocchi et al., 2019). The distinct $\Delta^{17}O$-Mg# systematics in NC and CC chondrules indicate distinct chondrule-forming environments (e.g., differences in redox states and precursor materials) for both meteorite groups. As mentioned in the Introduction, O, Cr, and Ti isotope systematics of chondrules indicate that NC and CC chondrules formed in distinct disk regions, probably in the inner and outer Solar System, respectively (Gerber et al., 2017; Schneider et al., 2020). Note that $\Delta^{17}O$ values of FeO-rich (type II) chondrules in CR chondrites are similar to those of NC chondrules ($\Delta^{17}O$ ~0‰; e.g., Schrader et al., 2013, 2014, 2017, 2018a; Tenner et al., 2015). In an oxygen three isotope plot, however, they are distinct from each other. For example, Tenner et al. (2017) show that type II chondrules in CR chondrites plot on the PCM line, but OC chondrules are fractionated to the left side of the PCM line.

Among CCs, CR chondrites contain chondrules that show a well-defined correlation of increasing $\Delta^{17}O$ with decreasing Mg# (Fig. 7b; Tenner et al., 2015). This trend can be explained by variable proportions of ^{16}O-rich anhydrous dust and ^{16}O-depleted H_2O ice among individual chondrule precursors and open-system formation of chondrules between melt and gas (Tenner et al., 2015; 2018a; see also Supplementary Material 1). On the basis of mass balance calculations, it is inferred that FeO-poor chondrules from CR chondrites formed in a dust enriched protoplanetary disk compared to solar abundance gas (~100–200 × dust enrichment) at relatively dry conditions (0–0.8 times the abundance of H_2O in CI chondritic dust) (Tenner et al., 2015). While the distribution of Mg# in CR chondrules and those of comet 81P/Wild 2 silicate particles are different (Frank et al., 2014), their Δ^{17}O-Mg# relationships show a significant similarity (Nakashima et al., 2012; Defouilloy et al., 2017). In addition, anhydrous interplanetary dust particles (IDPs) that are likely originated from icy outer Solar System comets also exhibit Δ^{17}O-Mg# systematics that are similar to those of CR chondrules (Zhang et al., 2021). Furthermore, CR chondrules have distinct Mg and Cr isotope systematics compared to those of CM and CV chondrites, which are similar to those of chondrules from other metal-rich carbonaceous chondrites including CH and CBs (Olsen et al., 2016; van Kooten et al., 2016, 2020). On the basis of the observations, van Kooten et al. (2016, 2020) proposed that chondrules in CR, CH, and CB chondrites formed in an environment that was distinct from that of other CCs and probably located outside the formation regions of chondrules from CM, CO, and CV chondrites. This scenario is consistent with the model that was proposed by Desch et al. (2018) based on the abundances of refractory elements and inclusions in each chondrite group. They concluded that the CR chondrite parent body accreted at the outer region further than where CM, CO, and CV chondrites accreted (see Fig. 10 in Desch et al., 2018). On the basis of the redox states and H isotopic systematics of bulk meteorites, Sutton et al. (2017) suggested that carbonaceous chondrites including CR are unlikely to have come from comets, and the regions where they accreted were probably not beyond 7 AU. By considering the rapid accretion of the majority of CR chondrules into the parent body after their formation (Budde et al., 2018; Tenner et al., 2019), we infer that the CR chondrule-forming region was outside the CM, CO, and CV chondrule-forming regions, but not beyond ~7 AU.

FeO-poor chondrules from CM, CO, CV, and Acfer 094 chondrites exhibit similar Δ^{17}O-Mg# systematics (Fig. 7b), suggesting they formed in a similar or even a common environment. Such an environment is predicted to have been moderately dust-enriched and relatively anhydrous (~50–100 × dust enrichment compared to solar abundance gas and less than 0.6 times the abundance of H_2O in CI chondritic dust; Fig. 7b), like proposed for the CV chondrule-forming environment (Hertwig et al., 2018, 2019b).

In NC chondrules, the near-constant $\Delta^{17}O$ values with variable Mg#s (~60–100) suggest variable redox conditions within respective chondrule-forming environments, potentially due to significant ranges of dust-to-gas ratios (e.g., ~100–10,000 × dust enrichment compared to solar abundance gas; Kita et al., 2010). The near-constant $\Delta^{17}O$ values among NC chondrules also suggest bulk oxygen isotope ratios of respective chondrule precursors were constant (Tenner et al., 2018a). Considering that Cr-Ti isotope systematics in NC chondrules are similar to those of Earth and Mars (Gerber et al., 2017; Schneider et al., 2020), these environments likely existed within the inner part of the solar protoplanetary disk.

On the basis of these observations, we infer that there were distinct chondrule-forming environments for (*i*) non-carbonaceous, (*ii*) CV, CO, CM, and Acfer 094, and (*iii*) CR chondrite chondrules, which are interpreted as having been located in the inner, outer, and outermost (but not beyond ~7 AU) parts, respectively, of the solar protoplanetary disk.

4.3. Mineralogically-controlled O-isotope heterogeneity recorded in chondrule A75: Evidence for mixing of NC-CC materials?

Among the CM and CO chondrules we studied, chondrule A75 is distinct because of its heterogeneous O-isotope ratios ($\Delta^{17}O$ = ~−4% to 0‰; Fig. 6c) and the presence of ^{16}O-depleted relict olivine grains ($\Delta^{17}O = -0.8 \pm 0.5$‰; 2SD), suggesting that its formation condition is dissimilar from that of the majority of CC chondrules. Rare FeO-poor chondrules/relict olivine grains with ^{16}O-depleted signatures ($\Delta^{17}O$ = ~0‰) have also been found in very low abundances in other CCs: ungrouped C (Ushikubo et al., 2012; Tenner et al., 2017), CV (Hertwig et al., 2018; 2019b; Williams et al., 2020), CO (Tenner et al., 2013), CM and CM-related (Marrocchi et al., 2018a; Schrader et al., 2020; Chaumard et al., 2021). Previous studies also proposed that some of the ^{16}O-depleted chondrules/relict olivine grains in CCs formed in the inner Solar System (Tenner et al., 2017; Schrader et al., 2020). This interpretation is supported by Williams et al. (2020) that conducted Cr-Ti-O isotope analyses of individual chondrules from Allende (CV) and Karoonda (CK) chondrites. Williams et al. (2020) found that Allende and Karoonda chondrules with relatively ^{16}O-depleted oxygen isotope ratios ($\Delta^{17}O$ = ~−4‰ to 0‰), which plot above the PCM line in the oxygen three isotope diagram, have Cr isotope ratios that are similar to those of non-carbonaceous meteorites (see Fig. 2 in Williams et al., 2020), indicating that some ^{16}O-depleted chondrules in CCs likely formed in the NC chondrule-forming environments and were transported to the CC accretion region. Note that the presence of some ^{16}O-depleted, FeO-poor chondrules in CV, CO, CM, and Acfer 094 chondrites, in contrast to their rarity in CR chondrites (e.g., Schrader et al., 2020), is consistent with these chondrite parent bodies having formed in between non-carbonaceous and CR chondrite accretion regions.

Based on oxygen isotope systematics of chondrule A75, we infer that this chondrule formed by melting of the mixture of NC and CC materials. This chondrule contains ^{16}O-depleted relict olivine grains ($\Delta^{17}O = -0.8 \pm 0.5$‰; 2SD) with oxygen isotope ratios similar to those in NC chondrules. In contrast, pyroxene and plagioclase in chondrule A75 are more ^{16}O-rich than the relict olivine grains (Fig. 6c), which are likely the characteristic of the CC chondrules. On the basis of these observations, the formation scenario of A75 can be envisioned as follows: the ^{16}O-depleted relict olivine grains could have initially formed in the NC chondrule-forming region, were then transported to the CC chondrule-forming region, became intermixed with other CC-chondrule-like precursors, and then remained partially or fully intact during the final chondrule melting event. If correct, the final melting event that produced the pyroxene shell and determined the $(^{26}Al/^{27}Al)_0$ of the interstitial plagioclase occurred in a different locale relative to where NC chondrules formed, which is more likely the outer Solar System. However, we do not infer that the region where the final melting occurred was the same as the region where the majority of CC chondrules formed, which will be discussed later.

4.4. Distribution of ^{26}Al in the early Solar System

The distribution of ^{26}Al in the early Solar System (i.e., homogeneous vs heterogeneous) is actively debated, although there is no general consensus on this topic (e.g., Kita et al., 2013; Sanborn et al., 2019; Bollard et al., 2019; Gregory et al., 2020). There are several studies that argue against a homogeneous distribution of ^{26}Al (Larsen et al., 2011; Schiller et al., 2015; Bollard et al., 2019). Although the possible heterogeneity proposed by Larsen et al. (2011) has been questioned by subsequent studies (Wasserburg et al., 2012; Kita et al., 2013; see also Sanborn et al., 2019 for more discussion), Bollard et al. (2017, 2019) showed discrepancies between Al-Mg and U-corrected Pb-Pb ages of CAIs and chondrules, suggesting a heterogeneous distribution of ^{26}Al. However, chondrule Pb-Pb ages reported in Bollard et al. (2017) were obtained by regressions of a series of acid leachates, which could represent mixing lines that reflect multiple processes or precursors, as opposed to true isochrons (Blichert-Toft et al., 2020; see also Siron et al. 2021a for more discussion). Schiller et al. (2015) also argued in favor of a heterogeneous distribution of ^{26}Al based on the discrepancy between Al-Mg and U-corrected Pb-Pb ages of CAIs and angrites. However, potential disturbances in the U-Pb and possibly Al-Mg systematics of the angrite meteorite Sahara 99555 have been pointed out by Amelin (2008). Sanborn et al. (2019) also questioned the robustness of the Al-Mg system of D'Orbigny because of its complex petrologic history base on apparent disturbance of the Sm-Nd systems (Sanborn et al., 2015). In addition, the argument by Schiller et al. (2015) might not be valid if age heterogeneity exits in the CAI population. As discussed in detail by Sanborn et al. (2019), variations in U-corrected Pb-Pb ages of CAIs (Amelin et al., 2010; Bouvier et al., 2011; Connelly et al., 2012) should be considered as an open question. Furthermore, individual CAIs also show variations in their inferred $^{26}Al/^{27}Al$ ages (Kawasaki et al., 2020 and references therein), which necessitates further combined Al-Mg and U-corrected Pb-Pb analyses of individual CAIs in order to fully evaluate the heterogeneity of ^{26}Al in the early Solar System.

A homogeneous distribution of ^{26}Al has also been proposed by several studies (e.g., Villeneuve et al., 2009; Kita et al., 2013; Kruijer et al., 2014; Mishra and Chaussidon, 2014; Schrader et al., 2017; Budde et al., 2018; Luu et al., 2019; Gregory et al., 2020). In particular, the agreement of Al-Mg and Hf-W ages of angrites and chondrules from CV and CR chondrites supports a homogeneous distribution of ^{26}Al in the early Solar System (Budde et al., 2016, 2018; Nagashima et al., 2017; Schrader et al., 2017; Tenner et al., 2019). We also note that the Pb-Pb ages of pooled chondrules from CV and CR chondrites are in agreement with their Al-Mg and Hf-W ages (Amelin et al., 2002; Amelin and Krot, 2007; Connelly et al., 2008; Connelly and Bizzarro, 2009; Budde et al., 2016b, 2018; Schrader et al., 2017: Nagashima et al., 2017; see also Kruijer et al., 2020). Taking all of this into consideration, we cannot rule out the possibility of heterogeneous distribution of ^{26}Al, but we estimate Al-Mg ages of chondrules under the assumption that ^{26}Al was homogeneously distributed in the early Solar System. By doing so, we use the canonical value of 5.25×10^{-5} (Jacobsen et al., 2008; Larsen et al., 2011) as a reference value, which represents the initial $^{26}Al/^{27}Al$ ratio at the time of earliest Al/Mg fractionation in the CV CAI-forming region (e.g., Kita et al., 2013). If this assumption is not valid, then our Al-Mg data constrain the initial abundance of ^{26}Al at the time of chondrule formation as an upper limit of ^{26}Al concentration for their parent asteroid. ^{26}Al is one of the dominant heat sources for thermal evolution of early-formed planetary bodies (e.g., Grimm and McSween, 1993; Ghosh et al., 2006; Hevey and Sanders, 2006; Wakita and Sekiya, 2011; Lichtenberg et al., 2016). Since chondrule formation must have predated accretion of their parent asteroids, our data constrain an upper limit of ^{26}Al available for heating up their parent asteroids (e.g., Nagashima et al., 2018), which is an important parameter for reconstructing the thermal evolution of asteroids in the outer Solar System.

4.5. Revision of Al-Mg ages of CO chondrules: Younger than previously determined

Previous studies determined Al-Mg ages of the 28 chondrules from the Y-81020 CO3.05 chondrite, ranging from ~1.7 to 3.0 Ma after CAIs (Yurimoto and Wasson, 2002; Kunihiro et al., 2004; Kurahashi et al., 2008). Among them, 22 chondrules were initially measured by Kurahashi et al. (2008), which include the four chondrules we reanalyzed in this study (Y20, Y24, Y71, Y175). Importantly, the four chondrules we reanalyzed show systematically younger ages (2.21 $^{-0.10}/_{+0.11}$ Ma to 2.41 $^{-0.19}/_{+0.24}$ Ma) compared to results of Kurahashi et al. (2008) (1.83 $^{-0.51}/_{+1.01}$ Ma to 2.29 $^{-0.25}/_{+0.32}$ Ma) (Fig. 10). We hypothesize that the systematic difference between the two datasets is due to an inaccuracy of the Al-Mg data acquired by Kurahashi et al. (2008), related to instrument operation that employed a single EM in pulse counting mode. Data for the four chondrules obtained by Kurahashi et al. (2008) have ^{27}Al/^{24}Mg ratios that are similar to our new data, but their δ^{26}Mg* values are systematically higher by ~0.5‰, corresponding to higher (^{26}Al/^{27}Al)$_0$ values for their isochron regression lines. We suspect that the higher δ^{26}Mg* values from Kurahashi et al. (2008) could be due to an inaccurate correction of the SIMS instrumental bias on δ^{26}Mg*. As clearly seen in Mg isotope analyses of pyroxene standards (Supplementary Fig. S2), the raw measured δ^{26}Mg* values of terrestrial standards are not always zero within uncertainties, meaning that we need to evaluate the potential instrumental bias on δ^{26}Mg* for matrix-matched standards and correct it for unknown analyses. In fact, previous SIMS studies have shown there can be slight negative biases on raw measured $\delta^{26}Mg^*$ values of plagioclase standard analyses (e.g., −0.41 ± 0.25‰ (2SE) and −1.47 ± 0.26‰ (2SD) for the mono-collection EM analyses in Tenner et al., 2019 and Kita et al., 2012, respectively). Whereas Kita et al. (2012) and Tenner et al. (2019) analyzed standards multiple times during sessions and corrected for these offsets to accurately determine the unknown $\delta^{26}Mg^*$ values, Kurahashi et al. (2008) did not. In turn, this lack of correction could have led to systematically higher $\delta^{26}Mg^*$ values from Kurahashi et al. (2008), relative to the values determined here. In this study, repeated analyses of matrix-matched plagioclase standards were deployed to ensure the accuracy of Mg isotope ratios (Siron et al., 2021a), and the determined offset was corrected by the standard bracketing procedure. Thus, we conclude that the Al-Mg ages reported in Kurahashi et al. (2008) are systematically biased towards older ages. For the following discussion, we therefore only consider Al-Mg ages of the reanalyzed four chondrules. Overall, we find that Al-Mg ages of the ten CO chondrules (6 from DOM 08006 and 4 from Y-81020) range from ~2.2 to 2.7 Ma after CAIs, and none of our analyzed CO chondrules are older than 2.2 Ma after CAIs.

4.6. Time and duration of chondrule formation: Constraints from high precision Al-Mg chronology

Our high precision Al-Mg analyses reveal a short duration of CO type I chondrule formation (~2.2–2.7 Ma after CAIs; Fig. 11a). Furthermore, CM chondrules, except for the chondrule A75, show a similar range of Al-Mg ages (~2.4–2.8 Ma after CAIs; Fig. 11a) and have similar chemical properties (Mg# >98.5 and plagioclase chemistry) as well as oxygen isotope ratios (Fig. 7), suggesting that CO and CM chondrules formed in similar environments (Schrader and Davidson, 2017; Chaumard et al., 2018) at a similar time (~2.2–

2.8 Ma after CAIs). Importantly, the formation times of CO and CM chondrules are indistinguishable from those of the majority of CV and Acfer 094 chondrules (Fig. 11a).

Chondrule A75 that contains ^{16}O-depleted relict olivine grains has an exceptionally old Al-Mg age (1.92 ± 0.09 Ma after CAIs), with a value similar to ^{16}O-depleted chondrules G39 and G85 from Acfer 094 (1.79 $^{-0.16}/_{+0.19}$ Ma and 1.75 $^{-0.11}/_{+0.12}$ Ma after CAIs, respectively) (Ushikubo et al., 2013; Hertwig et al., 2019a; Fig. 11a). All of these chondrules/relict grains are ^{16}O-depleted and plot on and above the PCM line, which might be related to the NC reservoir (Williams et al., 2020), suggesting that they probably originate from a different disk region than the majority of CO, CM, CV and Acfer 094 chondrules. Therefore, the Al-Mg ages of these chondrules will be discussed separately.

Recently, Siron et al. (2021a, 2021b) determined Al-Mg ages of 31 chondrules from unequilibrated ordinary chondrites (UOCs) (L/LL3.00–3.05). The inferred UOC chondrule formation ages range from 1.7 to 2.2 Ma after CAIs (Fig. 11a). This time span of UOC chondrule formation is consistent with chondrule ages from Kita et al. (2000) and Bollard et al. (2019), but is much shorter than the duration inferred by other studies (~1 to 3 Ma; e.g., Villeneuve et al., 2009; Pape et al., 2019). One possibility for this inconsistency is the difference in measured phases: Siron et al. (2021a, 2021b) as well as Kita et al. (2000) and Bollard et al. (2019) mainly analyzed plagioclase-bearing chondrules, but Villeneuve et al. (2009) and Pape et al. (2019) exclusively analyzed glassy mesostases in chondrules instead of plagioclase. Alexander and Ebel (2012) argued for variable degrees of disturbance during parent body alteration and/or possible mixed analyses between mesostasis and high-Ca pyroxene micro-crystals to explain the range of ages from Villeneuve et al. (2009), since glassy mesostases are more susceptible to a disturbance in the Al-Mg system by parent body metamorphism. This is consistent with data from two chondrules studied by Siron et al. (2021b) that contain glassy mesostases without excess ^{26}Mg, but also have plagioclase with clear excess ^{26}Mg, which are clear evidence for the Al-Mg system of plagioclase to be more resistant to parent body alteration than that of glassy mesostases. Recently, Lewis and Jones (2019) conducted the detailed petrologic observations of chondrule mesostases from Semarkona (LL3.00 or 3.01) and found that the degree of aqueous alteration observed in chondrule mesostases is variable among chondrules within the meteorite. This observation also suggests that Al-Mg systematics of glassy mesostases in chondrules could be randomly disturbed depending on the degrees of parent body alteration, which could explain why glass-bearing chondrules tend to show large range in their Al-Mg ages. Overall, the Al-Mg system of glassy mesostasis could be modified even in chondrules from chondrites with a petrologic type of ~3.01.

Note that Siron et al. (2021a, 2021b) studied 31 chondrules with a large variety of chondrule textures, chemical compositions of mafic minerals and mesostases, making it difficult to argue for a potential bias in the selection of chondrules to explain the observed inconsistency. Therefore, the high precision Al-Mg ages of the 31 chondrules determined by Siron et al. (2021a, 2021b) are likely to be more representative range of UOC chondrule formation time.

In combination with the 31 UOC chondrule data of Siron et al. (2021a, 2021b), the high precision Al-Mg ages obtained in this study provide evidence that CO and CM chondrule formation occurred after the majority of UOC chondrules formed (Fig. 11). Considering the similarities in Mg#s, oxygen isotope ratios, and Al-Mg ages of CO, CM, CV, and Acfer 094 chondrules, chondrules from the inner Solar System are likely to be older than chondrules produced at greater heliocentric distances (Fig. 12). We also note that the majority of CR chondrules formed later than 2.8 Ma after CAIs (Fig. 11; Nagashima et al., 2014; Schrader et al., 2017; Tenner et al., 2019). Although it is possible that the distinct $\Delta^{17}O$-Mg# systematics of CR chondrules resulted only from a difference in formation timing rather than differences in both formation timing and location, we infer that chondrule formation was active outside the regions where CO, CM, CV, and Acfer 094 chondrules formed until ~4 Ma after CAIs, when the majority of CR chondrules formed. Kernel density estimates (Fig. 11b) indicate that at least three major chondrule-forming events occurred between 1 Ma and 4 Ma after CAIs, probably in different regions in the solar protoplanetary disk. We note, however, that there could have been more than three major chondrule-forming events, and that they cannot be resolved due to low analytical precision and/or poor statistics. In addition, it is quite possible that the chondrule population that we discuss here may not represent the full range of asteroid parent bodies that formed in the early Solar System. For example, the proposed temporal shift of chondrule generation from the inner to outer Solar System could be further investigated by analyzing chondrules from different sources such as ungrouped and/or newly classified chondrite groups (e.g., CY and CA; King et al., 2019; Kimura et al., 2021) with the least metamorphosed signatures as well as asteroidal samples returned by spacecraft.

The relatively ^{16}O-depleted chondrules G39 and G85 in Acfer 094 (Ushikubo et al., 2012, 2013; Hertwig et al., 2019a) and chondrule A75 containing ^{16}O-depleted relict olivine grains (this study) have older Al-Mg ages that are in agreement with those of UOC chondrules, meaning that these three chondrules (G39, G85, A75) formed almost contemporaneously with UOC chondrules (Fig. 11a). The ^{16}O-depleted characteristic of the two chondrules G39 and G85 indicates that they most likely originated in the inner Solar System and were then transported to the accretion regions of the Acfer 094 parent body (Hertwig et al., 2019a; Fig. 12). As discussed previously, the final melting event that produced chondrule A75 likely occurred in the outer Solar System, but not exactly the same as those of the majority of CC chondrules formed. We infer that chondrule A75 formed innermost area of the outer Solar System (Fig. 12) where NC-like ^{16}O-depleted solids were abundant. Such NC-like relict olivine grains are very rare in CR chondrules (Schrader et al., 2020) that might have formed in the outermost part (but not beyond ~7 AU) in the disk.

4.7. Timescales of chondrule transport and accretion into parent asteroids

The delayed formation of CC chondrules relative to the majority of UOC chondrules is consistent with the accretion ages of their corresponding parent bodies, such as 2.14 ± 0.1 Ma after CAIs for ordinary chondrite (OC) parent bodies and >2.6 Ma after CAIs for CC parent bodies (Sugiura and Fujiya, 2014). These estimated accretion ages are model dependent and may have larger unseen uncertainties, such as the size of the asteroid, choices of thermal conductivity and heat capacity functions, and water-ice fractions (e.g., Ghosh and McSween, 1999; Cohen and Coker 2000; Hevey and Sanders, 2006). Although there may be the unseen uncertainties, the accretion of the CM parent body is estimated to have occurred >3 Ma after CAIs based on both thermal modeling and Mn-Cr dating of carbonates (Fujiya et al., 2012), which are compared to the Al-Mg ages of CM chondrules that we determined in this study. Here, we use the age of achondrite NWA 6704 as an anchor, as recently proposed by Sanborn et al., (2019), Amelin et al. (2019), and Hibiya et al. (2019). The initial $^{26}Al/^{27}Al$ ratio of NWA 6704 is $(3.15 \pm 0.38) \times 10^{-7}$ (Sanborn et al., 2019), which corresponds to its formation 5.2 ± 0.1 Ma after CAIs. The relative age difference between NWA 6704 and CM carbonates can also be calculated by comparing their initial $^{53}Mn/^{55}Mn$ ratios under the assumption of a homogeneous distribution of ^{53}Mn (e.g., Sanborn et al., 2019), resulting in CM carbonates that are ~0.7 Ma older than NWA 6704 (average value of the four CM chondrites studied by Fujiya et al., 2012). By combining these two calculations, the formation age of CM carbonates are estimated to be ~4.5 Ma after CAIs, which is consistent with the reported age of $4.8\ ^{-0.4}/_{+0.5}$ Ma by Fujiya et al. (2012), even though they determined the age using a different anchor (angrite LEW 86010) (for which there is a difference in Pb-Pb ages between CAIs and angrites). Therefore, the estimated accretion age of the CM parent body (> 3 Ma after CAIs) by Fujiya et al. (2012) can be directly compared with Al-Mg ages of CM chondrules. Sugiura and Fujiya (2014) constrained the accretion age of the CM (and Tagish Lake) parent bodies to be 3.5 $^{-0.5}/_{+0.7}$ after CAIs based on the results of Fujiya et al. (2012). The accretion age does not conflict with Al-Mg ages of chondrules in A 12236, as they are all older than 3 Ma after CAIs (Table 3). The youngest CM chondrule age so far is 2.76 $^{-0.23}/_{+0.30}$ after CAIs (chondrule A28). Including the uncertainty, the formation age of A28 could be as young as 3.06 Ma after CAIs, which is not resolvable from the estimated accretion age of the CM parent body (3.5 $^{-0.5}/_{+0.7}$ Ma after CAIs), suggesting a rapid accretion of CM chondrules into the parent asteroid. If considering the uncertainty of the estimated accretion age, however, we cannot rule out a possible time gap of ~1 Ma between CM chondrule formation and their accretion into the CM parent body. If true, the CM chondrule ages could indicate that there were two or more CM parent bodies (Lee et al., 2019) and/or that the thermal model of the CM parent body (e.g., the size of the asteroid, water-ice fractions) is inaccurate.

By taking the minimum accretion time of the CM parent body of 3 Ma after CAIs, the oldest chondrule A75, which formed 1.9 Ma after CAIs, had to be stored for more than 1 Ma in the solar protoplanetary disk before accretion into the CM parent body. Alexander (2005) and Cuzzi et al. (2010) predicted that chondrules that existed within ~2–4 AU in the protoplanetary disk could be mixed within ~1 Ma. Since turbulent diffusion is a statistical process, it is possible that chondrule A75 formed in the same region where the majority of CM chondrules formed and ended up migrating to the accretion region of the CM parent body, although there is no supporting evidence for the possibility. Alternatively, since this chondrule exhibits distinct oxygen isotope systematics, the formation region of chondrule A75 is not likely the same as that of the majority of CM chondrules. Thus we infer that this chondrule traveled from its formation region to the accretion region of the CM chondrite parent body in more than 1 Ma, which does not conflict with the scenario of its formation inside the disk region relative to where the majority of CM chondrules formed (Fig. 12). According to the mixing timescale estimated by Cuzzi et al. (2010), the formation region of chondrule A75 could have been located ≥ 2 AU interior to the CM parent body accretion region (Fig. 12). The same argument could be applied for two ^{16}O-depleted, older chondrules G39 and G85 from Acfer 094. Although the accretion time of the Acfer 094 parent body is not constrained, the Al-Mg age of the youngest chondrule in Acfer 094 is determined as 2.71 $^{-0.22}/_{+0.28}$ after CAIs (Hertwig et al., 2019a), which could be considered a minimum accretion time of the Acfer 094 parent body. Since Al-Mg ages of the two ^{16}O-depleted Acfer 094 chondrules are ~1 Ma older than the youngest chondrule (Fig. 11a), their formation region could have been located ≥2 AU interior to the Acfer 094 parent body accretion region (Fig. 12). However, we cannot rule out the possibility that these ^{16}O-depleted chondrules (A75, G39, G85) formed in the region exterior to the accretion regions of the CM and Acfer 094 parent bodies and then migrated inwards in more than ~1 Ma, although the oxygen isotope similarity between these chondrules/relict grains and OC-chondrules would rather be consistent with their formation inside the disk region relative to where the CM and Acfer 094 chondrules formed.

The accretion age of the CO parent body is estimated to be 2.7 ± 0.2 Ma after CAIs based on the peak metamorphic temperature (Sugiura and Fujiya, 2014) or ~2.1–2.4 Ma after CAIs based on thermal modeling and Mn-Cr dating of secondary fayalites (Doyle et al., 2015). Doyle et al. (2015) revealed that fayalite formation on the CO parent body occurred $5.1^{-0.4}/_{+0.5}$ Ma after CAIs, which was calculated from the difference in the U-corrected Pb-Pb ages of CAIs (4567.30 ± 0.16 Ma; Connelly et al., 2012) and angrites (4563.4 ± 0.3 Ma; Amelin, 2008; Brennecka and Wadhwa, 2012) with the relative Mn-Cr age difference between angrites and fayalites in the CO chondrite MAC 88107. As for CM carbonates, if we use NWA 6704 as an age anchor, then the fayalite formation age can be calculated as ~5.2 Ma after CAIs, which is consistent with the reported value in Doyle et al. (2015). Thus, the accretion age of the CO parent body (~2.1–2.4 Ma after CAIs) based on the fayalite formation time can be directly compared with our Al-Mg ages of CO chondrules. The youngest age among the CO chondrules studied here is $2.72\ ^{-0.22}/_{+0.28}$ Ma after CAIs, which is broadly consistent with the estimated accretion time of the CO parent body by Doyle et al. (2015) (~2.1–2.4 Ma after CAIs) and is in excellent agreement with that by Sugiura and Fujiya (2014) (2.7 ± 0.2 Ma after CAIs). This suggests rapid accretion of CO chondrules into the CO parent body after their formation.

4.8. Implications for chondrule formation and evolution of the solar protoplanetary disk

Our result-driven hypothesis, that chondrule relative ages increase with heliocentric distance, provides insights on chondrule formation in the solar protoplanetary disk. Several mechanisms have been proposed for chondrule formation, including nebular shock-wave heating (e.g., Wood, 1996; Hood, 1998; Weidenschilling et al., 1998; Desch and Connolly, 2002; Ciesla and Hood, 2002; Ciesla et al., 2004; Boss and Durisen, 2005; Morris and Desch, 2010; Desch et al., 2012; Morris et al., 2012, 2016; Mann et al., 2016), electromagnetic phenomena (current sheets, lightning; e.g., Desch and Cuzzi, 2000; Joung et al., 2004; McNally et al., 2013), and impact melting during collisions between asteroids (e.g., Asphaug et al., 2011; Sanders and Scott, 2012; Johnson et al., 2015; Hasewaga et al., 2016; Wakita et al., 2017). Among them, nebular shock-wave heating best explains the survival of relict grains (e.g., Tenner et al., 2018a; Marrocchi et al., 2018a) and probable chondrule cooling rates of 100–1000 K/h while between silicate liquidus and solidus (e.g., Hewins and

Radomsky, 1990) and 1–10 K/h during sub-solidus temperatures (Schrader et al., 2018b). Although cooling rates have not been examined by numerical simulations under plausible dust/gas ratios and total pressures, nebular shock-wave heating seems currently one of the most favored chondrule formation mechanisms (Desch et al., 2012). We note that impact jetting can also explain the cooling rates of chondrules and predicts that the earliest chondrule-forming events occur closer to the Sun and that the location where chondrule formation occurs moves outwards with time (Johnson et al., 2015), which is consistent with our observations. However, this process would have resulted in extremely high dust/gas ratios (Johnson et al., 2015), which is not consistent with environments that produce abundant Mg# > 98 chondrules. In addition, the survival of relict grains in chondrules is difficult to explain in an impact jetting regime (e.g., Tenner et al., 2018a). Therefore, shock-wave heating is our preferred mechanism for the formation of the majority of chondrules.

Large-scale shock waves can be caused by gravitational instabilities (GIs) in the protoplanetary disk (Boss and Durisen, 2005; Boley and Durisen, 2008). GIs can be active in any region of cool and massive disks and excite large-scale spiral arms that result in shock waves as a natural outcome (e.g., Boss, 2002; Durisen et al., 2007). Therefore, GI-induced shock fronts are a plausible site for chondrule formation in various disk regions. The signatures of GIs and large-scale spiral arms in the protoplanetary disk have been seen in the spectroscopic observations (e.g., Pérez et al., 2016; Dong et al., 2018; Paneque-Carreño et al., 2021), suggesting that GIs are generally available as drivers for shock-wave heating in the protoplanetary disk. However, both observational and theoretical studies suggest that GI-related spiral arms are active in the very early stage of the disk evolution (class 0/I; e.g., Liu et al., 2016; Tomida et al., 2017; Meru et al., 2017), which seems inconsistent with the formation period of chondrules (class II; e.g., Kita et al., 2013). Another possible source of GIs is the formation of Jupiter. Boss and Durisen (2005) showed that GIs that were induced by Jupiter could produce a strong shock front over many Ma, which would allow for generating chondrules at ~2–4 Ma after CAIs. In addition, bow shocks around eccentric planetesimals that were excited via resonance with Jupiter (e.g., Ciesla et al., 2004; Morris et al., 2012; Mann et al., 2016) are a plausible source for large-scale shock waves. In either case, chondrule formation by shock-wave heating likely required the presence of proto-Jupiter at the time of chondrule formation; e.g., ~2 Ma after CAIs when the majority of UOC chondrules formed. This timeframe is consistent with the formation of proto-Jupiter earlier than ~1 Ma after CAIs (Kruijer et al., 2017).

The early formation and existence of proto-Jupiter has been proposed as the mechanism that established and maintained the isotopic dichotomy between the carbonaceous and non-carbonaceous meteorite groups (Budde et al., 2016a; Kruijer et al., 2017, 2020; Desch et al., 2018; Kleine et al., 2020 and references therein). If this is the case, and if the orbit of proto-Jupiter located between the carbonaceous and non-carbonaceous reservoirs, chondrule formation by gravitational instability induced by the formation of proto-Jupiter would have occurred only in the non-carbonaceous side (~2–3 AU), because any gravitational instability beyond Jupiter's orbit would drive spiral shock fronts inwards relative to Jupiter's orbit (Boss and Durisen, 2005). Also the excitations of planetesimals caused by resonance with Jupiter might have occurred only inside the orbit of Jupiter, as the efficiency of resonance outside Jupiter's orbit may have been prohibitively diminished (Nagasawa et al., 2014, 2019; Gong et al., 2019). Thus, if proto-Jupiter was located between carbonaceous and non-carbonaceous reservoirs, additional and later chondrule-forming mechanisms would be required outside the orbit of Jupiter, in order to form CC chondrules at >2.3 Ma after CAIs. Further modeling is needed to explore whether chondrules were able to form outside the orbit of Jupiter by shock-wave heating.

Alternatively, if inward and outward migration of Jupiter (i.e., Grand Tack model; Walsh et al., 2011) occurred around ~2 Ma after CAIs, it might have induced chondrule formation in the inner Solar System that later continued in the outer Solar System. It is suggested that the inward and outward migration of Jupiter occurred within ~0.6 Ma (Walsh et al., 2011), which is broadly consistent with the formation durations of chondrules in UOC, CO, CM, CV, and Acfer 094 chondrules (~1 Ma; Fig. 11a). However, a recent hydrodynamic simulation predicts that Jupiter formed at the orbit that is close to the current one (~5–6 AU) and did not migrate significantly after its formation (Tanaka et al., 2020), making it unclear if the migration of Jupiter occurred at all.

Another possibility is that proto-Jupiter was located beyond the region where CC chondrules formed, as proposed by Chaumard et al. (2021). If true, this would have allowed for both NC and CC chondrules to have been formed by shock-wave heating. As discussed by Lichtenberg et al. (2021) and van Kooten et al. (2021), high abundances of volatile elements (e.g., nitrogen) in Jupiter's atmosphere as well as the asymmetric distribution of its Trojan asteroids suggest that an initial accretion location of the proto-Jupiter could be far from the inner Solar System (> 30 AU; Öberg and Wordsworth, 2019; Bosman et al., 2019; Pirani et al., 2019), which does not support the formation of proto-Jupiter between carbonaceous and non-carbonaceous reservoirs at ~3–5 AU. On the basis of existing shock-wave heating models and chondrule O-isotopic constrains as well as timing of chondrule formation, it is conceivable that proto-Jupiter was located beyond the region where CC chondrules formed at least >2.2 Ma after CAIs. If considering the rapid accretion of CC chondrules into their parent asteroids (Budde et al., 2018; Tenner et al., 2019; this study), the above scenario is consistent with the formation of CCs inside the orbit of proto-Jupiter, which has been hypothesized based on relatively low water/rock ratios estimated for CCs (Marrocchi et al., 2018b). It is often considered that the snow line was located inside the orbit of Jupiter at least ~2–3 Ma after CAIs (Morbidelli et al., 2016; Desch et al., 2018). If correct, the above scenario would also be consistent with the self-shielding model that predicts the oxygen isotope ratios to be planetary (i.e., Earth-like) inside the snow line at the T Tauri (class II) phase (Yurimoto and Kuramoto, 2004). If considering that proto-Jupiter was located outside the CC chondrule-forming regions, and if also assuming NC and CC chondrules formed by bow shocks created by planetesimals, the difference in formation time between OC and CC chondrules would indicate that (1) large planetesimals formed earlier in the inner disk than in the outer disk and/or (2) the location of planetesimals with eccentric orbits caused by resonances involving Jupiter moved from the inner (~1–2 Ma after CAIs) to the outer (> 2.2 Ma after CAIs) Solar System. Early formation of large planetesimals in the inner disk is broadly consistent with the observed relationship between Cr and Mo isotopes of bulk meteorites and their accretion ages (Sugiura and Fujiya, 2014; Kruijer et al., 2020; Kleine et al., 2020), suggesting that accretion of asteroids in the inner Solar System started as early as CAI formation; those in the outer Solar System would postdate CAIs by ~1 Ma.

If it assumed that the proto-Jupiter formed outside the CC chondrule-forming regions, then an alternative physical barrier would be required to maintain the non-carbonaceous-carbonaceous dichotomy and to explain the high abundances of refractory inclusions in CCs (Desch et al., 2018). The presence of multiple gaps in a given disk is often observed (e.g., Isella et al., 2016), although it is not clear if these multiple gaps existed in our solar protoplanetary disk. Further dynamic modeling as well as astronomical observations are required to better understand the spatio-temporal evolution of chondrules and their relation to the evolution of the solar protoplanetary disk.

5. SUMMARY

In this study we determined the $(^{26}Al/^{27}Al)_0$ values of fifteen FeO-poor chondrules from the least metamorphosed CM and CO chondrites. We also investigated detailed mineral chemistry and petrographic features of chondrule plagioclase in order to evaluate its reliability with respect to closure of the Al-Mg system of chondrules. In addition to the $(^{26}Al/^{27}Al)_0$ values, oxygen three-isotope ratios are determined in order to discuss the spatial and temporal evolution of chondrules in the solar protoplanetary disk. We summarize the following:

1) Chondrule plagioclase in A 12236 (CM2.9) and DOM 08006 (CO3.01) exhibits chemical, nanometer-scale petrographic, and oxygen isotopic characteristics similar to those of the least metamorphosed carbonaceous chondrites such as CR2–3 and Acfer 094 (ungrouped C3.00), suggesting that their Al-Mg systematics are undisturbed. Chondrule plagioclase in Y-81020 (CO3.05) exhibits oxygen isotope disequilibrium with coexisting olivine and pyroxene, indicative of oxygen isotope exchange between plagioclase and ^{16}O-poor fluids on the CO parent body. However, their Al-Mg systematics likely remained undisturbed.
2) Mg#-$\Delta^{17}O$ systematics of chondrules possess distinct trends for each chondrite group. By considering the fundamental non-carbonaceous-carbonaceous dichotomy as well as distinct isotopic characteristics of CR chondrules, we infer that there were distinct chondrule-forming environments for (*i*) non-carbonaceous, (*ii*) CV, CO, CM, and Acfer 094, and (*iii*) CR chondrite chondrules, which are interpreted as having been

located in the inner, outer, and outermost (but not beyond ~7 AU; Sutton et al., 2017) parts, respectively, of the solar protoplanetary disk.

3) High precision Al-Mg analyses reveal a short-duration for CO chondrule formation (~2.2–2.7 Ma after CAIs), which is in contradiction with earlier observations by Kurahashi et al. (2008).
4) Al-Mg ages of CM chondrules were determined for the first time. Aside from chondrule A75 which has distinct oxygen isotope characteristics, their formation duration is similar to those for CO chondrules (~2.4–2.8 Ma after CAIs).
5) The Al-Mg ages of CO and CM chondrules studied here are systematically younger than those of UOC chondrules determined by Siron et al. (2021a, 2021b). In combination with Al-Mg ages for CV and CR chondrules (Nagashima et al., 2014, 2017; Schrader et al., 2017; Tenner et al., 2019), we infer a temporal shift of chondrule generation from the inner to the outer part of the protoplanetary disk. The systematic difference in Al-Mg ages between NC and CC chondrules is consistent with the estimated accretion times of NC and CC parent bodies (e.g., Fujiya et al., 2012; Doyle et al., 2015).
6) Among the dated chondrules from the least metamorphosed carbonaceous chondrites, there are three chondrules (one from A 12236 and two from Acfer 094; Ushikubo et al., 2013; Hertwig et al., 2019a; this study) with exceptionally older Al-Mg ages (~1.7–1.9 Ma after CAIs). Three chondrules exhibit relatively ^{16}O-depleted characteristics compared to the majority of CC chondrules and/or contain ^{16}O-depleted relict grains, suggesting they formed in a different environment, probably inside the disk region relative to where the majority of CC chondrules formed. We hypothesize the three chondrules subsequently migrated outward and then accreted into the CM and Acfer 094 parent bodies, although their formation exterior to where

the majority of CC chondrules formed and subsequent inward migration cannot be ruled out completely.

7) In the currently known shock-wave heating models, the majority of CC chondrule formation would require the formation of proto-Jupiter outside the CC chondrule-forming regions. In this case, an alternative to the Jupiter gap would be required to explain the fundamental non-carbonaceous-carbonaceous dichotomy. Alternatively, additional chondrule-forming mechanisms would be required outside the orbit of proto-Jupiter. Further dynamic modeling, as well as astronomical observations, are needed to explore how CC chondrules formed in the outer Solar System.

Acknowledgment

We gratefully acknowledge the National Institute of Polar Research and ANSMET Program for allocating samples for this study. We thank Sota Arakawa for fruitful discussions, Mingming Zhang and Michael Spicuzza for technical assistance during SIMS operations, John Fournelle for assistance with EPMA analyses, and Bil Schneider for help with SEM observations. We thank Yuri Amelin for editorial handling and constructive comments, Conel Alexander, Devin Schrader, and an anonymous reviewer for their constructive reviews, which significantly improved the quality of this paper. This work is supported by NASA Emerging World Programs (NNX17AE29G and 80NSSC21K0378, N.K.; NNH17AE61i, T.J.T.). The upgrade of the RF plasma source is supported by the NASA Laboratory Analysis of Returned Samples and Planetary Major Equipment Programs (NNX16AG80G) and the

NSF Instrumentation and Facility Program (EAR-1355590). WiscSIMS is partly supported by NSF (EAR-1658823).

References

Akaki T., Nakamura T., Noguchi T. and Tsuchiyama A. (2007) Multiple formation of chondrules in the early Solar System: Chronology of a compound Al-rich chondrule. *Astrophys. J.* **656**, L29–L32.

Alexander C. M. O'D. (2005) From supernovae to planets: The view from meteorites and interplanetary dust particles. In *Chondrites and the protoplanetary disk* (eds. A. N. Krot, E. R. D. Scott, and B. Reipurth). pp. 972–1002.

Alexander C. M. O'D. and Ebel D. S. (2012) Questions, questions: Can the contradictions between the petrologic, isotopic, thermodynamic, and astrophysical constraints on chondrule formation be resolved? *Meteorit. Planet. Sci.* **47**, 1157–1175.

Alexander C. M. O'D., Grossman J. N., Ebel D. S. and Ciesla F. J. (2008) The formation conditions of chondrules and chondrites. *Science.* **320**, 1617–1619.

Amelin Y. (2008) The U-Pb systematics of angrite Sahara 99555. *Geochim. Cosmochim. Acta* **72**, 4874–4885.

Amelin Y. and Krot A. N. (2007) Pb isotopic age of the Allende chondrules. *Meteorit. Planet.* **42**, 1321–1335.

Amelin Y., Krot A. N., Hutcheon I. D. and Ulyanov A. A. (2002) Lead siotopic ages of chondrules and calcium-aluminium-rich inclusions. *Science.* **297**, 1678–1683.

Amelin Y., Kaltenbach A., Iizuka T., Stirling C. H., Ireland T. R., Petaev M. and Jacobsen S. B. (2010) U-Pb chronology of the Solar System's oldest solids with variable $^{238}U/^{235}U$.

Earth Planet. Sci. Lett. **300**, 343–350.

Amelin Y., Koefoed P., Iizuka T., Fernandes V. A., Huyskens M. H., Yin Q. Z. and Irving A. J. (2019) U-Pb, Rb-Sr and Ar-Ar systematics of the ungrouped achondrites Northwest Africa 6704 and Northwest Africa 6693. *Geochim. Cosmochim. Acta* **245**, 628–642.

Asphaug E., Jutzi M. and Movshovitz N. (2011) Chondrule formation during planetesimal accretion. *Earth Planet. Sci. Lett.* **308**, 369–379.

Baertschi P. (1976) Absolute ^{18}O content of standard mean ocean water. *Earth Planet. Sci. Lett.* **31**, 341–344.

Barosch J., Hezel D. C., Ebel D. S. and Friend P. (2019) Mineralogically zoned chondrules in ordinary chondrites as evidence for open system chondrule behaviour. *Geochim. Cosmochim. Acta* **249**, 1–16.

Beaty D. W. and Albee A. L. (1980) Silica solid solution and zoning in natural plagioclase. *Am. Mineral.* **65**, 63–74.

Bischoff A. and Keil K. (1984) Al-rich objects in ordinary chondrites: Related origin of carbonaceous and ordinary chondrites and their constituents. *Geochim. Cosmochim. Acta* **48**, 693–709.

Blackburn T., Alexander C. M. O'D., Carlson R. and Elkins-Tanton L. T. (2017) The accretion and impact history of the ordinary chondrite parent bodies. *Geochim. Cosmochim. Acta* **200**, 201–217.

Blichert-Toft J., Göpel C., Chaussidon M. and Albarède F. (2020) Th/U variability in Allende chondrules. *Geochim. Cosmochim. Acta* **280**, 378–394.

Boley A. C. and Durisen R. H. (2008) Gravitational Instabilities, Chondrule Formation, and the FU Orionis Phenomenon. *Astrophys. J.* **685**, 1193–1209.

Bollard J., Connelly J. N., Whitehouse M. J., Pringle E. A., Bonal L., Jørgensen J. K., Nordlund Å., Moynier F. and Bizzarro M. (2017) Early formation of planetary building blocks inferred from Pb isotopic ages of chondrules. *Sci. Adv.* **3**, 1–10.

Bollard J., Kawasaki N., Sakamoto N., Olsen M., Itoh S., Larsen K. K., Wielandt D., Schiller M., Connelly J. N., Yurimoto H. and Bizzarro M. (2019) Combined U-corrected Pb-Pb dating and ^{26}Al-^{26}Mg systematics of individual chondrules – Evidence for a reduced initial abundance of ^{26}Al amongst inner Solar System chondrules. *Geochim. Cosmochim. Acta* **260**, 62–83.

Bosman A. D., Cridland A. J. and Miguel Y. (2019) Jupiter formed as a pebble pile around the N_2 ice line. *Astron. Astrophys.* **632**, L11.

Boss A. P. (2002) Evolution of the Solar Nebula. V. Disk Instabilities with Varied Thermodynamics. *Astrophys. J.* **576**, 462–472.

Boss A. P. and Durisen R. H. (2005) Chondrule-forming shock fronts in the solar nebula: A possible unified scenario for planet and chondrite formation. *Astrophys. J.* **621**, L137–L140.

Bouden N., Villeneuve J., Marrocchi Y., Deloule E., Füri E., Gurenko A., Piani L., Thomassot E., Peres P. and Fernandes F. (2021) Triple oxygen isotope measurements by multi-collector secondary ion mass spectrometry. *Front. Earth Sci.* **8**, 601169.

Bouvier A. and Wadhwa M. (2010) The age of the Solar System redefined by the oldest Pb-Pb age of a meteoritic inclusion. *Nat. Geosci.* **3**, 637–641.

Bouvier A., Brennecka G. A. and Wadhwa M. (2011) Absolute chronology of the first solids in the Solar System. *Formation of the First Solids in the Solar System,* #9054.

Brasser R. and Mojzsis S. J. (2020) The partitioning of the inner and outer Solar System by a structured protoplanetary disk. *Nat. Astron.* **4**, 492–499.

Brennecka G. A. and Wadhwa M. (2012) Uranium isotope compositions of the basaltic angrite meteorites and the chronological implications for the early Solar System. *Proc.*

Natl. Acad. Sci.* **109**, 9299–9303.

Brooks C., Hart S. R. and Wendt I. (1972) Realistic use of two-error regression treatments as applied to rubidium-strontium data. *Rev. Geophys. Sp. Phys.* **10**, 551–577.

Budde G., Burkhardt C., Brennecka G. A., Fischer-Gödde M., Kruijer T. S. and Kleine T. (2016a) Molybdenum isotopic evidence for the origin of chondrules and a distinct genetic heritage of carbonaceous and non-carbonaceous meteorites. *Earth Planet. Sci. Lett.* **454**, 293–303.

Budde G., Kleine T., Kruijer T. S., Burkhardt C. and Metzler K. (2016b) Tungsten isotopic constraints on the age and origin of chondrules. *Proc. Natl. Acad. Sci.* **113**, 2886–2891.

Budde G., Kruijer T. S. and Kleine T. (2018) Hf-W chronology of CR chondrites: Implications for the timescales of chondrule formation and the distribution of ^{26}Al in the solar nebula. *Geochim. Cosmochim. Acta* **222**, 284–304.

Catanzaro E. J., Murphy T. J., Garner E. L. and Shields W. R. (1966) Absolute isotopic abundance ratios and atomic weight of magnesium. *J. Res. Natl. Bur. Stand. Sect. A Phys. Chem.* **70A**, 453–458.

Chaumard N., Defouilloy C. and Kita N. T. (2018) Oxygen isotope systematics of chondrules in the Murchison CM2 chondrite and implications for the CO-CM relationship. *Geochim. Cosmochim. Acta* **228**, 220–242.

Chaumard N., Defouilloy C., Hertwig A. T. and Kita N. T. (2021) Oxygen isotope systematics of chondrules in the Paris CM2 chondrite: Indication for a single large formation region across snow line. *Geochim. Cosmochim. Acta* **299**, 199–218.

Chaussidon M., Libourel G. and Krot A. N. (2008) Oxygen isotopic constraints on the origin of magnesian chondrules and on the gaseous reservoirs in the early Solar System. *Geochim. Cosmochim. Acta* **72**, 1924–1938.

Ciesla F. J. and Hood L. L. (2002) The nebular shock wave model for chondrule formation:

Shock processing in a particle-gas suspension. *Icarus* **158**, 281–293.

Ciesla F. J., Hood L. L. and Weidenschilling S. J. (2004) Evaluating planetesimal bow shocks as sites for chondrule formation. *Meteorit. Planet. Sci.* **39**, 1809–1821.

Clayton R. N. and Mayeda T. K. (1984) The oxygen isotope record in Murchison and other carbonaceous chondrites. *Earth Planet. Sci. Lett.* **67**, 151–161.

Clayton R. N. and Mayeda T. K. (1999) Oxygen isotope studies of carbonaceous chondrites. *Geochim. Cosmochim. Acta* **63**, 2089–2104.

Clayton R. N., Onuma N., Grossman L. and Mayeda T. K. (1977) Distribution of the pre-solar component in Allende and other carbonaceous chondrites. *Earth Planet. Sci. Lett.* **34**, 209–224.

Clayton R. N., Mayeda T. K., Goswami J. N. and Olsen E. J. (1991) Oxygen isotope studies of ordinary chondrites. *Geochim. Cosmochim. Acta* **55**, 2317–2337.

Cohen B. A. and Coker R. F. (2000) Modeling of Liquid Water on CM Meteorite Parent Bodies and Implications for Amino Acid Racemization. *Icarus* **145**, 369–381.

Connelly J. N. and Bizzarro M. (2009) Pb-Pb dating of chondrules from CV chondrites by progressive dissolution. *Chem. Geol.* **259**, 143–151.

Connelly J. N., Amelin Y., Krot A. N. and Bizzarro M. (2008) Chronology of the Solar System's oldest solids. *Astrophys. J.* **675**, L121–L124.

Connelly J. N., Bizzarro M., Krot A. N., Nordlund Å., Wielandt D. and Ivanova M. A. (2012) The absolute chronology and thermal processing of solids in the solar protoplanetary disk. *Science.* **338**, 651–655.

Connolly H. C. J. and Huss G. R. (2010) Compositional evolution of the protoplanetary disk: Oxygen isotopes of type-II chondrules from CR2 chondrites. *Geochim. Cosmochim. Acta* **74**, 2473–2483.

Connolly H. C. J. and Jones R. H. (2016) Chondrules: The canonical and noncanonical views.

J. Geophys. Res. Planets **121**, 1885–1899.

Cuzzi J. N., Hogan R. C. and Bottke W. F. (2010) Towards initial mass functions for asteroids and Kuiper Belt Objects. *Icarus* **208**, 518–538.

Davidson J., Alexander C. M. O'D., Stroud R. M., Busemann H. and Nittler L. R. (2019a) Mineralogy and petrology of Dominion Range 08006: A very primitive CO3 carbonaceous chondrite. *Geochim. Cosmochim. Acta* **265**, 259–278.

Davidson J., Schrader D. L., Alexander C. M. O'D., Nittler L. R. and Bowden R. (2019b) Re-examining thermal metamorphism of the Renazzo-like (CR) carbonaceous chondrites: Insights from pristine Miller Range 090657 and shock-heated Graves Nunataks 06100. *Geochim. Cosmochim. Acta* **267**, 240–256.

Davis A. M., Richter F. M., Mendybaev R. A., Janney P. E., Wadhwa M. and McKeegan K. D. (2015) Isotopic mass fractionation laws for magnesium and their effects on ^{26}Al–^{26}Mg systematics in solar system materials. *Geochim. Cosmochim. Acta* **158**, 245–261.

Defouilloy C., Nakashima D., Joswiak D. J., Brownlee D. E., Tenner T. J. and Kita N. T. (2017) Origin of crystalline silicates from Comet 81P/Wild 2: Combined study on their oxygen isotopes and mineral chemistry. *Earth Planet. Sci. Lett.* **465**, 145–154.

Desch S. J. and Connolly H. C. J. (2002) A model of the thermal processing of particles in solar nebula shocks: Application to the cooling rates of chondrules. *Meteorit. Planet. Sci.* **37**, 183–207.

Desch S. J. and Cuzzi J. N. (2000) The generation of lightning in the solar nebula. *Icarus* **143**, 87–105.

Desch S. J., Morris M. A., Connolly H. C. J. and Boss A. P. (2012) The importance of experiments: Constraints on chondrule formation models. *Meteorit. Planet. Sci.* **47**, 1139–1156.

Desch S. J., Kalyaan A. and Alexander C. M. O'D. (2018) The effect of Jupiter's formation on the distribution of refractory elements and inclusions in meteorites. *Astrophys. J. Suppl. Ser.* **238**, 11 (31pp).

Dong R., Najita J. R. and Brittain S. (2018) Spiral Arms in Disks: Planets or Gravitational Instability? *Astrophys. J.* **862**, 103 (19pp).

Doyle P. M., Jogo K., Nagashima K., Krot A. N., Wakita S., Ciesla F. J. and Hutcheon I. D. (2015) Early aqueous activity on the ordinary and carbonaceous chondrite parent bodies recorded by fayalite. *Nat. Commun.* **6**, 7444.

Durisen R., Boss A. P., Mayer L., Nelson A., Quinn T. and Rice K. (2007) Gravitational Instabilities in Gaseous Protoplanetary Disks and Implications for Giant Planet Formation. In *Protostars and Planets V* (eds. B. Reipurth, D. Jewitt, and K. Keil). pp. 607–622.

Ebel D. S. and Grossman L. (2000) Condensation in dust-enriched systems. **64**, 339–366.

Edwards G. H. and Blackburn T. (2020) Accretion of a large LL parent planetesimal from a recently formed chondrule population. *Sci. Adv.* **6**, eaay8641.

Fujiya W., Sugiura N., Hotta H., Ichimura K. and Sano Y. (2012) Evidence for the late formation of hydrous asteroids from young meteoritic carbonates. *Nat. Commun.* **3,** 627.

Fujiya W., Sugiura N., Sano Y. and Hiyagon H. (2013) Mn-Cr ages of dolomites in CI chondrites and the Tagish Lake ungrouped carbonaceous chondrite. *Earth Planet. Sci. Lett.* **362**, 130–142.

Fukuda K., Beard B. L., Dunlap D. R., Spicuzza M. J., Fournelle J. H., Wadhwa M. and Kita N. T. (2020) Magnesium isotope analysis of olivine and pyroxene by SIMS: Evaluation of matrix effects. *Chem. Geol.* **540**, 119482.

Fukuda K., Brownlee D. E., Joswiak D. J., Tenner T. J., Kimura M. and Kita N. T. (2021a) Correlated isotopic and chemical evidence for condensation origins of olivine in comet 81P/Wild 2 and in AOAs from CV and CO chondrites. *Geochim. Cosmochim. Acta* **293**, 544–574.

Fukuda K., Hiyagon H., Fujiya W., Kagoshima T., Itano K., Iizuka T., Kita N. T. and Sano Y. (2021b) Irradiation origin of ^{10}Be in the solar nebula: Evidence from Li-Be-B and Al-Mg isotope systematics, and REE abundances of CAIs from Yamato-81020 CO3.05 chondrite. *Geochim. Cosmochim. Acta* **293**, 187–204.

Galy A., Yoffe O., Janney P. E., Williams R. W., Cloquet C., Alard O., Halicz L., Wadhwa M., Hutcheon I. D., Ramon E. and Carignan J. (2003) Magnesium isotope heterogeneity of the isotopic standard SRM980 and new reference materials for magnesium-isotope-ratio measurements. *J. Anal. At. Spectrom.* **18**, 1352.

Gerber S., Burkhardt C., Budde G., Metzler K. and Kleine T. (2017) Mixing and transport of dust in the early solar nebula as inferred from titanium isotope variations among chondrules. *Astrophys. J.* **841**, L17 (7pp).

Ghosh A. and McSween H. Y. (1999) Temperature dependence of specific heat capacity and its effect on asteroid thermal models. *Meteorit. Planet. Sci.* **34**, 121–127.

Glavin D. P., McLain H. L., Dworkin J. P., Parker E. T., Elsila J. E., Aponte J. C., Simkus D. N., Pozarycki C. I., Graham H. V., Nittler L. R. and Alexander C. M. O'D. (2020) Abundant extraterrestrial amino acids in the primitive CM carbonaceous chondrite Asuka 12236. *Meteorit. Planet. Sci.* **55**, 1979–2006.

Gong M., Zheng X., Lin D. N. C., Silsbee K., Baruteau C. and Mao S. (2019) Chondrule Formation by the Jovian Sweeping Secular Resonance. *Astrophys. J.* **883**, 164 (12pp).

Gregory T., Luu T.-H., Coath C. D., Russell S. S. and Elliott T. (2020) Primordial formation of major silicates in a protoplanetary disc with homogeneous ^{26}Al/^{27}Al. *Sci. Adv.* **6**, eaay9626.

Grimm R. E. and McSween Jr. H. Y. M. (1993) Heliocentric zoning of the asteroid belt by aluminum-26 heating. *Science.* **259**, 653–655.

Harsono D., Bjerkeli P., van der Wiel M. H. D., Ramsey J. P., Maud L. T., Kristensen L. E. and Jørgensen J. K. (2018) Evidence for the start of planet formation in a young circumstellar disk. *Nat. Astron.* **2**, 646–651.

Hasegawa Y., Wakita S., Matsumoto Y. and Oshino S. (2016) Chondrule Formation Via Impact Jetting Triggered By Planetary Accretion. *Astrophys. J.* **816**, 8 (14pp).

Heck P. R., Ushikubo T., Schmitz B., Kita N. T., Spicuzza M. J. and Valley J. W. (2010) A single asteroidal source for extraterrestrial Ordovician chromite grains from Sweden and China: High-precision oxygen three-isotope SIMS analysis. *Geochim. Cosmochim. Acta* **74**, 497–509.

Hertwig A. T., Defouilloy C. and Kita N. T. (2018) Formation of chondrules in a moderately high dust enriched disk: Evidence from oxygen isotopes of chondrules from the Kaba CV3 chondrite. *Geochim. Cosmochim. Acta* **224**, 116–131.

Hertwig A. T., Kimura M., Ushikubo T., Defouilloy C. and Kita N. T. (2019a) The ^{26}Al-^{26}Mg systematics of FeO-rich chondrules from Acfer 094: Two chondrule generations distinct in age and oxygen isotope ratios. *Geochim. Cosmochim. Acta* **253**, 111–126.

Hertwig A. T., Kimura M., Defouilloy C. and Kita N. T. (2019b) Oxygen isotope systematics of chondrule olivine, pyroxene, and plagioclase in one of the most pristine CV3$_{Red}$ chondrites (Northwest Africa 8613). *Meteorit. Planet. Sci.* **54**, 2666–2685.

Hevey P. J. and Sanders I. S. (2006) A model for planetesimal meltdown by ^{26}Al and its implications for meteorite parent bodies. *Meteorit. Planet. Sci.* **41**, 95–106.

Hewins R. H. and Radomsky P. M. (1990) Temperature conditions for chondrule formation. *Meteoritics* **25**, 309–318.

Hezel D. C. and Palme H. (2010) The chemical relationship between chondrules and matrix and the chondrule matrix complementarity. *Earth Planet. Sci. Lett.* **294**, 85–93.

Hezel D. C., Balnd P. A., Palme H., Jacquet E. and Bigolski J. (2018) Composition of chondrules and matrix and their complementary relationship in chondrites. In *Chondrules: Records of Protoplanetary Disk Processes* (eds. S. S. Russell, H. C. Connolly, and A. N. Krot). Cambridge University Press. pp. 91–121.

Hibiya Y., Archer G. J., Tanaka R., Sanborn M. E., Sato Y., Iizuka T., Ozawa K., Walker R. J., Yamaguchi A., Yin Q. Z., Nakamura T. and Irving A. J. (2019) The origin of the unique achondrite Northwest Africa 6704: Constraints from petrology, chemistry and Re–Os, O and Ti isotope systematics. *Geochim. Cosmochim. Acta* **245**, 597–627.

Hood L. L. (1998) Thermal processing of chondrule precursors in planetesimal bow shocks. *Meteorit. Planet. Sci.* **33**, 97–107.

Hutcheon I. D. and Hutchison R. (1989) Evidence from the Semarkona ordinary chondrite for ^{26}Al heating of small planets. *Nature* **337**, 238–241.

Isella A., Guidi G., Testi L., Liu S., Li H., Li S., Weaver E., Boehler Y., Carperter J. M., De Gregorio-Monsalvo I., Manara C. F., Natta A., Pérez L. M., Ricci L., Sargent A., Tazzari M. and Turner N. (2016) Ringed structures of the HD 163296 protoplanetary disk revealed by ALMA. *Phys. Rev. Lett.* **117**, 251101.

Jacobsen B., Yin Q.-Z., Moynier F., Amelin Y., Krot A. N., Nagashima K., Hutcheon I. D. and Palme H. (2008) ^{26}Al-^{26}Mg and ^{207}Pb-^{206}Pb systematics of Allende CAIs: Canonical solar initial ^{26}Al/^{27}Al ratio reinstated. *Earth Planet. Sci. Lett.* **272**, 353–364.

Jogo K., Nakamura T., Ito M., Wakita S., Zolotov M. Y. and Messenger S. R. (2017) Mn–Cr ages and formation conditions of fayalite in CV3 carbonaceous chondrites: Constraints on the accretion ages of chondritic asteroids. *Geochim. Cosmochim. Acta* **199**, 58–74.

Johnson B. C., Minton D. A., Melosh H. J. and Zuber M. T. (2015) Impact jetting as the origin of chondrules. *Nature* **517**, 339–341.

Jones R. H. (1994) Petrology of FeO-poor, porphyritic pyroxene chondrules in the

Semarkona chondrite. *Geochim. Cosmochim. Acta* **58**, 5325–5340.

Jones R. H. (2012) Petrographic constraints on the diversity of chondrule reservoirs in the protoplanetary disk. *Meteorit. Planet. Sci.* **47**, 1176–1190.

Joung M. K. R., Mac Low M. and Ebel D. S. (2004) Chondrule formation and protoplanetary disk heating by current sheets in nonideal magnetohydrodynamic turbulence. *Astrophys. J.* **606**, 532–541.

Kawasaki N., Wada S., Park C., Sakamoto N. and Yurimoto H. (2020) Variations in initial $^{26}Al/^{27}Al$ ratios among fine-grained Ca-Al-rich inclusions from reduced CV chondrites. *Geochim. Cosmochim. Acta* **279**, 1–15.

Kimura M., Grossman J. N. and Weisberg M. K. (2008) Fe-Ni metal in primitive chondrites: Indicators of classification and metamorphic conditions for ordinary and CO chondrites. *Meteorit. Planet. Sci.* **43**, 1161–1177.

Kimura M., Imae N., Komatsu M., Barrat J. A., Greenwood R. C., Yamaguchi A. and Noguchi T. (2020) The most primitive CM chondrites, Asuka 12085, 12169, and 12236, of subtypes 3.0–2.8: Their characteristic features and classification. *Polar Sci.* **26**, 100565.

Kimura M., Greenwood R. C., Komatsu M., Imae N., Yamaguchi A. and Sato R. Petrology and classification of A-9003, A 09535, and Y-82094: A new type of carbonaceous chondrite. *Meteorit. Planet. Sci., in press.* DOI: 10.1111/maps.13704

King A. J., Bates H. C., Krietsch D., Busemann H., Clay P. L., Schofield P. F. and Russell S. S. (2019) The Yamato-type (CY) carbonaceous chondrite group: Analogues for the surface of asteroid Ryugu? *Geochemistry* **79**, 125531.

Kita N. T., Nagahara H., Togashi S. and Morishita Y. (2000) A short duration of chondrule formation in the solar nebula: Evidence from ^{26}Al in Semarkona ferromagnesian chondrules. *Geochim. Cosmochim. Acta* **64**, 3913–3922.

Kita N. T., Nagahara H., Tachibana S., Tomomura S., Spicuzza M. J., Fournelle J. H. and Valley J. W. (2010) High precision SIMS oxygen three isotope study of chondrules in LL3 chondrites: Role of ambient gas during chondrule formation. *Geochim. Cosmochim. Acta* **74**, 6610–6635.

Kita N. T., Ushikubo T., Knight K. B., Mendybaev R. A., Davis A. M., Richter F. M. and Fournelle J. H. (2012) Internal ^{26}Al-^{26}Mg isotope systematics of a Type B CAI: Remelting of refractory precursor solids. *Geochim. Cosmochim. Acta* **86**, 37–51.

Kita N. T., Yin Q.-Z., Macpherson G. J., Ushikubo T., Jacobsen B., Nagashima K., Kurahashi E., Krot A. N. and Jacobsen S. B. (2013) ^{26}Al-^{26}Mg isotope systematics of the first solids in the early solar system. *Meteorit. Planet. Sci.* **48**, 1383–1400.

Kleine T., Budde G., Burkhardt C., Kruijer T. S., Worsham E. A., Morbidelli A. and Nimmo F. (2020) The non-carbonaceous–carbonaceous meteorite dichotomy. *Space Sci. Rev.* **216,** 55.

Komatsu M., Fagan T. J., Mikouchi T. and Yamaguchi A. (2014) Alteration sequence of CV3 chondrites : matrix textures and Raman spectroscopy. *5th Symp. Polar Science* National Inst. Polar Res. abstract #370.

Krot A. N. and Nagashima K. (2016) Evidence for oxygen-isotope exchange in chondrules and refractory inclusions during fluid-rock interaction on the CV chondrite parent body. *79th Annual Meeting of the Meteoritical Society*. abstract #6014.

Krot A. N., Nagashima K., Fintor K. and Pál-Molnár E. (2019) Evidence for oxygen-isotope exchange in refractory inclusions from Kaba (CV3.1) carbonaceous chondrite during fluid-rock interaction on the CV parent asteroid. *Geochim. Cosmochim. Acta* **246**, 419–435.

Kruijer T. S., Kleine T., Fischer-Gödde M., Burkhardt C. and Wieler R. (2014) Nucleosynthetic W isotope anomalies and the Hf-W chronometry of Ca-Al-rich inclusions. *Earth Planet. Sci. Lett.* **403**, 317–327.

Kruijer T. S., Burkhardt C., Budde G. and Kleine T. (2017) Age of Jupiter inferred from the distinct genetics and formation times of meteorites. *Proc. Natl. Acad. Sci. U. S. A.* **114**, 6712–6716.

Kruijer T. S., Kleine T. and Borg L. E. (2020) The great isotopic dichotomy of the early Solar System. *Nat. Astron.* **4**, 32–40.

Kunihiro T., Rubin A. E., McKeegan K. D. and Wasson J. T. (2004) Initial $^{26}Al/^{27}Al$ in carbonaceous-chondrite chondrules: Too little ^{26}Al to melt asteroids. *Geochim. Cosmochim. Acta* **68**, 2947–2957.

Kurahashi E., Kita N. T., Nagahara H. and Morishita Y. (2008) ^{26}Al-^{26}Mg systematics of chondrules in a primitive CO chondrite. *Geochim. Cosmochim. Acta* **72**, 3865–3882.

Larsen K. K., Trinquier A., Paton C., Schiller M., Wielandt D., Ivanova M. A., Connelly J. N., Nordlund Å., Krot A. N. and Bizzarro M. (2011) Evidence for magnesium isotope heterogeneity in the solar protoplanetary disk. *Astrophys. J. Lett.* **735**, L37 (7pp).

LaTourrette T. and Wasserburg G. J. (1998) Mg diffusion in anorthite: implications for the formation of early solar system planetesimals. *Earth Planet. Sci. Lett.* **158**, 91–108.

Lee M. R., Cohen B. E., King A. J. and Greenwood R. C. (2019) The diversity of CM carbonaceous chondrite parent bodies explored using Lewis Cliff 85311. *Geochim. Cosmochim. Acta* **264**, 224–244.

Lewis J. A. and Jones R. H. (2019) Primary feldspar in the Semarkona LL3.00 chondrite: Constraints on chondrule formation and secondary alteration. *Meteorit. Planet. Sci.* **54**, 72–89.

Libourel G., Krot A. N. and Tissandier L. (2006) Role of gas-melt interaction during chondrule formation. *Earth Planet. Sci. Lett.* **251**, 232–240.

Lichtenberg T., Golabek G. J., Gerya T. V. and Meyer M. R. (2016) The effects of short-lived radionuclides and porosity on the early thermo-mechanical evolution of planetesimals. *Icarus* **274**, 350–365.

Lichtenberg T., Golabek G. J., Dullemond C. P., Schönbächler M., Gerya T. V. and Meyer M. R. (2018) Impact splash chondrule formation during planetesimal recycling. *Icarus* **302**, 27–43.

Lichtenberg T., Drążkowska J., Schönbächler M., Golabek G. J. and Hands T. O. (2021) Bifurcation of planetary building blocks during Solar System formation. *Science.* **371**, 365–370.

Liu H. B., Takami M., Kudo T., Hashimoto J., Dong R., Vorobyov E. I., Pyo T.-S., Fukagawa M., Tamura M., Henning T., Dunham M. M., Karr J. L., Kusakabe N. and Tsuribe T. (2016) Circumstellar disks of the most vigorously accreting young stars. *Sci. Adv.* **2**, e1500875.

Longhi J. and Hays J. F. (1979) Phase equilibria and solid solution along the join $CaAl_2Si_2O_8$-SiO_2. *Am. J. Sci.* **279**, 876–890.

Ludwig K. R. (2012) User's Manual for Isoplot 3.75. *Berkley Geochronol. Center, Spec. Publ.*, 1–75.

Luu T.-H., Hin R. C., Coath C. D. and Elliott T. (2019) Bulk chondrite variability in mass independent magnesium isotope compositions – Implications for initial solar system $^{26}Al/^{27}Al$ and the timing of terrestrial accretion. *Earth Planet. Sci. Lett.* **522**, 166–175.

Mann C. R., Boley A. C. and Morris M. A. (2016) Planetary Embryo Bow Shocks As a Mechanism for Chondrule Formation. *Astrophys. J.* **818**, 103 (20pp).

Marrocchi Y., Villeneuve J., Batanova V., Piani L. and Jacquet E. (2018a) Oxygen isotopic diversity of chondrule precursors and the nebular origin of chondrules. *Earth Planet. Sci. Lett.* **496**, 132–141.

Marrocchi Y., Bekaert D. V. and Piani L. (2018b) Origin and abundance of water in carbonaceous asteroids. *Earth Planet. Sci. Lett.* **482**, 23–32.

Marrocchi Y., Euverte R., Villeneuve J., Batanova V., Welsch B., Ferrière L. and Jacquet E. (2019) Formation of CV chondrules by recycling of amoeboid olivine aggregate-like precursors. *Geochim. Cosmochim. Acta* 247, 121–141.

Maruyama S. and Yurimoto H. (2003) Relationship among O, Mg isotopes and the petrography of two spinel-bearing compound chondrules. *Geochim. Cosmochim. Acta* **67**, 3943–3957.

Maruyama S., Yurimoto H. and Sueno S. (1999) Oxygen isotope evidence regarding the formation of spinel-bearing chondrules. *Earth Planet. Sci. Lett.* **169**, 165–171.

Matsuhisa Y. (1979) Oxygen isotopic compositions of volcanic rocks from the east Japan island arcs and their bearing on petrogenesis. **5**, 271–296.

McNally C. P., Hubbard A., Mac Low M.-M., Ebel D. S. and D'Alessio P. (2013) Mineral processing by short circuits in protoplanetary disks. *Astrophys. J.* **767**, L2 (6pp).

Meru F., Juhász A., Ilee J. D., Clarke C. J., Rosotti G. P. and Booth R. A. (2017) On the Origin of the Spiral Morphology in the Elias 2–27 Circumstellar Disk. *Astrophys. J.* **839**, L24 (6pp).

Miller K. E., Lauretta D. S., Connolly H. C., Berger E. L., Nagashima K. and Domanik K. (2017) Formation of unequilibrated R chondrite chondrules and opaque phases. *Geochim. Cosmochim. Acta* **209**, 24–50.

Mishra R. K. and Chaussidon M. (2014) Timing and extent of Mg and Al isotopic homogenization in the early inner Solar System. *Earth Planet. Sci. Lett.* **390**, 318–326.

Mishra R. K., Goswami J. N., Tachibana S., Huss G. R. and Rudraswami N. G. (2010) ^{60}Fe and ^{26}Al in chondrules from unequilibrated chondrites: Implications for early solar system processes. *Astrophys. J. Lett.* **714**, L217–L221.

Morbidelli A., Bitsch B., Crida A., Gounelle M., Guillot T., Jacobson S., Johansen A., Lambrechts M. and Lega E. (2016) Fossilized condensation lines in the Solar System protoplanetary disk. *Icarus* **267**, 368–376.

Morris M. A. and Desch S. J. (2010) Thermal histories of chondrules in solar nebula shocks. *Astrophys. J.* **722**, 1474–1494.

Morris M. A., Boley A. C., Desch S. J. and Athanassiadou T. (2012) Chondrule formation in bow shocks around eccentric planetary embryos. *Astrophys. J.* **752**, 27 (17pp).

Morris M. A., Weidenschilling S. J. and Desch S. J. (2016) The effect of multiple particle sizes on cooling rates of chondrules produced in large-scale shocks in the solar nebula. *Meteorit. Planet. Sci.* **51**, 870–883.

Nagasawa M., Tanaka K. K., Tanaka H., Nakamoto T., Miura H. and Yamamoto T. (2014) Revisiting Jovian-resonance induced chondrule formation. *Astrophys. J. Lett.* **794**, L7 (5pp).

Nagasawa M., Tanaka K. K., Tanaka H., Nomura H., Nakamoto T. and Miura H. (2019) Shock-generating planetesimals perturbed by a giant planet in a gas disk. *Astrophys. J.* **871**, 110 (15pp).

Nagashima K., Krot A. N. and Huss G. R. (2014) ^{26}Al in chondrules from CR2 chondrites. *Geochem. J.* **48**, 561–570.

Nagashima K., Krot A. N. and Huss G. R. (2015) Oxygen-isotope compositions of chondrule phenocrysts and matrix grains in Kakangari K-grouplet chondrite: Implication to a chondrule-matrix genetic relationship. *Geochim. Cosmochim. Acta* **151**, 49–67.

Nagashima K., Krot A. N. and Komatsu M. (2017) ^{26}Al–^{26}Mg systematics in chondrules from Kaba and Yamato 980145 CV3 carbonaceous chondrites. *Geochim. Cosmochim. Acta* **201**, 303–319.

Nagashima K., Kita N. T. and Luu T.-H. (2018) ^{26}Al-^{26}Mg systematics of chondrules. In *Chondrules: Records of Protoplanetary Disk Processes* (eds. S. S. Russell, H. C.

Connolly, and A. N. Krot). Cambridge University Press. pp. 247–275.

Nakashima D., Ushikubo T., Joswiak D. J., Brownlee D. E., Matrajt G., Weisberg M. K., Zolensky M. E. and Kita N. T. (2012) Oxygen isotopes in crystalline silicates of comet Wild 2: A comparison of oxygen isotope systematics between Wild 2 particles and chondritic materials. *Earth Planet. Sci. Lett.* **357**–**358**, 355–365.

Nishiizumi K. (2004) Preparation of ^{26}Al AMS standards. *Nucl. Instruments Methods Phys. Res. Sect. B Beam Interact. with Mater. Atoms* **223**–**224**, 388–392.

Nittler L. R., Alexander C. M. O'D., Patzer A. and Verdier-Paoletti M. J. (2021) Presolar stardust in highly pristine CM chondrites Asuka 12169 and Asuka 12236. *Meteorit. Planet. Sci.* **276**, 260–276.

Öberg K. I. and Wordsworth R. (2019) Jupiter's Composition Suggests its Core Assembled Exterior to the N_2 Snowline. *Astron. J.* **158**, 194 (9pp).

Olsen M. B., Wielandt D., Schiller M., Van Kooten E. M. M. E. and Bizzarro M. (2016) Magnesium and ^{54}Cr isotope compositions of carbonaceous chondrite chondrules – Insights into early disk processes. *Geochim. Cosmochim. Acta* **191**, 118–138.

Palme H., Hezel D. C. and Ebel D. S. (2015) The origin of chondrules: Constraints from matrix composition and matrix-chondrule complementarity. *Earth Planet. Sci. Lett.* **411**, 11–19.

Paneque-Carreño T., Pérez L. M., Benisty M., Hall C., Veronesi B., Lodato G., Sierra A., Carpenter J. M., Andrews S. M., Bae J., Henning T., Kwon W., Linz H., Loinard L., Pinte C., Ricci L., Tazzari M., Testi L. and Wilner D. (2021) Spiral Arms and a Massive Dust Disk with Non-Keplerian Kinematics: Possible Evidence for Gravitational Instability in the Disk of Elias 2–27. *Astrophys. J.* **914**, 88 (28pp).

Pape J., Mezger K., Bouvier A. S. and Baumgartner L. P. (2019) Time and duration of chondrule formation: Constraints from ^{26}Al-^{26}Mg ages of individual chondrules.

Geochim. Cosmochim. Acta **244**, 416–436.

Pape J., Rosén V., Mezger K. and Guillong M. (2021) Primary crystallization and partial remelting of chondrules in the protoplanetary disk: Petrographic, mineralogical and chemical constraints recorded in zoned type-I chondrules. *Geochim. Cosmochim. Acta* **292**, 499–517.

Pérez L. M., Carpenter J. M., Andrews S. M., Ricci L., Isella A., Linz H., Sargent A. I., Wilner D. J., Henning T., Deller A. T., Chandler C. J., Dullemond C. P., Lazio J., Menten K. M., Corder S. A., Storm S., Testi L., Tazzari M., Kwon W., Calvet N., Greaves J. S., Harris R. J. and Mundy L. G. (2016) Spiral density waves in a young protoplanetary disk. *Science.* **353**, 1519–1521.

Pirani S., Johansen A., Bitsch B., Mustill A. J. and Turrini D. (2019) Consequences of planetary migration on the minor bodies of the early solar system. *Astron. Astrophys.* **623**, A169.

Rudraswami N. G. and Goswami J. N. (2007) ^{26}Al in chondrules from unequilibrated L chondrites: Onset and duration of chondrule formation in the early solar system. *Earth Planet. Sci. Lett.* **257**, 231–244.

Rudraswami N. G., Goswami J. N., Chattopadhyay B., Sengupta S. K. and Thapliyal A. P. (2008) ^{26}Al records in chondrules from unequilibrated ordinary chondrites: II. Duration of chondrule formation and parent body thermal metamorphism. *Earth Planet. Sci. Lett.* **274**, 93–102.

Rudraswami N. G., Ushikubo T., Nakashima D. and Kita N. T. (2011) Oxygen isotope systematics of chondrules in the Allende CV3 chondrite: High precision ion microprobe studies. *Geochim. Cosmochim. Acta* **75**, 7596–7611.

Sanborn M. E., Carlson R. W. and Wadhwa M. (2015) ^{147,146}Sm-^{143,142}Nd, ^{176}Lu-^{176}Hf, and ^{87}Rb-^{87}Sr systematics in the angrites: Implications for chronology and processes on the angrite parent body. *Geochim. Cosmochim. Acta* **171**, 80–99.

Sanborn M. E., Wimpenny J., Williams C. D., Yamakawa A., Amelin Y., Irving A. J. and Yin Q. Z. (2019) Carbonaceous achondrites Northwest Africa 6704/6693: Milestones for early Solar System chronology and genealogy. *Geochim. Cosmochim. Acta* **245**, 577–596.

Sanders I. S. and Scott E. R. D. (2012) The origin of chondrules and chondrites: Debris from low-velocity impacts between molten planetesimals? *Meteorit. Planet. Sci.* **47**, 2170–2192.

Sano Y., Takada M., Takahata N., Fujiya W. and Sugiura N. (2014) Ion microprobe Al-Mg dating of single plagioclase grains in an Efremovka chondrule. *Geochem. J.* **48**, 133–144.

Schiller M., Connelly J. N., Glad A. C., Mikouchi T. and Bizzarro M. (2015) Early accretion of protoplanets inferred from a reduced inner solar system ^{26}Al inventory. *Earth Planet. Sci. Lett.* **420**, 45–54.

Schneider J. M., Burkhardt C., Marrocchi Y., Brennecka G. A. and Kleine T. (2020) Early evolution of the solar accretion disk inferred from Cr-Ti-O isotopes in individual chondrules. *Earth Planet. Sci. Lett.* **551**, 116585.

Schrader D. L. and Davidson J. (2017) CM and CO chondrites: A common parent body or asteroidal neighbors? Insights from chondrule silicates. *Geochim. Cosmochim. Acta* **214**, 157–171.

Schrader D. L., Connolly H. C. J., Lauretta D. S., Nagashima K., Huss G. R., Davidson J. and Domanik K. J. (2013) The formation and alteration of the Renazzo-like carbonaceous chondrites II: Linking O-isotope composition and oxidation state of chondrule olivine. *Geochim. Cosmochim. Acta* **101**, 302–327.

Schrader D. L., Nagashima K., Krot A. N., Ogliore R. C. and Hellebrand E. (2014) Variations in the O-isotope composition of gas during the formation of chondrules from the CR chondrites. *Geochim. Cosmochim. Acta* **132**, 50–74.

Schrader D. L., Nagashima K., Krot A. N., Ogliore R. C., Yin Q.-Z., Amelin Y., Stirling C. H. and Kaltenbach A. (2017) Distribution of ^{26}Al in the CR chondrite chondrule-forming region of the protoplanetary disk. *Geochim. Cosmochim. Acta* **201**, 275–302.

Schrader D. L., Nagashima K., Waitukaitis S. R., Davidson J., McCoy T. J., Connolly H. C. and Lauretta D. S. (2018a) The retention of dust in protoplanetary disks: Evidence from agglomeratic olivine chondrules from the outer Solar System. *Geochim. Cosmochim. Acta* **223**, 405–421.

Schrader D. L., Fu R. R., Desch S. J. and Davidson J. (2018b) The background temperature of the protoplanetary disk within the first four million years of the Solar System. *Earth Planet. Sci. Lett.* **504**, 30–37.

Schrader D. L., Nagashima K., Davidson J., McCoy T. J., Ogliore R. C. and Fu R. R. (2020) Outward migration of chondrule fragments in the early Solar System: O-isotopic evidence for rocky material crossing the Jupiter Gap? *Geochim. Cosmochim. Acta* **282**, 133–155.

Scott E. R. D. and Krot A. N. (2014) Chondrites and Their Components. In *Treatise on Geochemistry* (eds. H. Holland and K. Turekian). Elsevier, Oxford. pp. 65–137.

Shimizu K., Alexander C. M. O'D., Hauri E. H., Sarafian A. R., Nittler L. R., Wang J., Jacobsen S. D. and Mendybaev R. A. (2021) Highly volatile element (H, C, F, Cl, S) abundances and H isotopic compositions in chondrules from carbonaceous and ordinary chondrites. *Geochim. Cosmochim. Acta* **301**, 230–258.

Siron G., Fukuda K., Kimura M. and Kita N. T. (2021a) New constraints from ^{26}Al–^{26}Mg chronology of anorthite bearing chondrules in unequilibrated ordinary chondrites. *Geochim. Cosmochim. Acta* **293**, 103–126.

Siron G., Kita N. T., Fukuda K. and Kimura M. (2021b) High precision Al-Mg chronology of chondrules in unequilibrated ordinary chondrites. *52nd Lunar Planet. Sci. Conf.*, abstract #1639.

Smith J. V. (1984) Phase relatios of plagioclase feldspars. In *Feldspars and Feldspathoids* (ed. W. L. Brown). Springer, Dordrecht. pp. 55–94.

Sugiura N. and Fujiya W. (2014) Correlated accretion ages and ε^{54}Cr of meteorite parent bodies and the evolution of the solar nebula. *Meteorit. Planet. Sci.* **49**, 772–787.

Sutton S., Alexander C. M. O'D., Bryant A., Lanzirotti A., Newville M. and Cloutis E. A. (2017) The bulk valence state of Fe and the origin of water in chondrites. *Geochim. Cosmochim. Acta* **211**, 115–132.

Tanaka H., Murase K. and Tanigawa T. (2020) Final masses of giant planets III: Effect of photoevaporation and a new planetary migration model. *Astrophys. J.* **891**, 143 (11pp).

Tenner T. J., Ushikubo T., Kurahashi E., Kita N. T. and Nagahara H. (2013) Oxygen isotope systematics of chondrule phenocrysts from the CO3.0 chondrite Yamato 81020: Evidence for two distinct oxygen isotope reservoirs. *Geochim. Cosmochim. Acta* **102**, 226–245.

Tenner T. J., Nakashima D., Ushikubo T., Kita N. T. and Weisberg M. K. (2015) Oxygen isotope ratios of FeO-poor chondrules in CR3 chondrites: Influence of dust enrichment and H_2O during chondrule formation. *Geochim. Cosmochim. Acta* **148**, 228–250.

Tenner T. J., Kimura M. and Kita N. T. (2017) Oxygen isotope characteristics of chondrules from the Yamato-82094 ungrouped carbonaceous chondrite: Further evidence for common O-isotope environments sampled among carbonaceous chondrites. *Meteorit. Planet. Sci.* **52**, 268–294.

Tenner T. J., Ushikubo T., Nakashima D., Schrader D. L., Weisberg M. K., Kimura M. and Kita N. T. (2018a) Oxygen isotope characteristics of chondrules from recent studies by secondary ion mass spectrometry. In *Chondrules: Records of Protoplanetary Disk Processes* (eds. S. S. Russell, H. C. Connolly, and A. N. Krot). Cambridge University Press. pp. 196–246.

Tenner T. J., Kimura M. and Kita N. T. (2018b) Further characterizing the extent of metamorphism within the Dominion Range 08006 CO3 chondrite. *49th Lunar Planet. Sci. Conf.*, abstract #1510.

Tenner T. J., Nakashima D., Ushikubo T., Tomioka N., Kimura M., Weisberg M. K. and Kita N. T. (2019) Extended chondrule formation intervals in distinct physicochemical environments: Evidence from Al-Mg isotope systematics of CR chondrite chondrules with unaltered plagioclase. *Geochim. Cosmochim. Acta* **260**, 133–160.

Tissandier L., Libourel G. and Robert F. (2002) Gas-melt interactions and their bearing on chondrule formation. *Meteorit. Planet. Sci.* **37**, 1377–1389.

Tomida K., Machida M. N., Hosokawa T., Sakurai Y. and Lin C. H. (2017) Grand design spiral arms in a young forming circumstellar disk. *Astrophys. J. Lett.* **835**, L11 (8pp).

Ushikubo T., Kimura M., Kita N. T. and Valley J. W. (2012) Primordial oxygen isotope reservoirs of the solar nebula recorded in chondrules in Acfer 094 carbonaceous chondrite. *Geochim. Cosmochim. Acta* **90**, 242–264.

Ushikubo T., Nakashima D., Kimura M., Tenner T. J. and Kita N. T. (2013) Contemporaneous formation of chondrules in distinct oxygen isotope reservoirs. *Geochim. Cosmochim. Acta* **109**, 280–295.

Ushikubo T., Tenner T. J., Hiyagon H. and Kita N. T. (2017) A long duration of the ^{16}O-rich reservoir in the solar nebula, as recorded in fine-grained refractory inclusions from the least metamorphosed carbonaceous chondrites. *Geochim. Cosmochim. Acta* **201**, 103–122.

van der Marel N., van Dishoeck E. F., Bruderer S., Birnstiel T., Pinilla P., Dullemond C. P., van Kempen T. A., Schmalzl M., Brown J. M., Herczeg G. J., Mathews G. S. and Geers V. (2013) A major asymmetric dust trap in a transition disk. *Science.* **340**, 1199–1202.

van Kooten E. M. M. E., Wielandt D., Schiller M., Nagashima K., Thomen A., Larsen K. K., Olsen M. B., Nordlund Å., Krot A. N. and Bizzarro M. (2016) Isotopic evidence for primordial molecular cloud material in metal-rich carbonaceous chondrites. *Proc. Natl. Acad. Sci.* **113**, 2011–2016.

van Kooten E. M. M. E., Cavalcante L., Wielandt D. and Bizzarro M. (2020) The role of Bells in the continuous accretion between the CM and CR chondrite reservoirs. *Meteorit. Planet. Sci.* **55**, 575–590.

van Kooten E., Schiller M., Moynier F., Johansen A., Haugbølle T. and Bizzarro M. (2021) Hybrid accretion of carbonaceous chondrites by radial transport across the Jupiter barrier. *Astrophys. J.* **910**, 70 (18pp).

Van Orman J. A., Cherniak D. J. and Kita N. T. (2014) Magnesium diffusion in plagioclase: Dependence on composition, and implications for thermal resetting of the ^{26}Al-^{26}Mg early solar system chronometer. *Earth Planet. Sci. Lett.* **385**, 79–88.

Villeneuve J., Chaussidon M. and Libourel G. (2009) Homogeneous distribution of ^{26}Al in the solar system from the mg isotopic composition of chondrules. *Science.* **325**, 985–988.

Wakaki S., Itoh S., Tanaka T. and Yurimoto H. (2013) Petrology, trace element abundances and oxygen isotopic compositions of a compound CAI-chondrule object from Allende. *Geochim. Cosmochim. Acta* **102**, 261–279.

Wakita S. and Sekiya M. (2011) Thermal evolution of icy planetesimals in the solar nebula. *Earth, Planets Sp.* **63**, 1193–1206.

Wakita S., Matsumoto Y., Oshino S. and Hasegawa Y. (2017) Planetesimal Collisions As a Chondrule Forming Event. *Astrophys. J.* **834**, 125 (8pp).

Walsh K. J., Morbidelli A., Raymond S. N., O'Brien D. P. and Mandell A. M. (2011) A low mass for Mars from Jupiter's early gas-driven migration. *Nature* **475**, 206–209.

Warren P. H. (2011) Stable-isotopic anomalies and the accretionary assemblage of the Earth and Mars: A subordinate role for carbonaceous chondrites. *Earth Planet. Sci. Lett.* **311**, 93–100.

Wasserburg G. J., Wimpenny J. and Yin Q.-Z. (2012) Mg isotopic heterogeneity, Al-Mg isochrons, and canonical $^{26}Al/^{27}Al$ in the early solar system. *Meteorit. Planet. Sci.* **47**, 1980–1997.

Weidenschilling S. J., Marzari F. and Hood L. L. (1998) The origin of chondrules at Jovian resonances. *Science.* **279**, 681–684.

Weisberg M. K., Ebel D. S., Connolly H. C., Kita N. T. and Ushikubo T. (2011) Petrology and oxygen isotope compositions of chondrules in E3 chondrites. *Geochim. Cosmochim. Acta* **75**, 6556–6569.

Weisberg M. K., Kita N. T., Fukuda K., Siron G. and Ebel D. S. (2021) Micro-distribution of Oxygen Isotopes in Unequilibrated Enstatite Chondrites. *Geochim. Cosmochim. Acta* **300**, 279–295.

Williams C. D., Sanborn M. E., Defouilloy C., Yin Q. Z., Kita N. T., Ebel D. S., Yamakawa A. and Yamashita K. (2020) Chondrules reveal large-scale outward transport of inner Solar System materials in the protoplanetary disk. *Proc. Natl. Acad. Sci. U. S. A.* **117**, 23426–23435.

Wood J. A. (1996) Processing of chondritic and planetary material in spiral density waves in the nebula. *Meteorit. Planet. Sci.* **31**, 641–645.

Young E. D. and Russell S. S. (1998) Oxygen reservoirs in the early solar nebula inferred from an Allende CAI. *Science.* **282**, 452–455.

Yurimoto H. and Wasson J. T. (2002) Extremely rapid cooling of a carbonaceous-chondrite chondrule containing very ^{16}O-rich olivine and a ^{26}Mg-excess. *Geochim. Cosmochim. Acta* **66**, 4355–4363.

Yurimoto H. and Kuramoto K. (2004) Molecular cloud origin for the oxygen isotope heterogeneity in the solar system. *Science.* **305**, 1763–1766.

Zhang M., Lin Y., Tang G., Liu Y. and Leya I. (2020) Origin of Al-rich chondrules in CV chondrites: Incorporation of diverse refractory components into the ferromagnesian chondrule-forming region. *Geochim. Cosmochim. Acta* **272**, 198–217.

Zhang M., Defouilloy C., Joswiak D. J., Brownlee D. E., Nakashima D., Siron G., Kitajima K. and Kita N. T. (2021) Oxygen isotope systematics of crystalline silicates in a giant cluster IDP: A genetic link to Wild 2 particles and primitive chondrite chondrules. *Earth Planet. Sci. Lett.* **564**, 116928.

Figure captions

Fig. 1. Backscattered electron images of chondrules from the Asuka 12236 (CM2.9) carbonaceous chondrite. White rectangles in Fig. 1a, 1c, and 1g indicate areas shown as expanded views in Fig. 1b, 1d, and 1h, respectively. (a–b) A21, type I PO chondrule. Al-Mg SIMS pits on plagioclase are shown in Fig. 1b. (c–d) A28, type I PO chondrule. Oxygen isotope SIMS pits on plagioclase are shown in Fig. 1d. Some mesostases appear to be aqueously altered (Fig. 1d). (e) A184, type I PO chondrule. (f) A207, type I PO chondrule. (g–h) A75, type I POP chondrule. This chondrule is mineralogically zoned (large olivine crystals in the core → interstitial plagioclase → low-Ca pyroxene in the outermost shell). Small olivine grains are poikilitically enclosed in low-Ca pyroxene (Fig. 1h). Mineral phases shown are olivine (ol), low-Ca pyroxene (lpx), high-Ca pyroxene (hpx), and plagioclase (pl).

Fig. 2. Backscattered electron images of chondrules from the DOM 08006 (CO3.01) carbonaceous chondrite. (a–c) type I POP chondrules D41 (Fig. 2a), D59 (Fig. 2b), and D109 (Fig. 2c). (d) D10, type I PP chondrule. (e) D89, type I POP chondrule. A white rectangle in Fig. 2e indicates an area shown as an expanded view in Fig. 5a, in which plagioclase grains were investigated by TEM. (f) D198, Al-rich chondrule. A white rectangle in Fig. 2f indicates an area shown as an expanded view in Fig. 2g, which shows corroded spinel grains enclosed by plagioclase. Mineral phases shown are olivine (ol), low-Ca pyroxene (lpx), high-Ca pyroxene (hpx), plagioclase (pl), and spinel (spi).

Fig. 3. Comparison of mean Mg#s of low-Ca pyroxene and olivine within individual chondrules from Asuka 12236 and DOM 08006. The solid line represents a one to one relationship. Error bars represent the range of values from EPMA analyses.

Fig. 4. (a–c) Excess silica ($[\ ]Si_4O_8$) and (d–f) MgO concentrations (wt.%) in plagioclase as a function of Anorthite content (An = [Ca]/[Ca + Na + K] molar %) in chondrules from Asuka 12236 (Fig. 4a and d), DOM 08006 (Fig. 4b and e), and Yamato-81020 (Fig. 4c and f). Legends for Fig. 4d, 4e, and 4f are the same as those in Fig. 4a, 4b, and 4c, respectively. Individual EPMA data are reported in Supplementary Material 6.

Fig. 5. Electron micrographs of plagioclase from chondrule D89 from DOM 08006. (a) Back scattered electron image of a location sectioned by FIB. (b) Bright-field TEM image of the FIB section, consisting of two plagioclase (pl) grains with an interstitial low-Ca pyroxene (lpx) grain. The arrows show the surface of the petrographic thin section. (c) HAADF-STEM (Z-contrast) image showing the plagioclase grains are chemically homogeneous (elemental

EDS maps are shown in Supplementary Fig. S3). (d) High resolution TEM (HRTEM) image of the plagioclase grain-1 showing no inclusions are present, even down to the nm-scale. (e) Selected-area electron diffraction (SAED) patterns from the plagioclase grain along the [201] zone axis corresponding to high-temperature phase with a body-centered cell. (f) SAED pattern for the plagioclase grain-2 along the [1$\bar{1}$0] zone axis showing faint extra reflections corresponding to the low-temperature phase with a primitive cell.

Fig. 6. Oxygen three-isotope diagrams for chondrules from (a–e) Asuka 12236 and (f–k) DOM 08006. Reference lines are Terrestrial Fractionation (TF; Clayton et al., 1991), Young and Russell (Y&R; Young and Russell, 1998), Primitive Chondrule Minerals (PCM; Ushikubo et al., 2012), and Carbonaceous Chondrite Anhydrous Mineral (CCAM; Clayton et al., 1977) lines. Error bars are 2SD.

Fig. 7. (a) Mean oxygen isotope ratios of individual chondrules from Asuka 12236 and DOM 08006, and individual mineral analyses of chondrule A75 from Asuka 12236. Mean oxygen isotope ratios of chondrules from L/LL3.00–3.05 chondrites ([1] Kita et al., 2010; [2] Siron et al., 2021a) and four chondrules (Y20, Y24, Y71, Y175) from Yamato-81020 ([3] Tenner et al., 2013) are also shown. TF, Y&R, CCAM, and PCM represent terrestrial fractionation (Clayton et al., 1991), the Young and Russell (Young and Russell, 1998), the Carbonaceous Chondrite Anhydrous Mineral (Clayton et al., 1977), and Primitive Chondrule Minerals (Ushikubo et al., 2012) lines, respectively. (b) Relationships between oxygen isotope ratios and Mg#s of chondrules from Asuka 12236 and DOM 08006. Mean $\Delta^{17}O$ values are shown for 10 out of 11 chondrules we studied, except for chondrule A75 from Asuka 12236. Those for chondrules from UOC ([1] Kita et al., 2010; [2] Siron et al., 2021a), Acfer 094 ([4] Ushikubo et al., 2012), CV ([5–6] Hertwig et al., 2018; 2019b), CO ([3] Tenner et al., 2013),

CM ([7] Chaumard et al., 2018), and CR ([8–10] Schrader et al., 2013, 2014; Tenner et al., 2019) are also plotted. Solid curves are from the oxygen isotope mixing model with variable H_2O ice enhancement factors relative to CI chondritic proportions and under variable dust enrichment factors relative to solar abundance (Hertwig et al., 2018, see Supplementary Material 1 and Tenner et al., 2015 for more details about the mixing model). Note that mixing curves in Tenner et al. (2015) used different $\Delta^{17}O$ values for precursor components of the anhydrous silicate and H_2O-ice so that the estimated dust enrichment and ice enhancement factors for CR chondrules in Tenner et al. (2015) are systematically higher in the former and lower in the latter than those indicated in Fig. 7b (see Supplementary Material 1 for more details). For mean Mg#s, error bars represent the range of values from EPMA analyses. For $\Delta^{17}O$ values, error bars are 2σ. For clarity, error bars for literature data are not shown.

Fig. 8. Oxygen three-isotope diagrams for four chondrules (Y20, Y24, Y71, Y175) from Yamato-81020. Olivine and pyroxene data are from [1] Tenner et al. (2013), while plagioclase data were obtained in this study. Reference lines are Terrestrial Fractionation (TF; Clayton et al., 1991), Young and Russell (Y&R; Young and Russell, 1998), Primitive Chondrule Minerals (PCM; Ushikubo et al., 2012), and Carbonaceous Chondrite Anhydrous Mineral (CCAM; Clayton et al., 1977) lines. Dashed lines indicate the linear regression with a slope of ~0.7 through the oxygen isotope data for the bulk CM chondrites and anhydrous mineral separates of Murchison (Clayton and Mayeda, 1984, 1999). Error bars are 2SD.

Fig. 9. Al-Mg isochron diagrams for chondrules from (a–d) Asuka 12236, (e–j) DOM 08006, and (k–n) Yamato-81020. Solid lines represent isochron regression lines obtained by using Isoplot 4.15 (Ludwig, 2012). Similar scales of X and Y are applied to each diagram for proper comparisons of slopes from individual regression lines. Error envelopes (dashed curves) are

95% confidence. Error bars are 2σ. pl = plagioclase, lpx = low-Ca pyroxene, ol = olivine.

Fig. 10. Comparison of $(^{26}Al/^{27}Al)_0$ and corresponding Al-Mg ages of chondrules from CO chondrites Yamato-81020 and DOM 08006. Open square symbols represent $(^{26}Al/^{27}Al)_0$ of four Y-81020 chondrules reported in [1] Kurahashi et al. (2008), which are systematically higher than those obtained in this study (closed black square symbols). Error bars represent 2σ or 95% confidence intervals.

Fig. 11. (a) Compilation of the $(^{26}Al/^{27}Al)_0$ and corresponding Al-Mg ages of chondrules from the least altered chondrites (petrologic subtype 2.9–3.1) determined by recent high precision SIMS analyses. Data from; UOC ([1–2] Siron et al., 2021a, 2021b), CO (this study), CM (this study), Acfer 094 ([3] Ushikubo et al., 2013; [4] Hertwig et al., 2019a), CV ([5] Nagashima et al., 2017), CR ([6] Nagashima et al., 2014; [7] Schrader et al., 2017; [8] Tenner et al., 2019). A grey shaded area represents a range of $(^{26}Al/^{27}Al)_0$ of UOC chondrules (L/LL ≤3.1) reported in previous studies (Siron et al., 2021a, 2021b; Hutcheon and Hutchison, 1989, Kita et al, 2000; Rudraswami and Goswami 2007; Rudraswami et al., 2008; Villeneuve et al., 2009; Mishra et al., 2010; Pape et al., 2019; Bollard et al., 2019). Three chondrules (A75, G39, G85) exhibit relatively ^{16}O-depleted oxygen isotope characteristics, which might have formed inside the disk region relative to where the majority of CC chondrules formed (see sections 4.3 and 4.6). (b) The Kernel density estimates of $(^{26}Al/^{27}Al)_0$ for chondrules from UOCs [red for Siron et al. (2021a, 2021b) (*n* = 31) and grey for all literature data (*n* = 102)], CRs (gold; *n* = 33), and other carbonaceous chondrites (CV, CO, CM, and Acfer 094; blue; *n* = 37). The three ^{16}O-depleted chondrules (A75, G39, G85) are not included in this plot. Data sources are the same as those listed for Fig. 11a. $(^{26}Al/^{27}Al)_0$ of three UOC chondrules

("n = 3") exceeds the upper bound (1.2×10^{-5}) of the plotted range, although two out of the three are not resolvable from 1×10^{-5}.

Fig. 12. A temporal shift of chondrule generation and chondrule transport from the inner to outer Solar System. (a) At ≤1 Ma after CAIs, a physical barrier formed between the NC and CC reservoirs, which is probably related to the formation of proto-Jupiter (Kruijer et al., 2017; Brasser and Mojzsis, 2020). According to Desch et al. (2018), we assume that the physical barrier located at 3 AU from the Sun. (b) At ≤2.2 Ma after CAIs, the majority of ordinary chondrite (OC) chondrules as well as chondrules G39 and G85 from Acfer 094 formed at the inner Solar System. Chondrule A75 from Asuka 12236, which contains ^{16}O-depleted relict grains, formed at outside of the OC chondrule-forming regions at the time of 1.9 Ma after CAIs. Chondrule G39 and G85 as well as the ^{16}O-depleted relict grains in chondrule A75 may have passed through the physical barrier, as suggested for OC-like materials found in CCs (Schrader et al., 2020; Williams et al., 2020). (c) At ~2.2–2.8 Ma after CAIs, the majority of chondrules from CV, CO, CM, and Acfer 094 formed in regions exterior to those where OC chondrules formed. Chondrules G39, G85, and A75 traveled from the inner to the outer part of the solar protoplanetary disk within ~1 Ma. (d) After 2.8 Ma, the majority of CR chondrules formed in parts exterior to the CV, CO, CM, and Acfer 094 chondrule-forming regions.

Table 1. Compilation of mean Mg#s and oxygen isotope ratios of 15 FeO-poor chondrules from Asuka 12236 (CM2.9), DOM 08006 (CO3.01), and Yamato-81020 (CO3.05) carbonaceous chondrites

chondrule#	Type		Mg#[a]		Ol[b]		Lpx[b]		Hpx[b]		Mean oxygen isotope ratios						
			Mean	Unc.	Relict[c]	Host	Relict[c]	Host	Relict[c]	Host	$\delta^{18}O$	Unc.[d]	$\delta^{17}O$	Unc.[d]	$\Delta^{17}O$	Unc.[d]	Ref.[e]
Asuka 12236																	
A21	I	PP	98.9	(−0.7/+0.3)	−	2	−	6	−	−	−2.75	0.38	−5.96	0.21	−4.53	0.13	[1]
A28	I	PP	98.9	(−0.2/+0.1)	−	−	−	6	−	−	−2.64	0.35	−5.72	0.20	−4.35	0.15	[1]
A75	I	POP	99.4	(−0.5/+0.3)	−	−	−	−	−	−			*-Heterogeneous-*				[1]
A184	I	PP	99.1	(−0.4/+0.4)	−	4	−	4	−	−	−4.56	0.53	−7.71	0.40	−5.34	0.18	[1]
A207	I	PP	98.9	(−0.6/+0.2)	1	3	−	3	−	−	−4.22	0.39	−7.68	0.28	−5.48	0.20	[1]
DOM 08006																	
D10	I	PP	98.7	(−0.3/+0.3)	1	1	−	6	−	−	−2.49	0.52	−5.65	0.32	−4.36	0.12	[1]
D41	I	POP	98.9	(−0.7/+0.3)	−	2	−	4	−	−	−4.78	0.39	−8.06	0.20	−5.57	0.12	[1]
D59	I	POP	98.5	(−0.8/+0.5)	−	3	−	3	−	1	−2.30	0.46	−5.70	0.36	−4.50	0.20	[1]
D89	I	PO	99.2	(−0.4/+0.2)	4	1	−	3	−	−	−6.23	0.44	−9.49	0.26	−6.25	0.19	[1]
D109	I	POP	98.6	(−0.5/+0.3)	−	4	−	4	−	−	−2.35	0.34	−5.32	0.21	−4.09	0.16	[1]
D198	ARC		99.1	(−0.1/+0.2)	1	3	−	2	−	−	−3.41	0.41	−6.74	0.45	−4.97	0.31	[1]
Yamato-81020																	
Y20	I	POP	99.3		−	4	−	3	−	−	−6.98	0.52	−10.02	0.39	−6.39	0.24	[2]
Y24	I	POP	99.0		−	4	−	4	−	2	−4.57	0.47	−7.12	0.27	−4.75	0.17	[2]
Y71	I	PP	98.7		−	−	1	2	−	2	−4.68	0.72	−7.52	0.47	−5.22	0.21	[2]
Y175	ARC		99.1		−	−	−	3	−	−	−5.83	0.49	−8.81	0.64	−5.77	0.42	[2]

[a]Mean Mg# (=[Mg] / [Mg + Fe] molar%) of olivine and/or pyroxene. Uncertainties represent the range in measured Mg#s of those olivine and/or pyroxene.

[b]Number of oxygen isotope analyses of olivine (Ol), low-Ca pyroxene (Lpx, Wo < 10), and high-Ca pyroxene (Hpx, Wo ≥ 10).

[c]Relict grains not included to calculate mean oxygen isotope ratios.

[d]Calculation of uncertainties are described in Supplementary Material 1.

[e]References: [1] This study, [2] Tenner et al. (2013)

Table 2. Average major and minor element compositions (wt.%), An contents, and excess silica components of plagioclase determined with EPMA

chondrule#	SiO_2	TiO_2	Al_2O_3	MgO	FeO	CaO	Na_2O	K_2O	MnO	Oxide Total	N[a]	An[b]	±[c]	[ ]Si_4O_8	±[c]
Asuka 12236															
A21	46.84	0.12	33.30	0.75	0.40	18.43	0.46	0.04	b.d.	100.34	28	95.7	(−7.4/+3.5)	0.032	(−0.029/+0.025)
A28	50.96	b.d.	29.93	1.06	0.38	16.61	0.98	0.05	0.11	100.08	10	90.3	(−3.8/+1.6)	0.083	(−0.014/+0.009)
A75	46.50	b.d.	32.59	0.92	0.04	18.25	0.51	0.04	0.13	98.99	16	95.1	(−2.8/+2.2)	0.031	(−0.022/+0.016)
A184	46.54	0.09	33.44	0.84	0.36	18.51	0.60	0.04	0.11	100.52	13	94.5	(−6.3/+4.3)	0.020	(−0.020/+0.019)
A207	45.68	0.12	33.09	0.86	0.51	18.59	0.63	b.d.	0.09	99.57	10	94.2	(−2.0/+1.3)	0.005	(−0.005/+0.007)
DOM 08006															
D10	46.95	b.d.	32.33	0.93	0.50	18.29	0.91	b.d.	b.d.	99.91	27	91.7	(−5.1/+4.2)	0.007	(−0.007/+0.016)
D41	46.29	0.05	32.95	0.85	0.57	18.67	0.41	b.d.	0.07	99.86	22	96.2	(−1.0/+1.3)	0.021	(−0.016/+0.013)
D59	46.34	b.d.	33.15	0.99	0.42	18.64	0.77	b.d.	b.d.	100.31	11	93.0	(−2.1/+1.4)	0.001	(−0.001/+0.004)
D89	46.77	0.05	32.64	0.96	0.46	18.72	0.16	b.d.	b.d.	99.76	16	98.5	(−1.8/+0.9)	0.040	(−0.017/+0.018)
D109	46.54	0.05	32.46	0.92	0.47	18.55	0.60	b.d.	0.09	99.67	25	94.4	(−1.6/+1.3)	0.015	(−0.010/+0.012)
D198	45.74	0.05	34.37	0.66	0.20	19.14	0.34	b.d.	b.d.	100.50	22	96.9	(−3.6/+1.2)	0.015	(−0.015/+0.012)
Yamato-81020															
Y20	46.40	0.07	32.92	0.88	0.30	18.45	0.64	b.d.	b.d.	99.67	7	94.1	(−1.7/+0.9)	0.015	(−0.011/+0.011)
Y24	45.75	b.d.	33.95	0.87	0.40	18.51	0.71	b.d.	0.07	100.25	5	93.6	(−4.2/+4.6)	0.005	(−0.005/+0.020)
Y71	47.82	b.d.	32.49	0.87	0.30	18.19	0.62	b.d.	b.d.	100.29	5	94.2	(−4.2/+3.2)	0.039	(−0.021/+0.012)
Y175	49.01	0.07	31.11	0.84	0.15	16.72	1.51	0.03	0.10	99.53	4	86.0	(−6.2/+4.0)	0.032	(−0.021/+0.020)

[a]Number of EPMA analyses
[b]An = [Ca] / [Ca + Na + K] molar%
[c]Uncertainties represent the range in measured values.

Table 3. Summary of the Al-Mg isotope systematics of 15 FeO-poor chondrules from the Asuka 12236 (CM2.9), DOM 08006 (CO3.01), and Yamato-81020 (CO3.05) carbonaceous chondrites

chondrule#	$(\delta^{26}Mg)_0$* [‰]	Unc. [‰]	$(^{26}Al/^{27}Al)_0$ ($\times 10^{-6}$)	Unc. ($\times 10^{-6}$)	Age relative to CAI [Ma]	Unc. [Ma]	MSWD	N[a]
Asuka 12236								
A21	−0.036	0.063	4.7	0.5	2.45	(−0.11/+0.12)	0.9	12
A28	0.012	0.063	3.5	0.9	2.76	(−0.23/+0.30)	0.4	7
A75	−0.044	0.047	8.0	0.7	1.92	(−0.09/+0.09)	0.7	10
A184	−0.007	0.050	4.3	0.6	2.55	(−0.14/+0.16)	0.5	12
A207	−0.049	0.045	4.1	0.9	2.59	(−0.21/+0.26)	1.0	7
DOM 08006								
D10	0.005	0.050	4.1	0.9	2.58	(−0.20/+0.26)	0.5	8
D41	0.032	0.045	4.7	0.8	2.46	(−0.16/+0.20)	1.3	8
D59	0.018	0.043	3.6	0.9	2.72	(−0.22/+0.28)	0.7	9
D89	0.024	0.044	5.3	0.6	2.33	(−0.10/+0.11)	1.0	11
D109	0.100	0.040	4.6	0.6	2.48	(−0.12/+0.14)	1.4	12
D198	0.043	0.047	4.3	0.5	2.55	(−0.11/+0.12)	1.5	12
Yamato-81020								
Y20	−0.01	0.068	6.0	0.6	2.21	(−0.10/+0.11)	0.8	10
Y24	−0.012	0.068	5.7	0.7	2.26	(−0.12/+0.13)	0.9	11
Y71	−0.073	0.049	4.9	1.0	2.41	(−0.19/+0.24)	0.8	8
Y175	−0.014	0.055	5.8	0.8	2.24	(−0.12/+0.14)	0.2	9

[a]Number of analyses.
All uncertainties are 2σ.

Figure 1

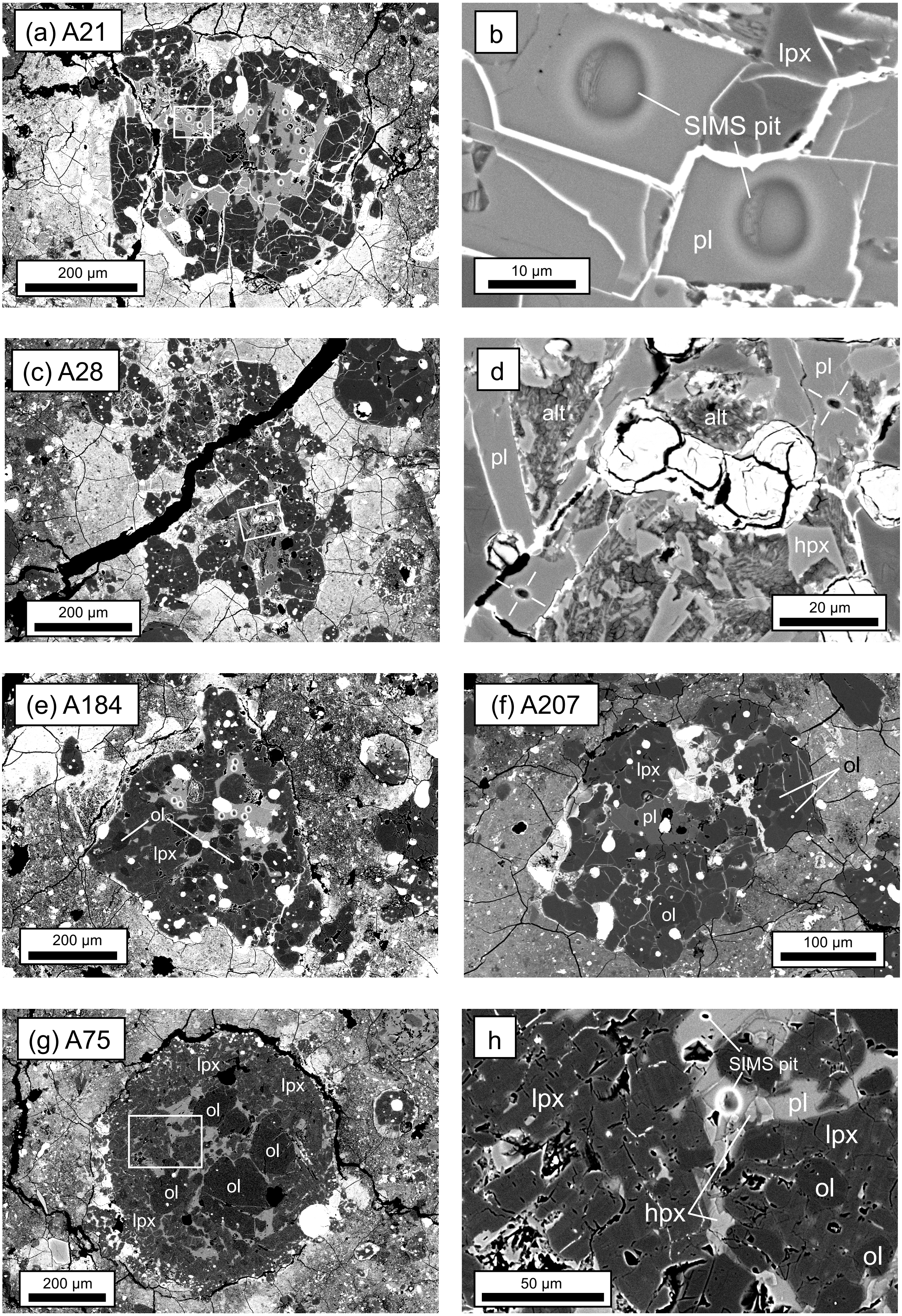
(a) A21
200 µm
b
lpx
SIMS pit
pl
10 µm
(c) A28
200 µm
d
alt
alt
pl
pl
hpx
20 µm
(e) A184
ol
lpx
200 µm
(f) A207
lpx
pl
ol
ol
100 µm
(g) A75
lpx
lpx
ol
ol
ol
ol
lpx
200 µm
h
SIMS pit
lpx
pl
lpx
ol
hpx
ol
50 µm

Figure 2

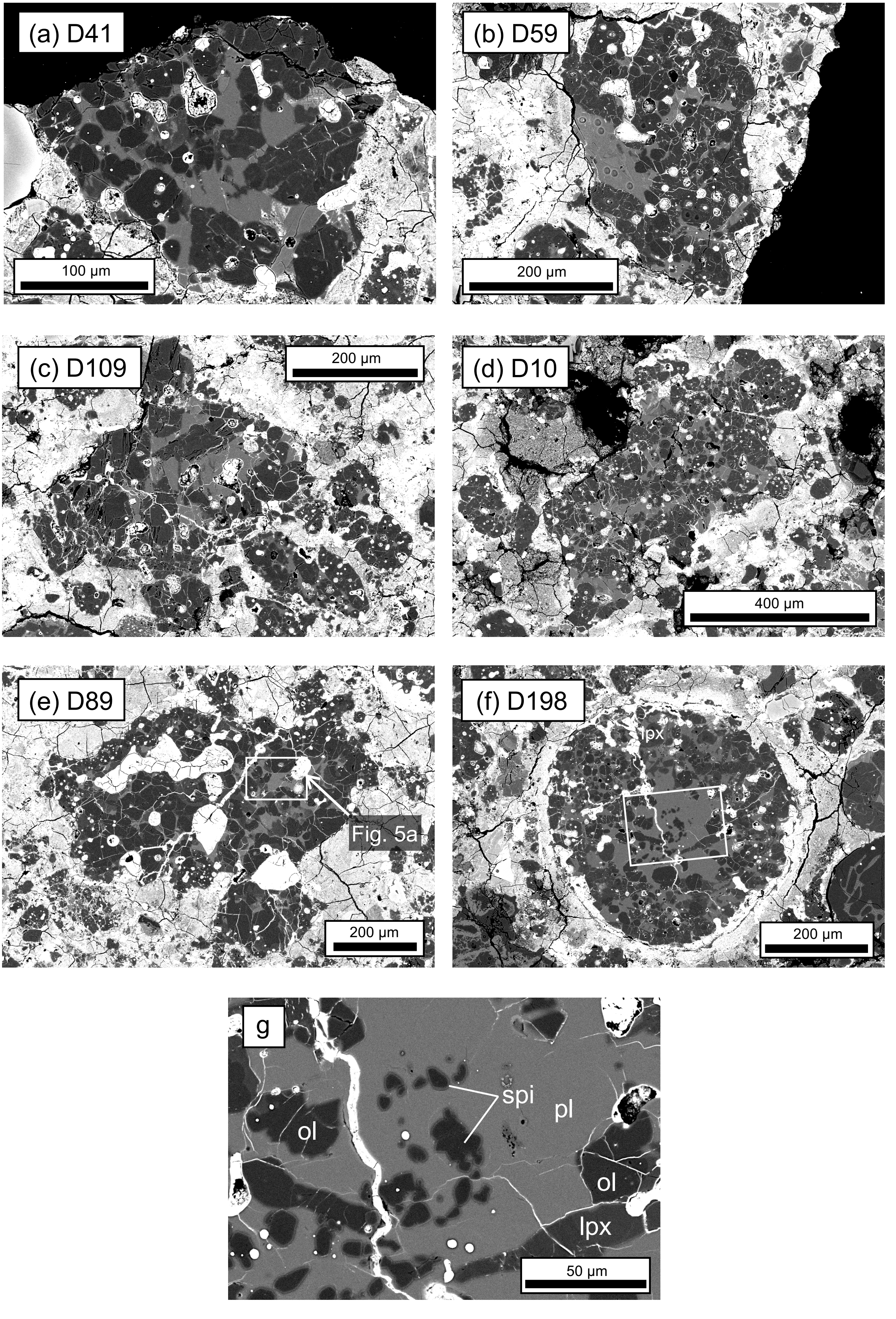

(a) D41
100 µm
(b) D59
200 µm
(c) D109
200 µm
(d) D10
400 µm
(e) D89
Fig. 5a
200 µm
(f) D198
lpx
200 µm
g
spi
pl
ol
ol
lpx
50 µm

Figure 3

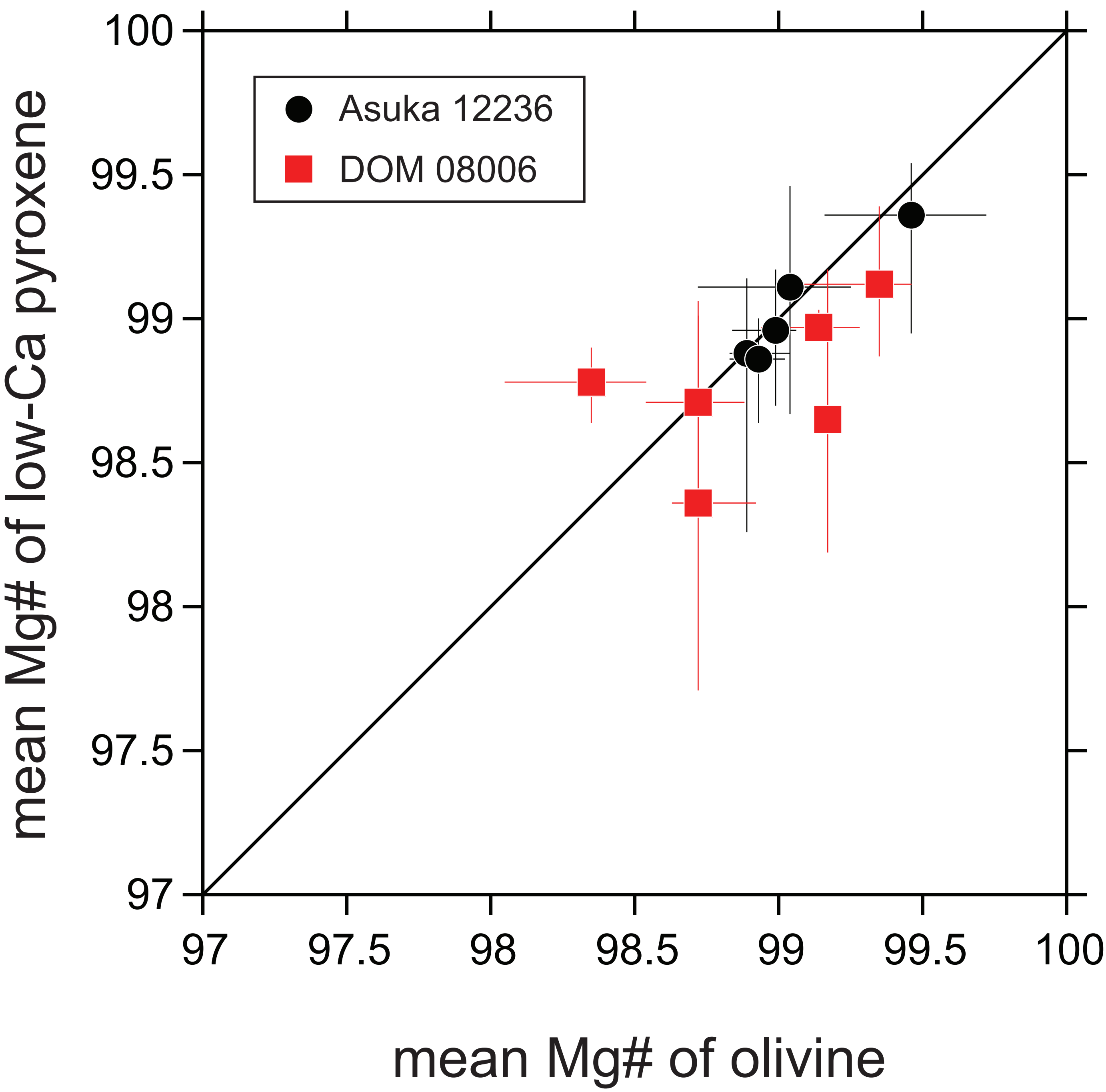

Asuka 12236
DOM 08006
100
99.5
99
98.5
98
97.5
97
mean Mg# of low-Ca pyroxene
mean Mg# of olivine

Figure 4

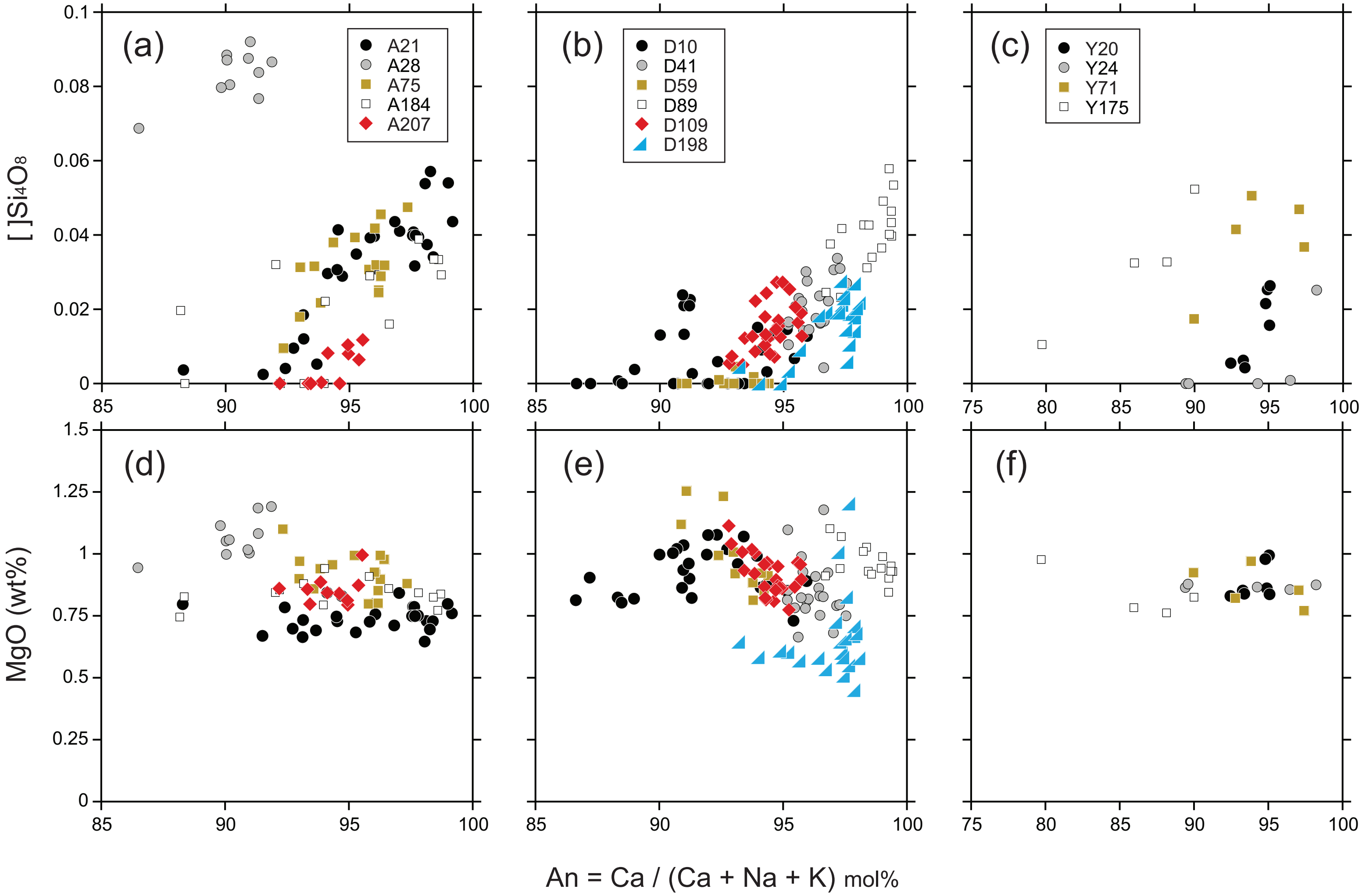

(a)
A21
A28
A75
A184
A207
(b)
D10
D41
D59
D89
D109
D198
(c)
Y20
Y24
Y71
Y175
[ ]Si4O8
0.1
0.08
0.06
0.04
0.02
0
85
90
95
100
75
80
(d)
(e)
(f)
MgO (wt%)
1.5
1.25
1
0.75
0.5
0.25
0
An = Ca / (Ca + Na + K) mol%

Figure 5

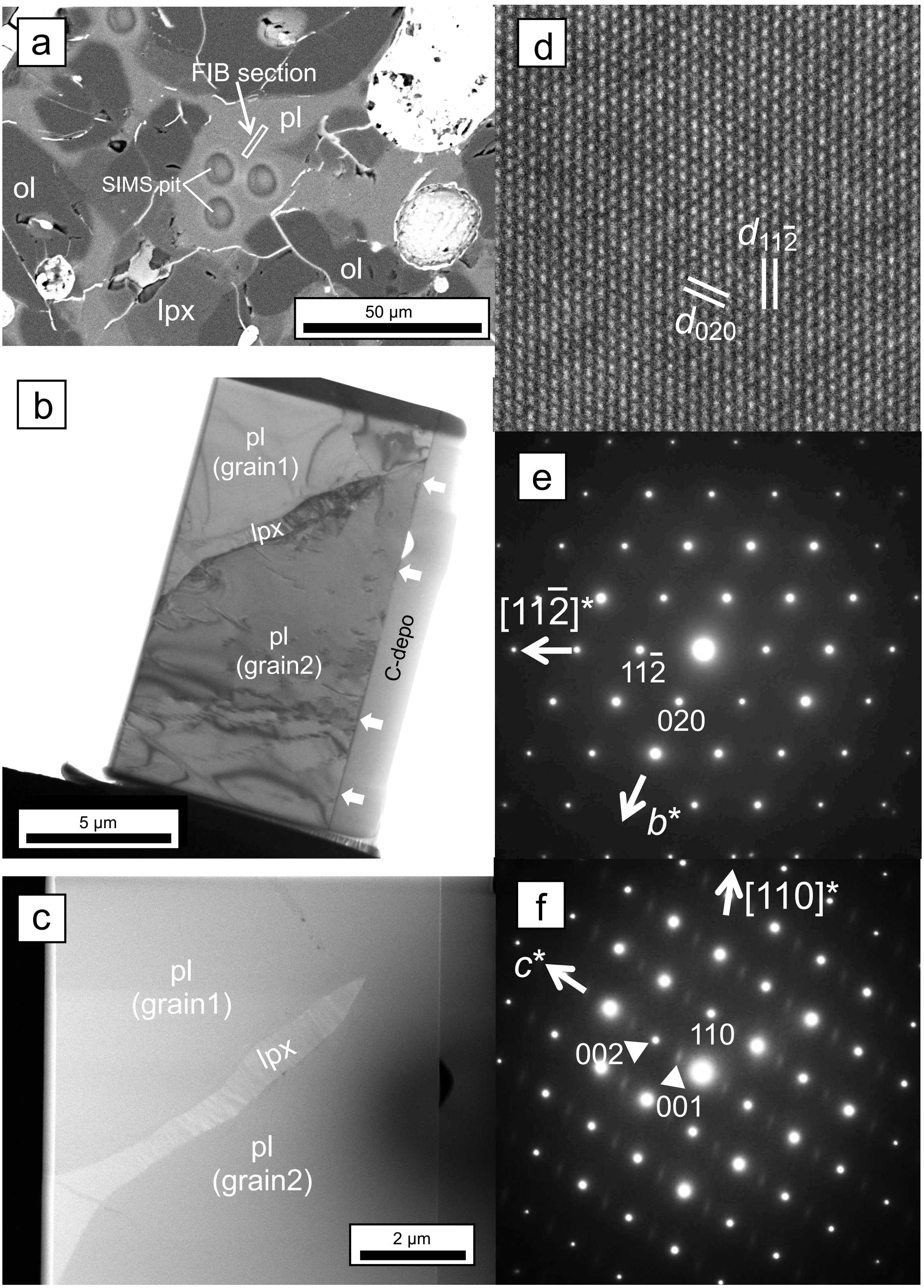

a
FIB section
pl
SIMS pit
ol
ol
lpx
50 μm
b
pl
(grain1)
lpx
pl
(grain2)
C-depo
5 μm
c
pl
(grain1)
lpx
pl
(grain2)
2 μm
d
$d_{11\bar{2}}$
d_{020}
e
$[11\bar{2}]^*$
$11\bar{2}$
020
b^*
f
$[110]^*$
c^*
110
002
001

Figure 6

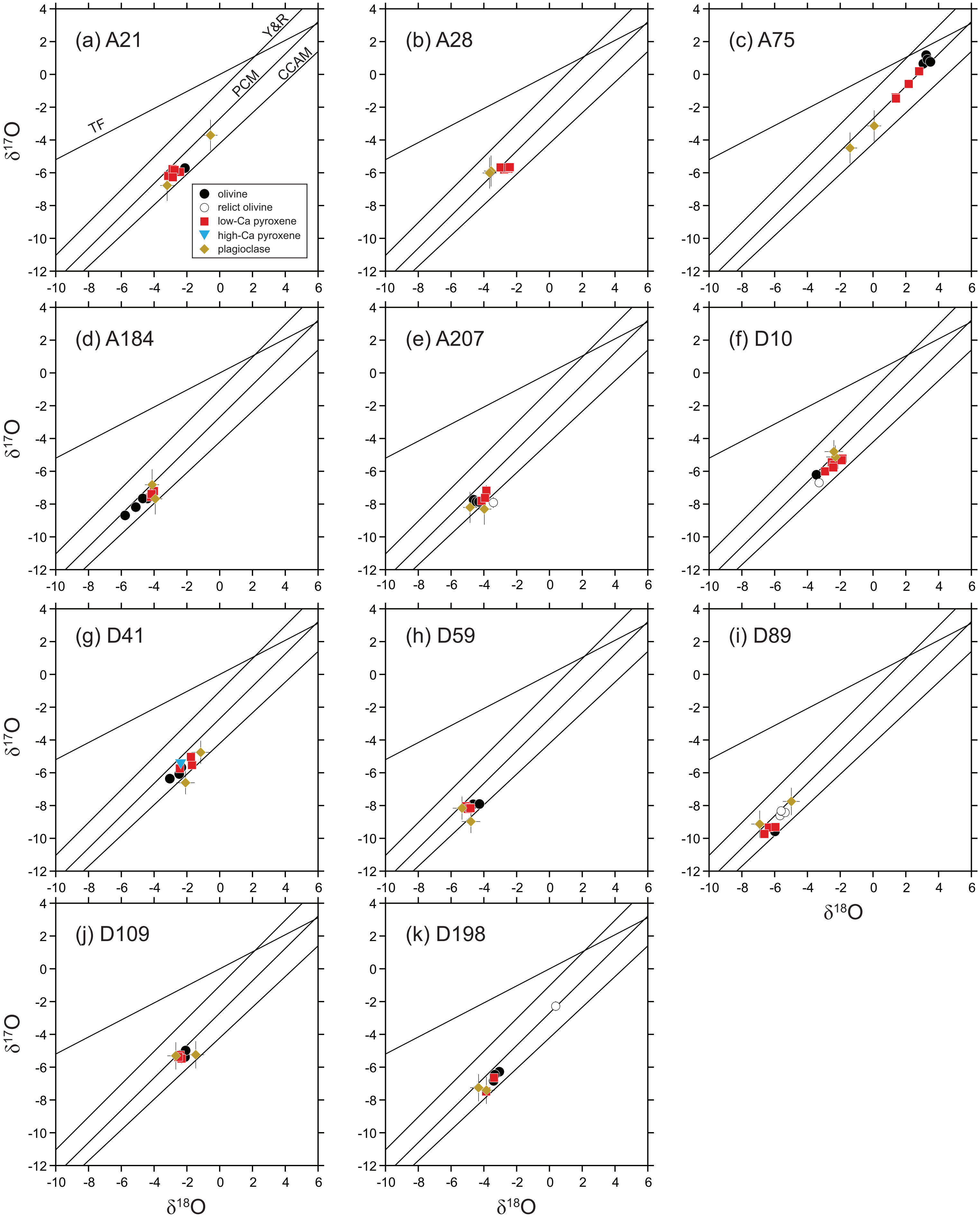

(a) A21
(b) A28
(c) A75
(d) A184
(e) A207
(f) D10
(g) D41
(h) D59
(i) D89
(j) D109
(k) D198
TF
PCM
Y&R
CCAM
olivine
relict olivine
low-Ca pyroxene
high-Ca pyroxene
plagioclase
$\delta^{17}O$
$\delta^{18}O$

Figure 7

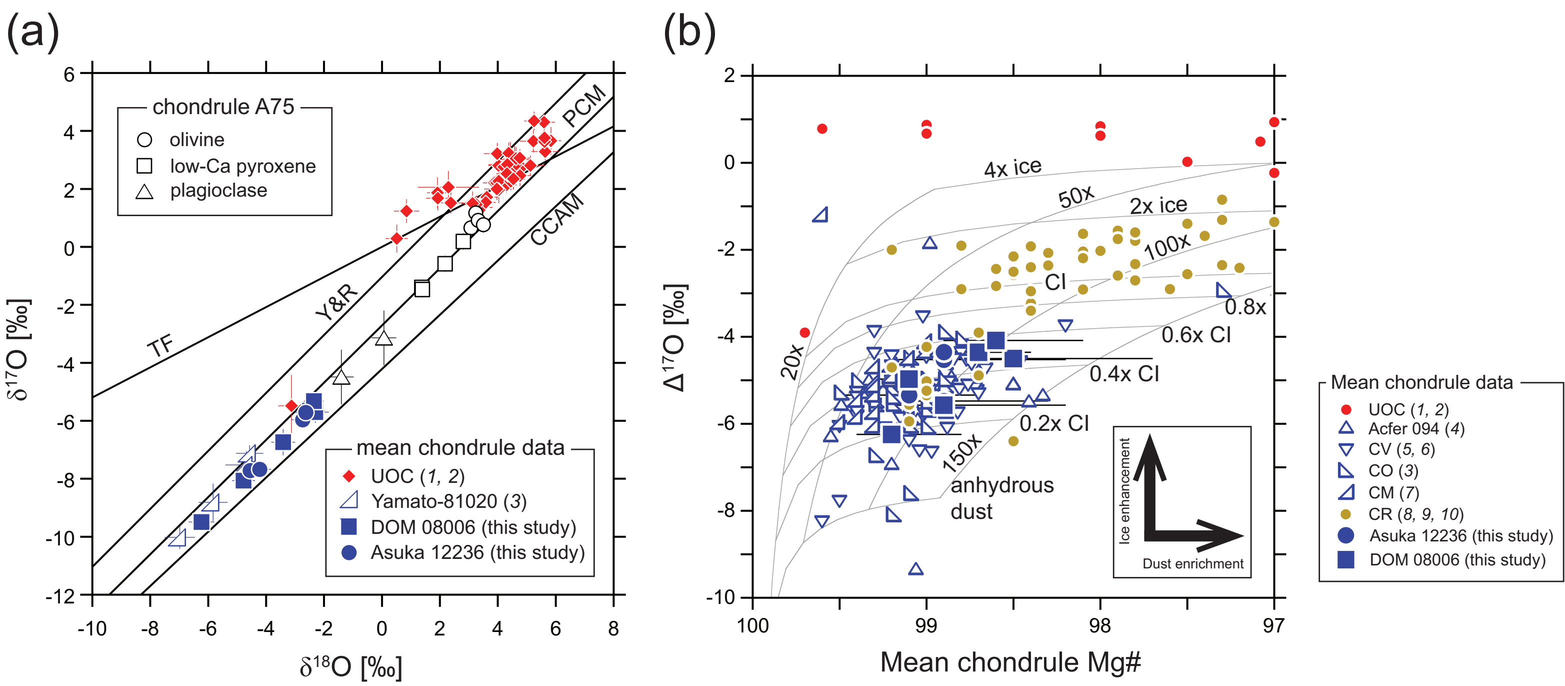

(a)
chondrule A75
olivine
low-Ca pyroxene
plagioclase
PCM
Y&R
CCAM
TF
mean chondrule data
UOC (1, 2)
Yamato-81020 (3)
DOM 08006 (this study)
Asuka 12236 (this study)
δ17O [‰]
δ18O [‰]
(b)
4x ice
50x
2x ice
100x
CI
0.8x
0.6x CI
0.4x CI
0.2x CI
20x
150x
anhydrous dust
Ice enhancement
Dust enrichment
Δ17O [‰]
Mean chondrule Mg#
Mean chondrule data
UOC (1, 2)
Acfer 094 (4)
CV (5, 6)
CO (3)
CM (7)
CR (8, 9, 10)
Asuka 12236 (this study)
DOM 08006 (this study)

Figure 8

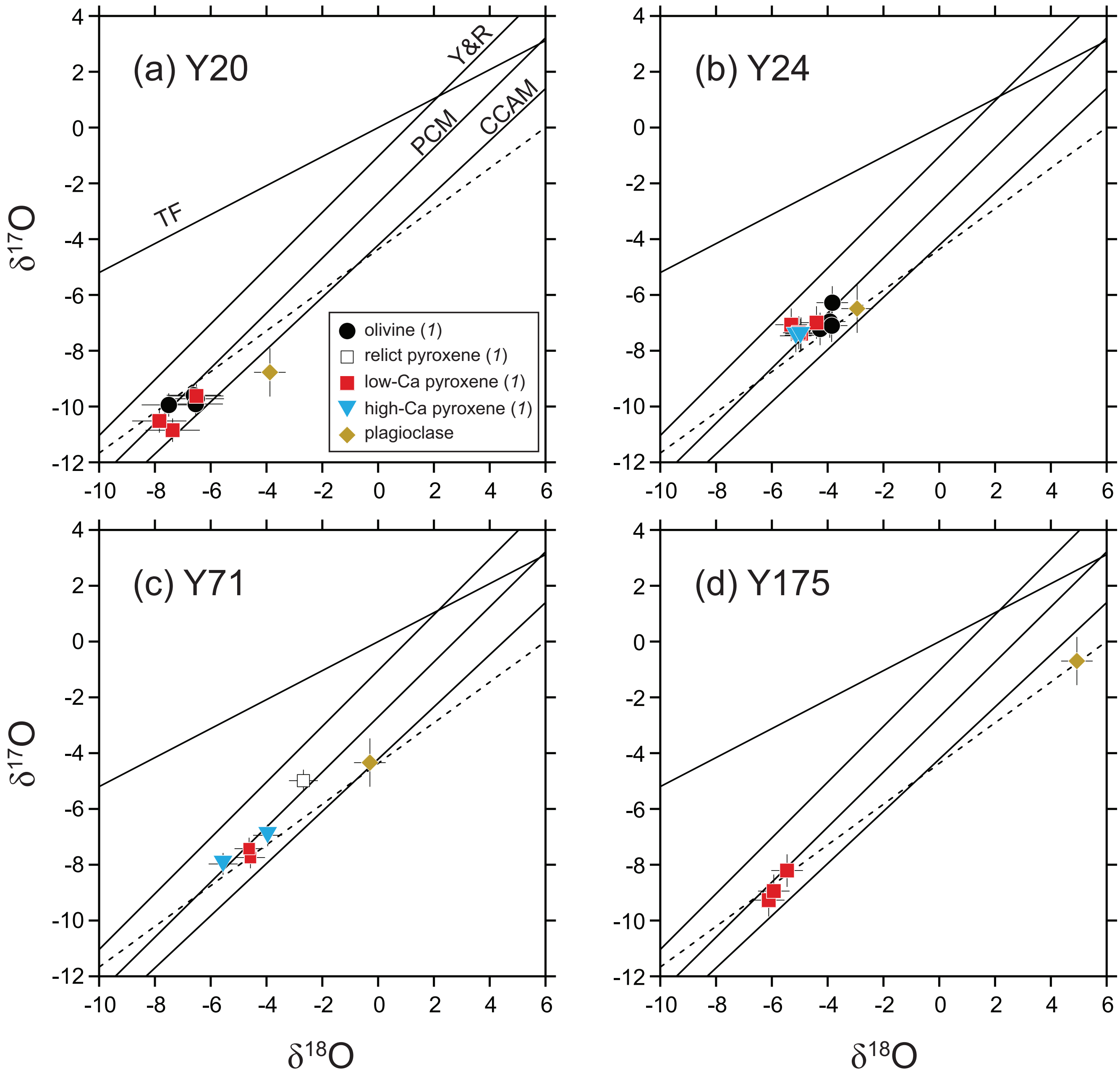
(a) Y20
(b) Y24
(c) Y71
(d) Y175
TF
Y&R
PCM
CCAM
olivine (1)
relict pyroxene (1)
low-Ca pyroxene (1)
high-Ca pyroxene (1)
plagioclase
δ17O
δ18O

Figure 9

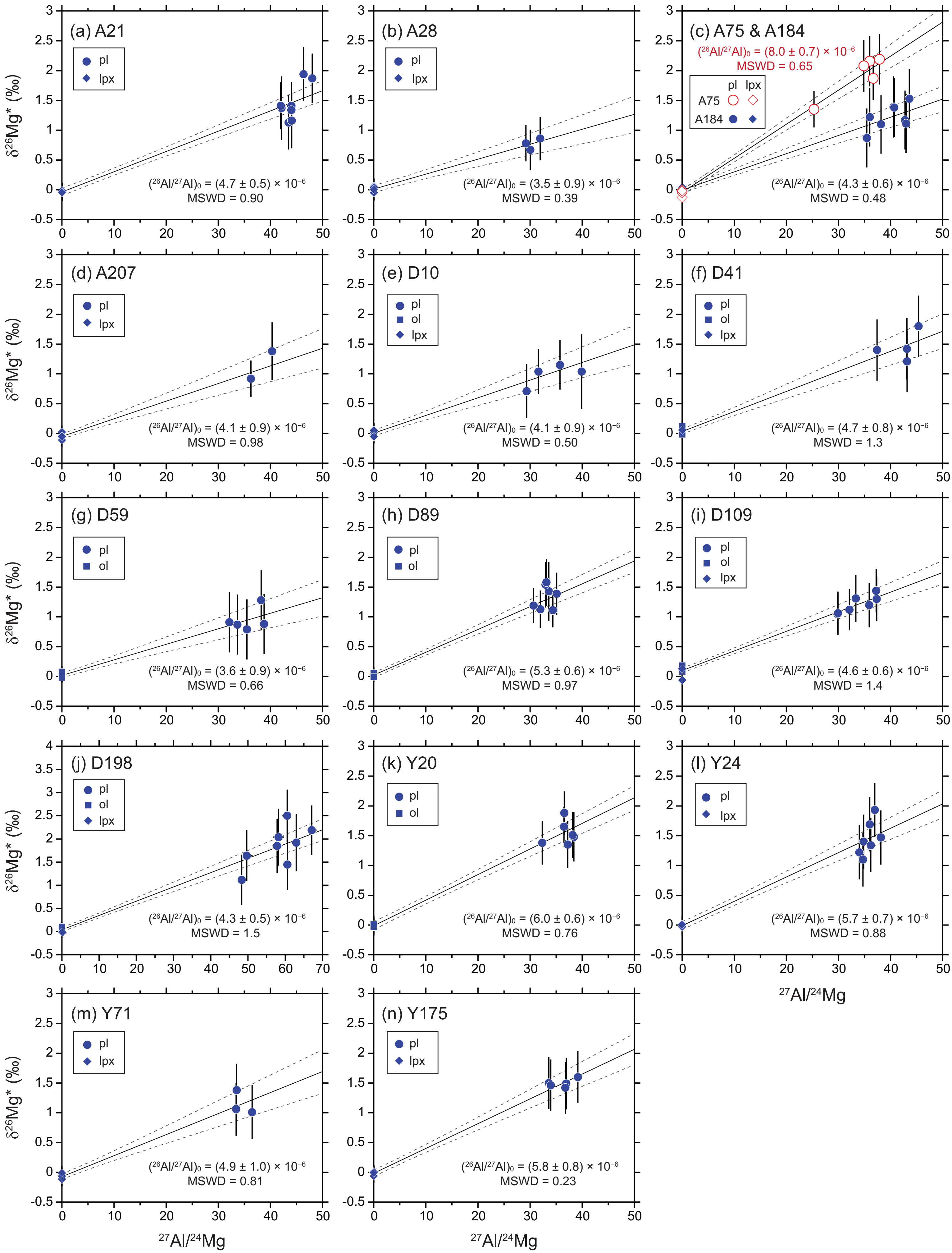
(a) A21
pl
lpx
$(^{26}Al/^{27}Al)_0 = (4.7 \pm 0.5) \times 10^{-6}$
MSWD = 0.90
(b) A28
pl
lpx
$(^{26}Al/^{27}Al)_0 = (3.5 \pm 0.9) \times 10^{-6}$
MSWD = 0.39
(c) A75 & A184
$(^{26}Al/^{27}Al)_0 = (8.0 \pm 0.7) \times 10^{-6}$
MSWD = 0.65
pl lpx
A75
A184
$(^{26}Al/^{27}Al)_0 = (4.3 \pm 0.6) \times 10^{-6}$
MSWD = 0.48
(d) A207
pl
lpx
$(^{26}Al/^{27}Al)_0 = (4.1 \pm 0.9) \times 10^{-6}$
MSWD = 0.98
(e) D10
pl
ol
lpx
$(^{26}Al/^{27}Al)_0 = (4.1 \pm 0.9) \times 10^{-6}$
MSWD = 0.50
(f) D41
pl
ol
lpx
$(^{26}Al/^{27}Al)_0 = (4.7 \pm 0.8) \times 10^{-6}$
MSWD = 1.3
(g) D59
pl
ol
$(^{26}Al/^{27}Al)_0 = (3.6 \pm 0.9) \times 10^{-6}$
MSWD = 0.66
(h) D89
pl
ol
$(^{26}Al/^{27}Al)_0 = (5.3 \pm 0.6) \times 10^{-6}$
MSWD = 0.97
(i) D109
pl
ol
lpx
$(^{26}Al/^{27}Al)_0 = (4.6 \pm 0.6) \times 10^{-6}$
MSWD = 1.4
(j) D198
pl
ol
lpx
$(^{26}Al/^{27}Al)_0 = (4.3 \pm 0.5) \times 10^{-6}$
MSWD = 1.5
(k) Y20
pl
ol
$(^{26}Al/^{27}Al)_0 = (6.0 \pm 0.6) \times 10^{-6}$
MSWD = 0.76
(l) Y24
pl
lpx
$(^{26}Al/^{27}Al)_0 = (5.7 \pm 0.7) \times 10^{-6}$
MSWD = 0.88
(m) Y71
pl
lpx
$(^{26}Al/^{27}Al)_0 = (4.9 \pm 1.0) \times 10^{-6}$
MSWD = 0.81
(n) Y175
pl
lpx
$(^{26}Al/^{27}Al)_0 = (5.8 \pm 0.8) \times 10^{-6}$
MSWD = 0.23
$\delta^{26}Mg^*$ (‰)
$^{27}Al/^{24}Mg$

Figure 10

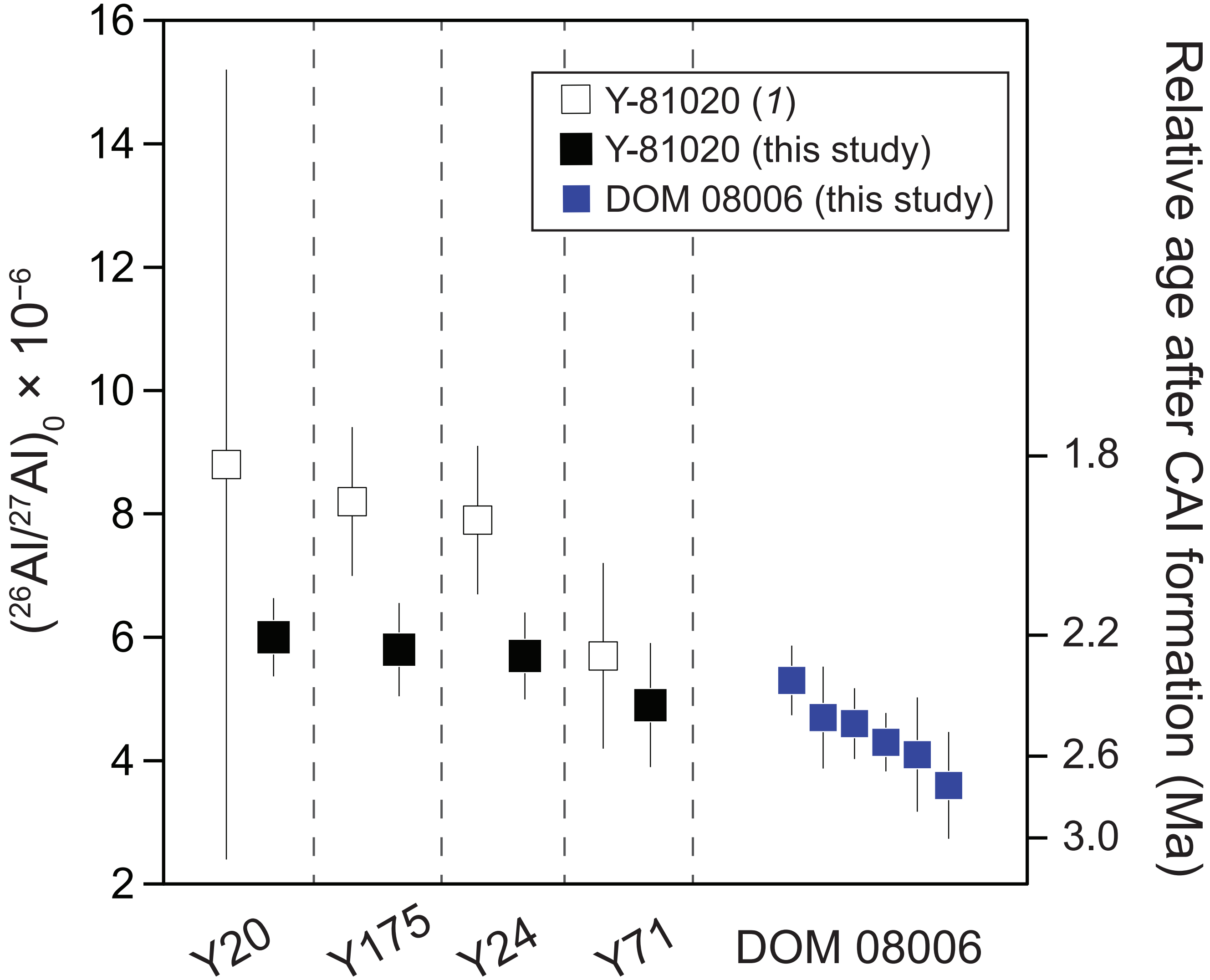

16
14
12
10
8
6
4
2
($^{26}Al/^{27}Al$)$_0$ × 10^{-6}
Y-81020 (*1*)
Y-81020 (this study)
DOM 08006 (this study)
1.8
2.2
2.6
3.0
Relative age after CAI formation (Ma)
Y20
Y175
Y24
Y71
DOM 08006

Figure 11

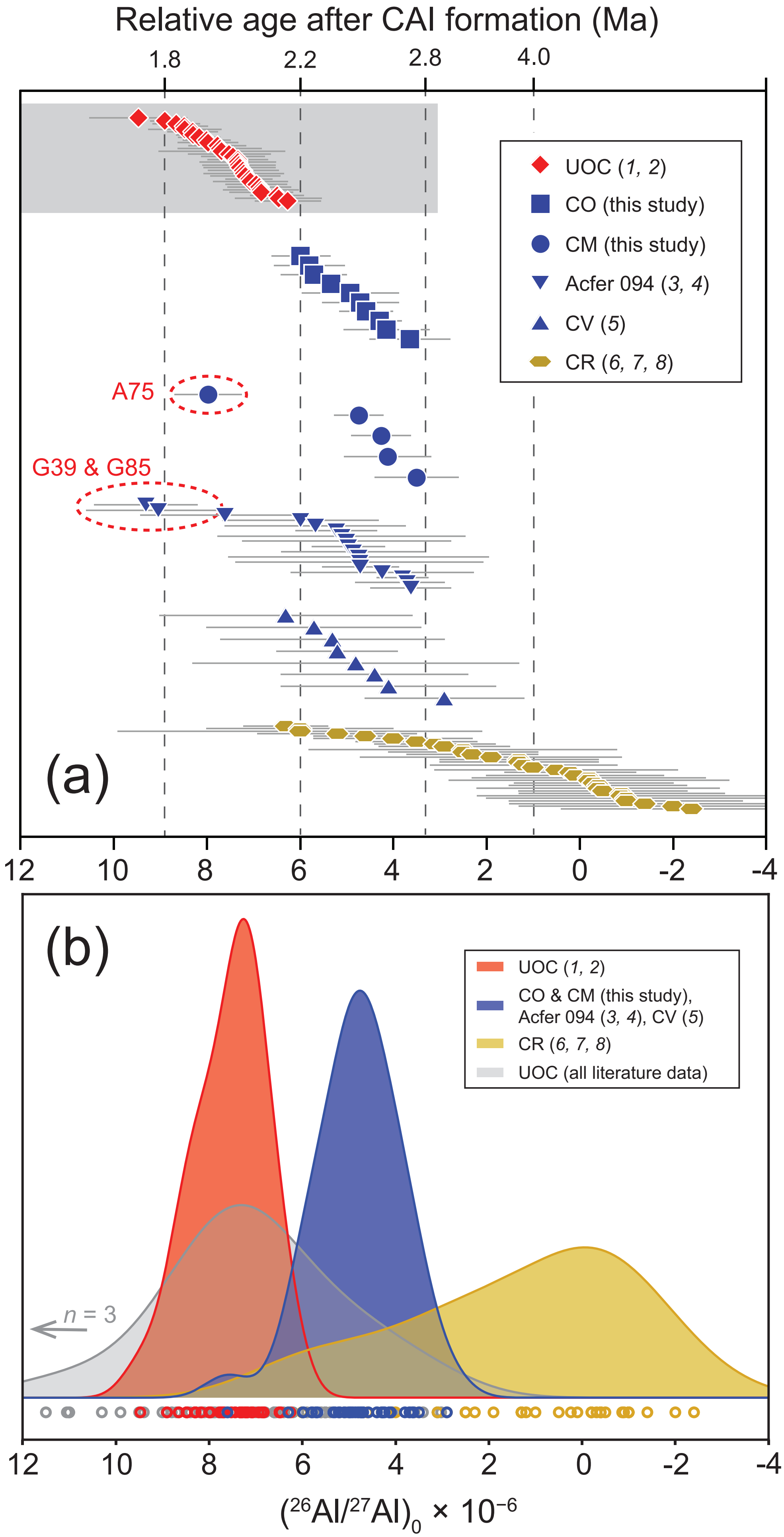

Relative age after CAI formation (Ma)
1.8
2.2
2.8
4.0
UOC (1, 2)
CO (this study)
CM (this study)
Acfer 094 (3, 4)
CV (5)
CR (6, 7, 8)
A75
G39 & G85
(a)
12
10
8
6
4
2
0
-2
-4
(b)
UOC (1, 2)
CO & CM (this study), Acfer 094 (3, 4), CV (5)
CR (6, 7, 8)
UOC (all literature data)
n = 3
12
10
8
6
4
2
0
-2
-4
(^{26}Al/^{27}Al)$_0$ × 10^{-6}

Figure12

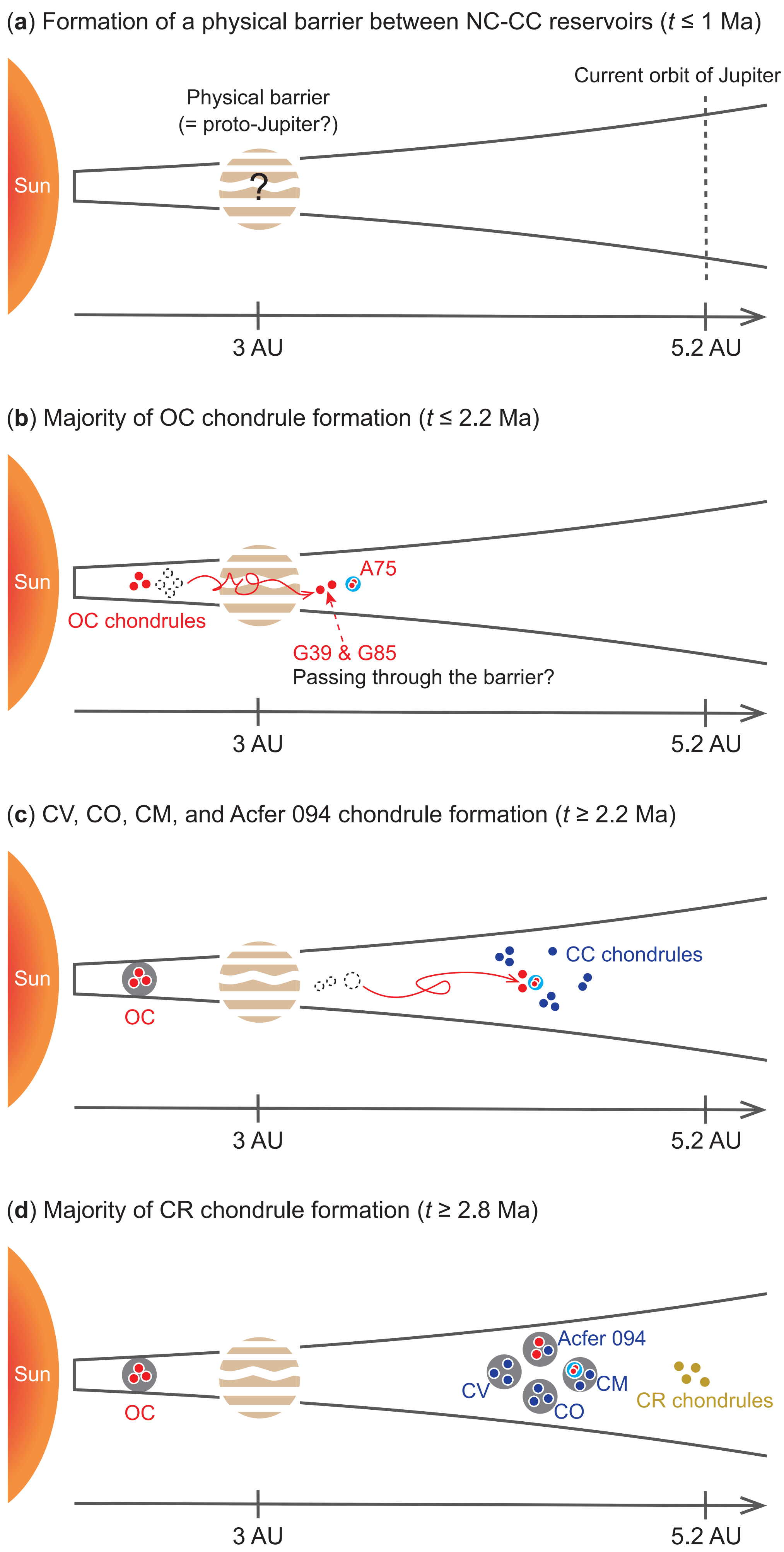

(a) Formation of a physical barrier between NC-CC reservoirs (t ≤ 1 Ma)
Current orbit of Jupiter
Physical barrier
(= proto-Jupiter?)
Sun
?
3 AU
5.2 AU
(b) Majority of OC chondrule formation (t ≤ 2.2 Ma)
Sun
A75
OC chondrules
G39 & G85
Passing through the barrier?
3 AU
5.2 AU
(c) CV, CO, CM, and Acfer 094 chondrule formation (t ≥ 2.2 Ma)
Sun
CC chondrules
OC
3 AU
5.2 AU
(d) Majority of CR chondrule formation (t ≥ 2.8 Ma)
Sun
Acfer 094
CV
CM
CO
CR chondrules
OC
3 AU
5.2 AU